Republic of Tunisia
Ministry of Higher Education,
Scientific Research

University of Sfax
National Engineering School of Sfax
(ENIS)

Doctoral School

Sciences and Technologies

Electrical Engineering

Order n°: 25 –2023

THESIS

Presented in

The National School of Engineers of Sfax

In order to obtain the

DOCTORATE

In
Electrical Engineering

By

Thaar Abdalraheem Kareem Al-musaadi

Contribution to the design of CSS-UWB receiver for medical applications in the WBAN network

Defended on 01/07/2023, in the presence of the examining committee:

Mr.	**Nabil DERBEL**	**(Professor at ENIS)**	**President**
Mr.	**Mohamed BEN SLIMA**	**(Professor at ENET'COM)**	**Reporter**
Mr.	**Hafedh TRABELSI**	**(Professor at ENIS)**	**Reporter**
Mr.	**Hamdi GASSARA**	**(Professor at ENIS)**	**Examiner**
Mr.	**Hatem TRABELSI**	**(Professor at ENIS)**	**Supervisor**

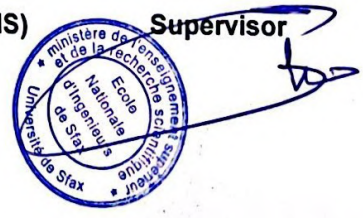

Dedications

To the one who encouraged me to persevere and be patient throughout my life, to the most important man in my life

(Dear father)

To my beloved mother... I can't find words that can give her due, as she is the epic of love and the joy of life, and an example of dedication and giving.

To my lovely wife.... the highest symbols of sincerity, honesty, and companion on the path. A big thanks to you because without you, I would not have been able to overcome all of my difficulties.

To my gift from God… the most valuable thing I have... the sweetest feeling... and the most beautiful joy, my son (Hasan) and my daughter (Asal).

To my brothers and sister.... thanks for supporting me and sharing my joys and sorrows in this life.

Thaar Abdalraheem Kareem

Acknowledgment

I would like to start by thanking Allah Almighty for giving me strength and patience, and every time I get weak I find God my only refuge and the source of my strength... Thanks my God, for hearing all my prayers.

I would like to express my gratitude to my supportive supervisor, **Mr. Hatem TRABELSI**, Professor at ENI-Sfax, University of Sfax, for his enthusiasm for the work and for his support, encouragement, and patience. He continuously encouraged me and was always willing to assist in any way throughout my Ph.D. study.

I am very appreciative of the honor **Mr. Nabil DERBEL**, Professor at ENI-Sfax, University of Sfax, has bestowed upon me by agreeing to preside over the jury for my thesis defense. I would like to thank him for his interest in this work.

My thanks are also addressed to **Mr. Mohamed BEN SLIMA**, Professor at ENET'Com, University of Sfax, and **Mr. Hafedh Trabelsi**, Professor at ENI-Sfax, University of Sfax, for giving me the honor to report this thesis.

My special thanks are addressed to **Mr. Hamdi GASSARA**, Professor at ENI-Sfax, University of Sfax, for agreeing to examine this work.

بسم الله الرحمن الرحيم

"قَدْ جَعَلَها رَبِّي حَقًّا"

صدق الله العظيم

Table of Contents

List of Figures

List of Table

List of Abbreviations

ADS Advance Design System

A/D Analog to Digital converter

BW Bandwidth

CMOS Complementary Metal Oxide Semiconductor

DRC Design Rule Check

DS-OFDM Direct Sequence Orthogonal Frequency-Division Multiplexing

EIRP Equivalent Isotropic Radiated Power

FCC Federal Communications Commission

FHSS Frequency Hopping Spread Spectrum

HRV Heart Rate Variability

IC Integrated Circuit

ILO Inter level Oxide

IR-UWB Impulse radio ultra-wide band

LNA Low Noise Amplifier

MOSFET Metal Oxide Semiconductor Field Effect Transistor

nMOS n-channel MOS

pMOS p-channel

OOK On-Off Keying

PAM Pulse-Amplitude Modulation

PPM Pulse-Position Modulation

CSS Chirp Spread Spectrum

RF Radio Frequency

SNR Signal to Noise Ratio

TSMC Taiwan Semiconductor Manufacturing Company Ltd.

UWB Ultra-wideband

WBAN Wireless Body Area Network

BS Base station

LFM linear Frequency Modulation

General Introduction

Due to the growing need of current Internet of Things (IoT) infrastructures, in terms of connectivity and network capacity, connected people have an aspiring potential to form an imminent access network that extends the IoT coverage, through achieving ubiquitous and real-time applications (healthcare, social interactions, sports and entertainment, etc.), thus ensuring anywhere and anytime people connectivity.

Nowadays, the field of wireless sensor networks is gaining great progress in the applications and technologies used due to its contribution to creating a flexibly connected world. The wireless aspect allows sensor networks to adapt to a variety of applications by deploying a large number of sensors, including instrumentation, military monitoring and medical monitoring.

These sensors are of great interest for the remote monitoring of the elderly, people with reduced mobility or at risk and their living environment. [1].

A very great importance to this practice emerged from the appearance of implantable devices in the 1960s with the first pacemaker designed and manufactured by Rune to extend to cochlear implants, auditory, for the vision coming to programmable drug delivery pumps and neuro-stimulators [2] [3].

We have a population that tends towards aging, confirmed by the United Nations Department of Economics and Social Affairs (population division): around the year 2050, the number of elderly people will double, reaching 2.1 billion [4]. This will not correspond to the number of professional staff in the health field or to the allocated budget. Thus, a collection of clinical data from a patient distant from the hospital or from his doctor will make it possible to act on time.

With rapidly aging populations in many countries, the need to monitor human vital signs has increased dramatically in recent years. The Wireless Body Area Network (WBAN) technology imposed itself due to the continued increase in the global population of chronically ill elderly people [5] [6].

The rise of new technologies and advances in microelectronics and telecommunications have led to the development of new wireless applications that tend to use low-power implantable and wearable chips capable of monitoring patients' vital signs. To be practical, the device must be small in size, wireless and capable of operating on battery power for years. Two types

of wireless medical electronic devices are used: the first includes non-implanted devices and the second includes implanted devices.

Considerable attention has been given to CMOS as an emerging technology used in low power, low complexity and low cost microelectronic systems. This technology is the best solution for realizing the transceiver part of the sensor node thanks to its large scale of integration for frequencies exceeding Gigahertz. These wireless sensors have now enabled the development of high-performance dynamic systems for monitoring physiological parameters, capable of taking into account significant technological constraints: high integration for reduced bulk and low consumption for greater autonomy.

More and more Application Specific Integrated Circuit (ASIC) chips are now being designed specifically for biomedical applications.

The design of the receiver part of the wireless sensor node with low power consumption and reduced complexity is a very dynamic research topic. In order to optimize energy efficiency, the choice of receiver architecture, RF band and receiver RF technical parameters are critical.

Ultra-Wide Band (UWB) communication authorizes the use of the free band between 3.1 and 10.6 GHz, without license. UWB technology is ideal for WBAN applications as there are potential advantages such as low probability of interception, eases coexistence with existing wireless communication systems, higher data rates, lower power dissipation and enhanced security of medical data due to a power spectral density emission limit of -41.3 dBm/MHz as transmitter output power dedicated by the Federal Communications Committee (FCC).

Applying Impulse Radio-Ultra-Wide Band (IR-UWB) technology in medical applications is an emerging research trend in recent years. According to the Shannon-Hartley theorem, the maximum channel capacity is inversely proportional to the channel's bandwidth and the logarithm of the signal-to-noise ratio. This indicates that the UWB communication system's wide bandwidth enables it to attain faster data rates than narrow band systems, but the extremely low transmission levels also permit coexistence between UWB and current standards.

The objective of this work is the design of a Chirp Spread Spectrum (CSS) RF receiver of the "wireless sensor node" using the 3-5GHz UWB band for medical applications in the WBAN network. This work focuses on analysis and optimizations of the RF-front end blocks such as Low Noise Amplifier (LNA) and Mixer at the transistor level and system level in CMOS TSMC 0.18µm technology. The goal is to reduce power consumption, circuit complexity and enhance linearity performance of the CSS-UWB receiver.

The chapters are divided as follows:

The first chapter is a brief introduction to the field of Wireless Body Area Network with its various applications in the medical field as well as how to send, receive and process signals. Then we give an overview about the Ultra-Wideband (UWB) communication and some of its properties.

In the second chapter, we introduce the state-of-the-art UWB transceiver architectures. The various RF transceiver designs as well as the standards key features which an RF transmitter's performance is measured will be explained. To emphasize the selection criteria for RF designs, the benefits and drawbacks of each architecture will be evaluated. We'll also present the RF circuits technical parameters including conversion gain, noise figure (NF), second order intermodulation products, third-order intercept and 1dB compression point which are used by RF circuit designers to gauge the effectiveness of their designs. At the end of this chapter, the first important part of the UWB receiver which is a balun LNA circuit will be proposed. The LNA was analyzed and simulated using TSMC 0.18µm design kit on ADS tool.

The third chapter presents a study and optimization of the UWB receiver based on a differential double balanced passive mixer. The mixer uses NMOS transistors as switches and designed to work with 25% duty cycle local oscillator signal. Performances simulation results are presented and compared with other works.

The fourth chapter consists of two parts. The first part presents system level simulation of the complete CSS receiver including the LNA, the mixer, the low pass filter and the AGC amplifier. Harmonic balance simulations as well as budget simulation are used to determine cascaded gain, NF, P-1dB at each node of the receiver chain. Time representation and spectrum at each node are also given.

The second part includes analysis of MOSFET transistors mismatches effect on the performance of UWB receiver front-end. A Monte Carlo and harmonic balance simulations were performed using 0.18µm CMOS process to evaluate the impact of $^{W}/_{L}$ mismatch as well as V_{th} mismatch on the receiver gain and IIP2.

Finally, a general conclusion will close this report which will give a brief summary of the results and highlight research work perspectives.

Chapter 1

WBAN Communication and UWB technology

1. Introduction

Recent advances in microelectronics, microsystems, and low-power radio frequency technology have made it possible to produce miniature communication devices called wireless sensors. These are inexpensive, low-powered, and self-contained. They thus respond to changes in physical environmental phenomena. These sensors make it possible to capture, convert physical quantities into digital quantities, and transmit them wirelessly using various capture, processing, data storage, and wireless transmission units.

Therefore, wireless sensors represent embedded systems. Several of them are used to autonomously collect environmental data and transmit it to one or more collection points, forming a network of wireless sensors. Wireless sensor networks have represented an important research topic in recent years and have now generated an increasing demand for sensor networks for various applications.

These networks are of particular interest for home automation, military applications, and those related to the monitoring of critical infrastructure and medical monitoring. However, due to their characteristics (energy limitation, reduced node capacity, a large number of sensors, etc.), the power reduction of these sensors is today the source of many scientific and technological challenges.

In this chapter, we will first focus on wireless sensor networks. We will also present the WBAN standard as well as its different applications. Finally, we will mention the history of UWB technology and its regulations throughout the world.

2. Networks of Wireless Sensors

wireless sensor networks (WSNs) are networks of sensor nodes that are geographically dispersed across the environment, and each provides a specific function both alone and in conjunction with other nodes[7]. These networks' primary objective is to gather environmental data and transmit it to the base station (BS) or distant server. The use of WSN

in healthcare is one such application. This application uses wearable sensors that are attached to the body to track and monitor bodily motions as well as detect physiological variables like heart rate and body temperature [3]. These sensors capture data and transmit it to the BS for processing, analysis, and storage. The information is then securely sent over the Internet or another medium to distant medical servers. Because the data contain private information derived from physiological variables, security is essential. All personal information has to be secured against unwanted access. The health of a patient may be remotely monitored thanks to wireless body area networks (WBANs), a specific form of sensor network that uses wireless sensor nodes on the body to record physiological parameters including blood pressure, body temperature, heart rate, and blood sugar level. WBANs come in wearable and implantable varieties. WBANs' primary goal is to assure people's health by transferring physiological data from body sensors to medical servers so that doctors may better comprehend the health of their patients. Recent advances in microelectronics, microsystems, and low-power radio frequency technology have made it possible to produce miniature communication devices called wireless sensors. These are inexpensive, low power, and self-contained. They thus respond to changes in physical environmental phenomena. These sensors make it possible to capture, and convert physical quantities into digital quantities and transmit them wirelessly using various capture, processing, data storage, and wireless transmission units. Therefore, wireless sensors represent embedded systems. Several of them are used to autonomously collect environmental data and transmit it to one or more collection points, forming a network of wireless sensors. Wireless sensor networks have represented an important research topic in recent years and have now generated an increasing demand for sensor networks for various applications. These networks are of particular interest for home automation, military applications, and those related to the monitoring of critical infrastructure and medical monitoring. However, due to their characteristics (energy limitation, reduced node capacity, a large number of sensors, etc.), the power reduction of these sensors is today the source of many scientific and technological challenges In this chapter, we will first focus on wireless sensor networks. We will also present the WBAN standard as well as its different applications and related work. Finally, we will mention the history of UWB technology and its regulations throughout the world.

2.1. Utilizing Sensors to Control Health

Sensor networks are becoming increasingly important in healthcare, as they enable real-time health diagnostics that can make up for missed degenerative illnesses, save lives, and save medical expenses. In certain cutting-edge hospitals, rudimentary sensor types are already being utilized to manage drug regimens, monitor doctors and patients in the hospital, and monitor patient physiology data. Nursing the elderly is one of the uses for sensor networks in this area, as they can spot falls, unconsciousness, vital signs, food, and activity. An ultra wide band device will be built to gather and provide information about the body's insulin levels, blood pressure, bone density, and heart health, and may diagnose a patient with an arrhythmia and foretell the start of a heart attack. This device must be cheap and available to everyone, and capable of storing and sending large volumes of data.

2.2. IoT Healthcare

The Internet of Things (IoT) refers to a network of interconnected physical devices that are able to collect data about their surroundings and operate in response to that information. Smart objects' sensors output data that may be analyzed further to inform choices. These "smart" objects are preloaded with software that manages their individual components and the events they cause. By bringing together the best features of previously separate areas of communication technology, the IoT paradigm opens up novel avenues for innovation in many different sectors, including cloud computing, WBANs, edge computing, fog computing, and automated computing. In the year 2025, it is predicted that there will be 75 billion IoT-connected devices in use. Business, manufacturing, healthcare, retail, and defense/security are just few of the sectors impacted by the Internet of Things. Smart parking, smart lighting, trash management, forest fire warning, earthquake detection, intelligent crop management, and remote care for the elderly are just a few examples of the various ways the IoT may be put to use.

3. Body Sensor Network Architecture

3.1. Sensor Network Architecture

As can be seen in Figure 1.1, there are three distinct phases in the development of body sensors.

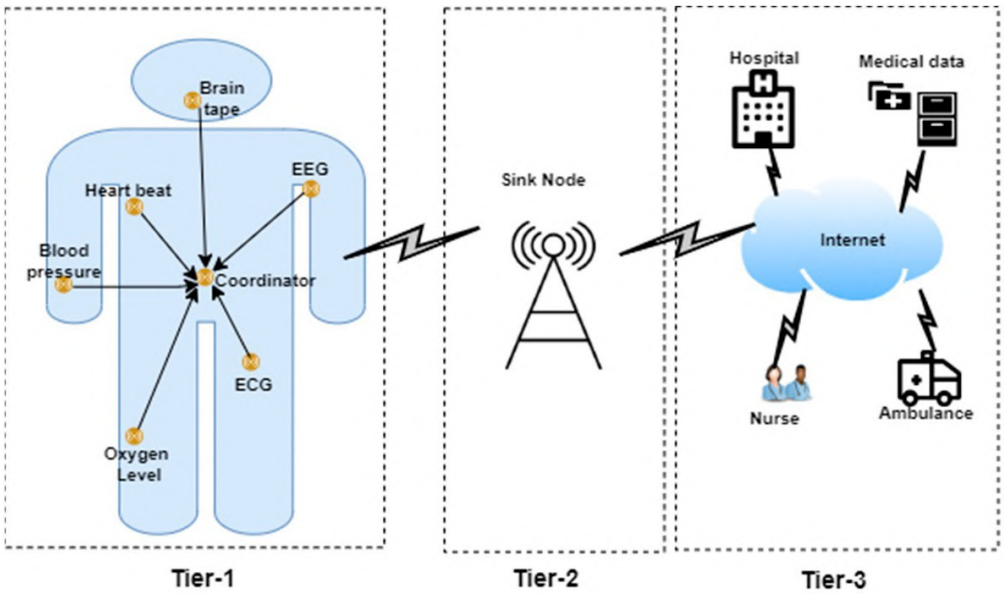

Figure 1.1. *The architecture of wireless body sensor networks.*

First: Medical sensor nodes are implanted in the human body or wearable along with the sinkhole located[8].

Second, the data is relayed from the sinkhole to the BS after being aggregated and processed.

Third, the BS relays the data to the hospital over the Internet network so that doctors may check in on patients from afar. Each sensor in this network [8] collects sensory information from the patient's body and transmits it to the sink node, which in turn forwards the information to the BS, which may subsequently dispatch medical assistance.

3.2. How to Run the Body Sensor Network

Today, enhancing the level of intelligence and synchronization of industrial or environmental systems requires the usage of wireless sensor networks. Wireless body sensor networks are one of the main applications of wireless sensor networks in human healthcare systems. After a patient leaves the hospital and resumes their regular routine, this sensor network transmits physiological signals from patients or the elderly to healthcare facilities. This makes it possible for doctors and emergency rooms to properly and promptly respond to patients' medical requirements while also monitoring their status in real time or with a short delay. An illustration of a wireless sensor network in a healthcare system is shown in Figure 1.2. This network gathers physiological data from patients in various settings and transmits it to a unit that coordinates medical care. The doctor receives this information via a variety of communication channels.

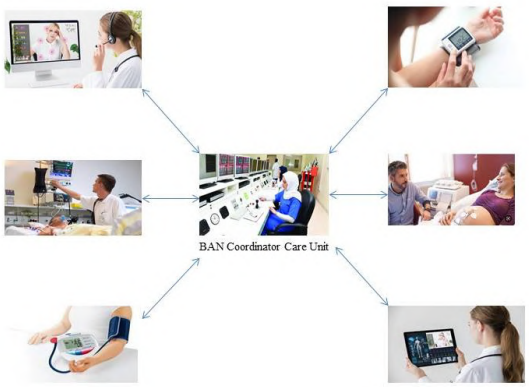

Figure 1.2. *Example of a body sensor network.*

The BAN coordinator unit then receives the data given by the sensors. Its main function is to time the data transfer and aid in the extraction of useful information from the dataset obtained from the patient's body. The storage unit is another component of this node. In this unit, delayed data are preserved and made available to the medical facility upon request. Sometimes it's necessary to store the data because of bad channel conditions or high data traffic.

The communication unit and the power supply unit are two additional crucial components of this network. To coordinate the nodes and communicate with following nodes, a transceiver with four radiofrequency channels between 850 GHz and 2.4 MHz is often employed. Batteries designed for tiny and portable parts offer the necessary power. Figure 1.4 depicts the design of the University of Virginia researchers' TEMPO body sensor node, which is shown as being the size of a coin [9].

These body sensor nodes are all linked together by a central node using a star topology. All nodes on the body deliver data to a collector unit in this design. In the hybrid mesh star approach, communication is established between the coordinating units of each group, and the other nodes are alerted right away in the event of a problem in one node. In order to connect to larger networks, this design also links collector units and bridges. The star topology is shown in Figure 1.4 while the mesh star composite topology is shown in Figure 1.5[10].

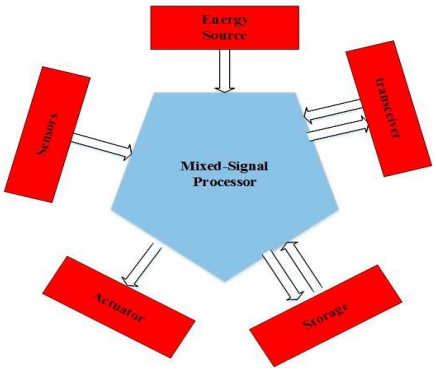

Figure 1.3. *A body sensor node structure includes sensors, a mixed signal processor, storage, a transceiver unit, an energy source, and an actuator unit.*

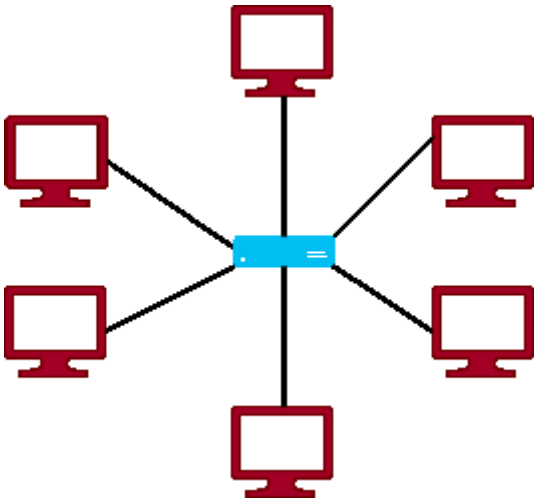

Figure 1.4. *Star topology structure.*

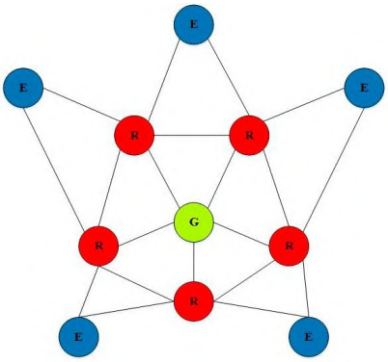

Figure 1.5. *The structure of a mesh star composite topology in which nodes are connected to a central node.*

Their hierarchical nature is another feature of these networks. Large volumes of data are continually received by this network, and microprocessors must extract the relevant information and attributes. Hierarchical data collecting is also used. It follows that the network contains several sensors at the next node of the dataset, and each sensor node processes data locally. In the composition of data, the collecting unit is in charge. As a middleman between lower levels of the network and the nodes, these collectors integrate the data from the nodes. The information gained at each higher level can serve as feedback to the lower levels, helping to enhance feature extraction, categorization, and sensor coordination. The data flow in the body's wireless sensor network and and some examples of sensors for telemedicine are depicted in Figure 1.6 [11].

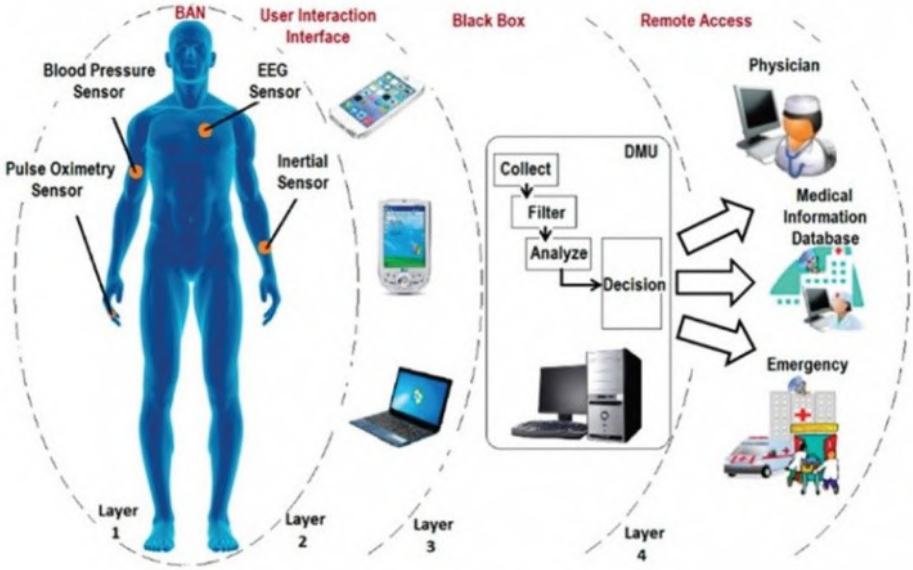

Figure 1.6. *Examples of sensors for telemedicine in the wireless body sensor network of the body.*

Wireless body sensor networks also face problems with the technological coordination of many components. One tool that helps the WBANs harmonize and cooperate is standardization. The examples of innovative wireless technologies shown in the next section are intended for application in wireless body sensor networks.

4. WBAN communication

According to statistics from the World Health Organization (WHO), the elderly are the fastest-growing age group in the world[12]. By 2050, there will be 2 billion people over 60 or almost a quarter of the population. Immigration is one of the ever-changing social forces

affecting the care and well-being of older people[12]. As they age, they are more susceptible to mobility issues and chronic illnesses. Overall, the incidence of chronic diseases is increasing in people of all ages. Active health management, as well as early diagnosis and detection before it is too late, can help to control this[13]. Therefore, it is expected to increase the chances of using medical equipment without affecting people's normal lives. The demand for medical systems using advances in wireless communication technology is evidenced by the design of low-power, intelligent, and miniaturized medical devices that can be used on or around the human body or even implanted in the human body[14]. This special type of Wireless Sensor Network (WSN) is called the Wireless Body Area Network (WBAN).

A crucial technology Wireless Body Area Network (WBAN) has evolved as a means of better diagnosing a number of dangerous disorders. This device monitors the patients' physiological indicators and health conditions in real time[6]. Since WBAN is a rapidly evolving technology, a number of challenges still need to be resolved. In WBAN, either a sensor network on a band or numerous light-weight sensors that monitor different physiological signs are worn by the patient Figure. 1.7. They can send biosignals (vital signs) to the relevant system at a healthcare facility. The monitoring healthcare professional retrieves and processes the patient data. According to [15], WBAN emerged as a groundbreaking approach in recent years and is widely accepted.

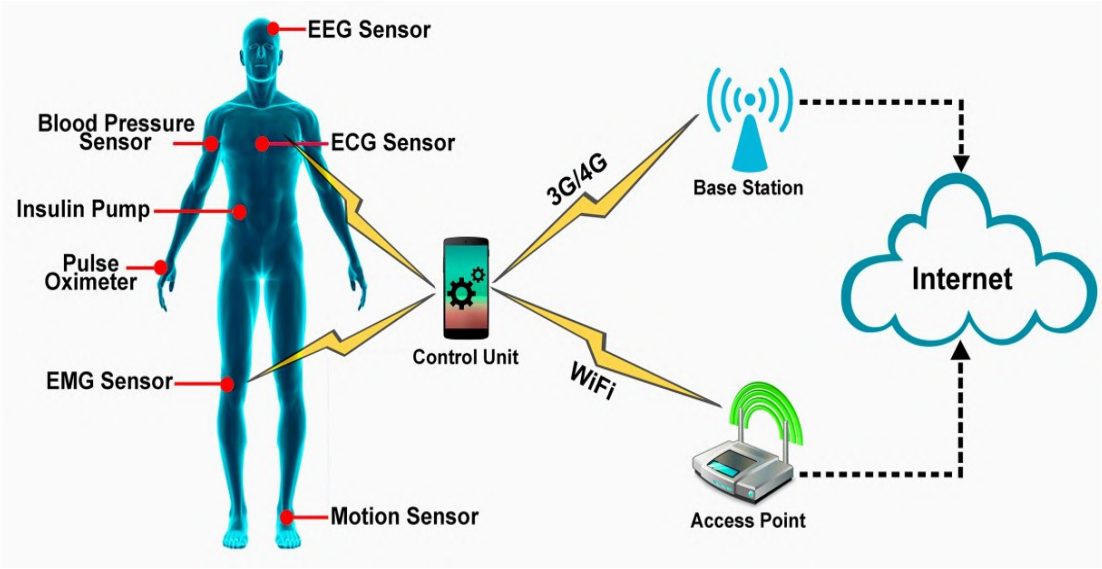

Figure 1.7. *The path of the data in the wireless body sensor network of the body.*

4.1. WBAN Architecture

The development of wireless communication standards and technology has accelerated during the past ten years. E-Health and Telemedicine, two fields at the forefront of this development, make full use of the wireless communication technologies currently available to deliver emergency and on-demand medical services, enable outpatient monitoring and treatment, support patient recovery, and establish direct connections between doctors, nursing staff, and patients. WBAN is one example of how this is done. WBAN is a wireless networking technology that links a few tiny nodes with sensor or actuator capabilities. It is based on radio frequency (RF). These nodes serve a variety of medical and non-medical sector applications by operating within a few centimeters of, on, or just outside of a human body. WBAN collects physiological information from sensor nodes using medical bands. In order to maximize the cohabitation of sensor node devices with other network devices accessible at medical centers, the medical band is chosen in a way that minimizes interference. The medical gateway wireless boards are then used to send the acquired data to distant stations using a multi-hoping approach[16]. The use of WBAN technology in healthcare and medical research is well regarded[17][18]. Additionally, the discipline of biomedicine and other scientific fields have benefited greatly [19]. Additionally, it has several uses in non-medical fields, including personal entertainment and consumer electronics[20]. In earlier work, [21] outlines a low-cost WBAN that successfully took data and displayed it on a website while utilizing off-the-shelf hardware and was tested in real time. The BAN gathered the patients' whereabouts, temperatures, and pulse rates. A graphing application programming interface was used to make the collected data accessible, allowing for continuous data monitoring on a website. The BAN is currently powered by a 9V battery.

The architecture of a WBAN typically consists of four main components: sensors, a communication module, a processing unit, and a network infrastructure.

In Figure 1.8. a diagram that illustrates the basic architecture of a WBAN:

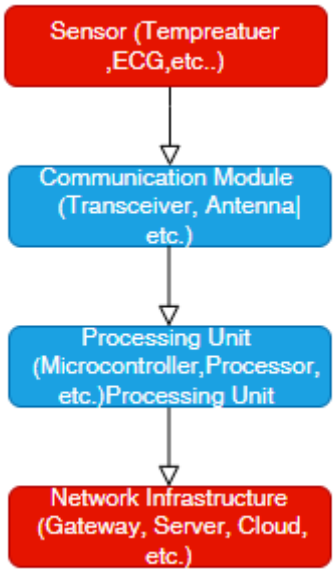

Figure 1.8. *Basic architecture*

- The sensors are attached to the body and are used to measure various physiological parameters such as temperature, heart rate, blood pressure, and movement. These sensors can be either wearable devices or implanted devices.
- The communication module is responsible for transmitting the data collected by the sensors wirelessly to the processing unit. The communication module can consists of a transceiver, an antenna, and other components that enable wireless communication.
- The processing unit is responsible for processing the data received from the sensors and making decisions based on that data. The processing unit typically consists of a microcontroller, a processor, and other components that enable data processing.
- The network infrastructure is responsible for connecting the WBAN to the internet and other networks. This can include a gateway that connects the WBAN to a local network, a server that stores and processes data, and a cloud service that enables remote access to the data.

Overall, the architecture of a WBAN is designed to enable the collection, processing, and transmission of data from wearable and implanted devices in a secure and efficient manner. This architecture has the potential to revolutionize healthcare by enabling continuous monitoring of patient health and enabling remote diagnosis and treatment.

4.2. Intra-WBAN communication

In this part, we focus on the main design requirements of wireless communication technologies that can be applied in WBAN, as follows:

• Data Rate: The data rate should support multiple WBAN applications and should be between 10 kbps and 10 Mbps. BER determines the reliability of data transmission and depends on the importance of the data. The reliability of WBAN depends on both packet transmission delay as well as the possibility of packet loss. The BER must be less than 10-3.

• Communication range: WBAN allows sensors related to the human body to communicate with each other, so an effective communication range of 2 to 5 m in WBAN is sufficient.

• Transmission power: the WBAN sensor can transmit up to 1 mW (0 dBm) of power, which corresponds to the specific absorption rate (SAR) of 1.6 W / Kg in 1 g of human tissue[22]. The battery life of WBAN nodes is expected to be extended by several months or even years, especially for nodes implanted subcutaneously.

• Deadline: The main purpose of the monitoring application is to collect information in real time, so strict deadlines are crucial. According to the IEEE 802.15.6 standard, the delay of medical applications must be less than 125 milliseconds and non-medical applications must be less than 250 milliseconds.

• Mobility: Due to body posture movement, WBAN may experience signal attenuation, which may affect reliability and QoS indicators (such as packet transmission speed, delay, etc.). This reliability is essential to protect the lives of patients. Therefore, energy-efficient data transmission with high reliability and low latency is required to ensure successful data transmission.

• Coexistence: WBANs can interact and coexist with each other, or with other wireless technologies (such as Bluetooth, ZigBee, WLAN, etc.). The coexistence algorithm must ensure that the WBAN works well in a dynamic heterogeneous environment where technologies collaborate to exchange information. Taking into account the different operating environments and the characteristics of each WBAN application, these requirements may vary. In an effort to meet WBAN requirements, communication between sensor nodes and coordination and communication between sensor nodes involve many wireless technologies.

• Configuration: the WBAN must be configurable, allowing a single node to join the WBAN system without any external intervention.

4.3. WBAN applications

WBAN can be used for a variety of purposes, including medicinal as well as non-medical ones. An overview of WBAN submissions Table 1.1 displays the necessary parameters as well as other information[23][24]. As shown in Figure 1.9, WBAN may be further divided into three categories.

Table 1.1 Wireless technologies in medical monitoring[23].

Application Type (Sensitivity to Latency)	Sensor Node Privacy	Data rate	Duty Cycle (per device)	Power Consumption	QoS (Sensitivity to Latency)	Privacy
In-body Applications	Glucose Sensor Pacemaker Endoscope Capsule	Few Kbps Few Kbps >2 Mbps	<1% <1% <50%	Extremely Low Low low	Yes Yes Yes	High High medium
On-body medical Applications	ECG SPO2 Blood pressure	3 Kbps 32 bps <10 bps	<50% <10% <1%	Low Low high	Yes Yes Yes	High High High
On-body non-Medical Applications	Music for Headset Forgotten Things Monitor Social Networking	1.4 Mbps 256 Kbps <200 Kbps	High Medium <1%	Relatively Low Low	Yes Yes No Low	Low Low High
Off-body Applications	Motion Sensor	35 Kbps	-	-	-	Low

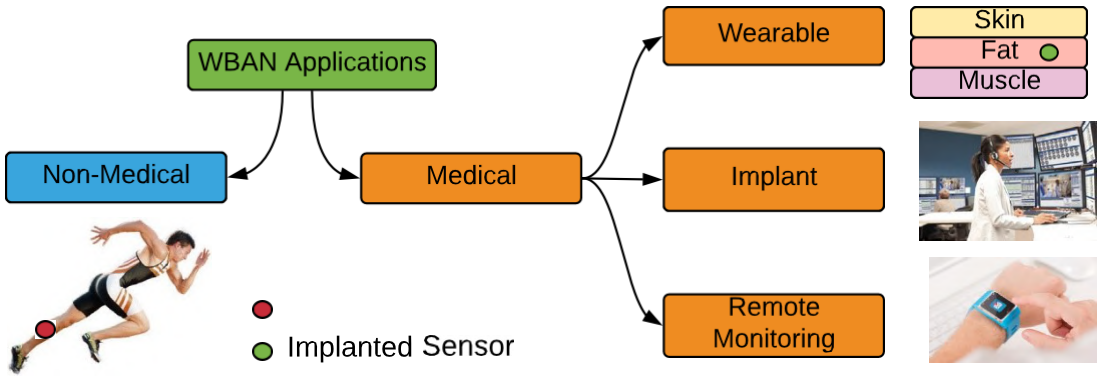

Figure 1.9. *Classification of WBAN*

4.3.1. Medical applications

In terms of medical applications, the categories of wearable, implantable, and remote monitoring devices are depending on how the devices are used in the applications. In this subsection, we provide a brief explanation of each area of medical applications.

4.3.1.1. Wearable WBAN

These WBAN devices are often strapped to body surfaces. Below is a discussion of a few wearable WBAN application examples:

WBAN applications can be used on the battlefield to track military activity. It is feasible to monitor from a central station and maintain secure communication using GPS-enabled devices or cameras. A secure communication system is necessary to prevent ambushes[25].

WBAN may be used to monitor the performance level in individual sports. A personal trainer can monitor an athlete's performance level using data from wearable devices that are linked to the athlete's body. Additionally, this application's real-time feedback would encourage performance enhancement and occasionally even prevent accidents [26].

The act of sleeping is crucial to our everyday lives. Productivity at work ultimately suffers from sleep disorders. It not only affects the job, but it also contributes to a number of illnesses, including cardiovascular problems, vertigo when driving, and even appetite loss. As a result, it has become increasingly important to monitor a patient's sleeping patterns. Several biopotentials that were captured overnight in a sleep lab and analyzed using a polysomnography test are used to diagnose sleeping disorders. This type of test necessitates the use of several wires, which makes the patient uncomfortable and even worsens sleep difficulties. WBANs are able to delocalize and do away with the need for cables[27].

Millions of individuals struggle with asthma. The WBAN may be used to track allergic substances in the air and give doctors immediate feedback. In [28], a GPS-based gadget is suggested that analyzes ambient parameters and sounds an alert if it notices an environment to which the patient is allergic. WBAN application includes a service for real-time health monitoring. The WBAN framework, for instance, may be used to monitor a patient rehabilitation facility (depicted in [25]). Patients may be observed for a long period, and physiological data can be sent in real time to the cloud, as shown in Figure. 1.10. However, a group of medical professionals may keep an eye on patients' activities via video conferencing or real-time database updates.

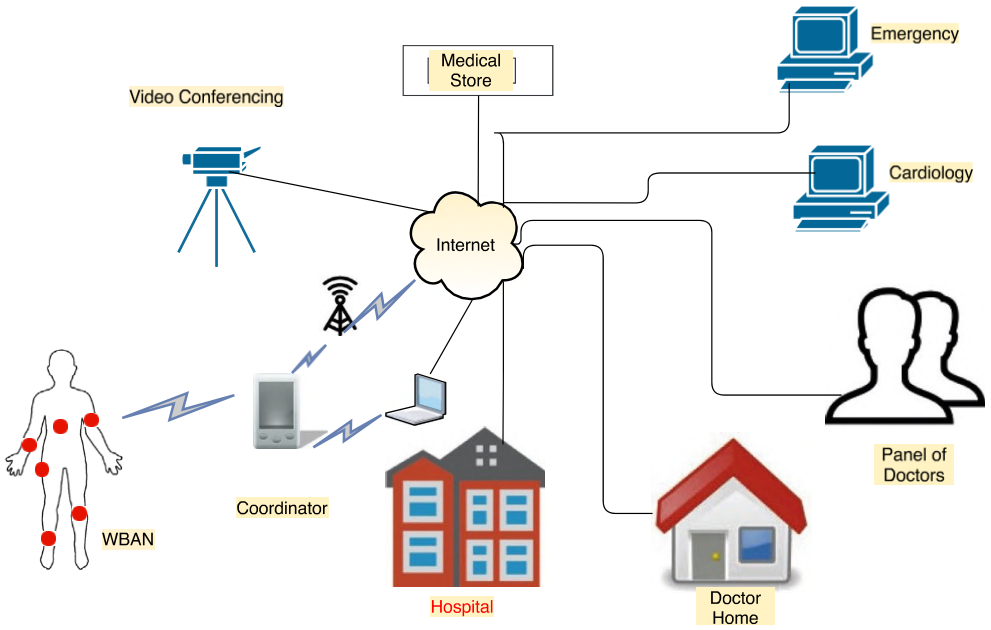

Figure 1.10. *Real-time telemedicine monitoring system for patient rehabilitation.*

4.3.1.2. WBAN implants:

They are typically placed within the body. The following is a discussion of a few implant WBAN application examples:

The World Health Organization estimates that since 1980, there have been an additional 422 million cases of diabetes. Around 1.7 million individuals in Australia have diabetes, and more than 100,000 Australians have received a diagnosis (Diabetes Australia,). This condition may cause a variety of consequences, including heart attack, stroke, blindness, renal failure, and lower limb amputation. Regular WBAN monitoring would lessen diabetes' severity and keep it under control. Diabetes sufferers employ Gluecocellphone technology to monitor their blood glucose levels and send the results to their doctors for additional examination [26].

Among the leading causes of mortality are cardiovascular illnesses. Through the use of WBAN technology, it may be watched. Periodic monitoring of Myocardial Infraction (MI) makes it more likely to be at reduced risk. WBAN technology may be used to track numerous physical health issues [13]. By 2020, the estimated worldwide cancer rate might rise by 50% to 15 million [29]. Doctors may continue to diagnose tumors without a biopsy by keeping track of cancer cells using WBAN-based sensors, which will enable the best possible analysis and therapy[13]. More information about WBAN's implant communication technology may be found in [3].

Remote monitoring - WBAN's seamless Internet link enables it to monitor a patient's body's vital signs and offer real-time feedback on the healing process. WBAN sensors can specifically sense vital physiological variables including blood pressure, body temperature, pulse, respiration, and heart rate. These sensors give information to the doctors about the patients' health status periodically or continually. As a result, doctors find it simple to follow up with patients and offer remote support via phone or video conferencing.

4.3.2. Non-medical applications of WBAN

WBAN is utilized in several non-medical applications in addition to medicinal ones. Below are a few instances of non-medical applications of WBAN.

4.3.2.1. Monitoring of performance, wellbeing, and physical fitness:

In recent years, a variety of gadgets have been utilized for these purposes. A record of physical activities and performances is kept by these gadgets. For instance, the Tomtom smartwatch can monitor the number of calories burned after a specific amount of running. Similar to this, a trainer at a gym can maintain track of a trainee's fitness level and proceed with the subsequent level of activities. In order to assess the sensory data, it is feasible to employ WBAN sensors that may be mounted to the individuals. WBAN sensors may also be installed in corporate buildings to track employee performance and keep them happy, engaged, and productive. For instance, the Hitachi Business Microscope, which is worn around the neck like a nametag, observes the face-to-face communications of office workers via WBAN. This gadget can transmit information on a worker's breathing, speaking volume, ambient light, and air temperature. The manager makes use of this data to enhance the working environment, which boosts pleasure and productivity [30]

4.3.2.2. Apps for entertainment:

WBAN may be utilized in social networking and gaming applications. Both virtual reality and gaming may make use of it. Examples include hand motions or body movements, tracking personal items, and exchanging business cards[13].

Emergency: Smoke detectors can set off a fire alarm in the event that a home fire spreads. Elderly persons who are deaf, however, are unable to feel the fire. With the help of a WBAN sensor, it is possible to gauge how bad the situation is and remain secure. WBAN sensors (off the body) can play a crucial role to protect the workplace and even lives in sectors that are susceptible to fire or hazardous gas.

4.3.2.3. Authentication:

The WBAN application may be used for safe authentication. This makes use of biometric features including odor, face identification, iris recognition, palm print, hand geometry, and odor detection. Unique biometric signatures are provided by biometric signals like ECG, EEG, and electrodermal activity (EDA), which are difficult to steal, copy, falsify, or lose. Commonly referred to as "Cognitive Biometrics," this system. The Department of Homeland Security of the United States of America uses technologies like Future Attribute Screening Technology (FAST). According to[30], the FAST system employs biosignals obtained from off-body sensors, such as heart and respiration rates, skin temperature on the face, voice tone, pupil dilation, and body movement. Tables 1.2 and 1.3 provide a taxonomy of medical and non-medical uses[23] .

Tables 1.2. Taxonomy of medical applications

Medical Applications	Focus
Cardiovascular Disease (CVD)(MyHeart)	Self-managed Monitoring System of CVD and Real-time Monitoring
Heart Rate Monitoring	Electrocardiogram (ECG), Heart Rate (HR), Body Acceleration, Temperature Sensors
Real-time Monitoring and Analysis of Human Health	Blood Pressure, Body Temperature, ECG, Blood Flow
Health Face	Web-based Remote Health Monitioring
RehabSPOT	Stroke and Physical Dysfunction
Rehabilitation	Improve Rehabilitation and Assisting in Mobility
Comfortable Health Monitoring for New Born (Smart Jacket)	ECG
Kids Health Monitoring System (KiMS)	Temperature and Pulse Rate Sensor
Rehabilitation and Recovery Monitoring	Rehabilitation Exercise Monitoring
IMPAIRED	Low Back Pain
HipGuard	Leg and Hip Position Rotation
Real-time Activity Monitoring	Exercise Monitoring for patients with motor impairment
Fall Detection	Posture of Humans especially elderly people
Abnormal Condition Detection System	Monitors sitting, walking, lying and falling
Neurodegenerative	Parkinson
BASUMA	Health Monitoring (ECG, Reactive Oxygen Sensor, SpO2 sensor, Spirometer)
MobiHealth	Ambulatory Patient Monitoring (ECG)
AID-N	Emergency Response of Blood Pulse, ECG
MAHS	Sprirometer, Pressure, Temperature, Pulse
Code Blue	Motion, Pulse, Oximeter
LifeMinder	ECG, Thermometer, SpO_2, Galvanic Skin Response
ASNET	Remote Monitoring (Temperature and Blood Pressure)
Ayushman	EKG, Blood Pressure, Oximeter, Gyroscopic Sensor
SMART	ECG, SPO_2

Biofeedback	Controlling Emotion such as Stress
Assisted Living	Disable People

Table 1.3 Taxonomy of non-medical applications.

Non-Medical Applications	**Focus**
Golf Training	Wearable sensors used to monitor quality of movements
Soccer Player Monitoring	Routing techniques to monitor soccer player's movement
THE-FAME	Muscle fatigue through sensing accumulation of lactic acid
Fitness Monitoring	Improvement in user's quality of life
Physical State Monitoring	Identifying exhausted player
Performance of Marathon Athlete	Real-time data collection in dense dynamic environment
Biometrics	User authentication
Sweat pH Analysis	Textile-based sensor
Indoor Positioning System	Assists visually impaired person to determine objects
DynaMo	Mobility pattern of players
Baseball Game	Calculates force, torque during baseball game
Precision Analysis of Dart Game	Measurement of speed, acceleration and timing.
Cyclist performance Analysis	Motion sensors used for monitoring lower limb kinematics
Project ProeTEX	Sensor based garments for activity monitoring of fire fighters
Soldiers Activity Monitoring	Estimates the impact of blast and effects on soldier
Management of Notification	Intelligent notification tool
Serious Gaming	Detects stress level and improve effectiveness of games

4.4. Wireless communication standards

WBAN communication is based on a number of wireless standards, including IEEE 802.11 [31], IEEE 802.15.1[32], and IEEE 802.15.4 [31]. These standards (Ad-Hoc, WSN, and WPAN) are made for environments with different characteristics than WBAN, though.

Due to the power consumption of IEEE 802.11 and IEEE 802.15.1, which is too high to support low power WBAN nodes, they are unable to satisfy all of the requirements of

WBAN[33]. The WBAN standard that is most frequently used is IEEE 802.15.4. The standard, however, is unable to ensure data transfer over 250 Kbps or enable high-speed applications [34]. Therefore, IEEE Working Group 6 was created to standardize the MAC layer of WBAN for short-range wireless communications near or inside the human body [35]. The group provided the IEEE 802.15.6 standard, which supports quality of service and allows devices to operate at very low transmit power, thereby ensuring human safety by minimizing the specific absorption rate (SAR) of the device and extending the life of the battery [35]. In April 2010, the IEEE 802.15.6 working group formulated the first draft WBAN communications standard, optimized for nodes on or implanted in the body with low power in various medical and non-medical applications. The latest WBAN standardization is IEEE 802.15.6, which aims to provide an international standard for low-power, short-range, and highly reliable wireless communications in the area around the human body, and supports data rates of data ranging from 75.9 Kbps to 15.6 Mbps. Additionally, the standard uses different frequency bands; narrowband (NB) uses 400, 800, 900 MHz and 2.3 and 2.4 GHz, ultra wideband (UWB) uses 3.1-11.2 GHz, and human body communication (HBC) uses frequencies between 10 and 50 MHz that does not support high-speed transmission, such as video or audio streaming. In addition, the standard proposes a more flexible frame structure at the MAC layer, which supports multiple channel access modes[36]. According to numerous studies such as [37], compared to other standards, the IEEE 802.15.6 standard is more suitable for WBAN communication, especially for latency and reliability.

WBAN is indeed a portable network whose successful implementation faces many major challenges. Battery life of implanted devices is the biggest challenge as the network must last for many years. The Wireless Power Transmission (WPT) system helps solve this problem [38]. However, establishing a power-saving wireless link is a major factor in long-term battery usage. The graphical comparison shown in Figure 1.11 shows the power consumption and data rate obtained by several RF transmitters.

Indeed, since the IEEE 802.15.6 standard [39] supports three physical layers (PHY). Narrowband (NB) PHY, Ultra Wideband (UWB) PHY and Human Body Communication (HBC) PHY. The standard specifies a mandatory PHY for the default mode of operation for communication using IR-UWB pulse radio.

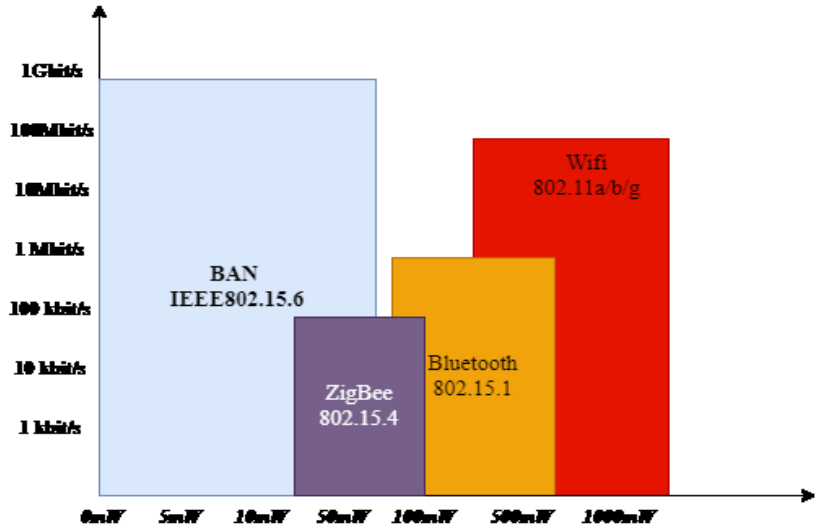

Figure 1.11. *Speed and Range of the different wireless communication standards.*

4.5. Related Work

An abundance of studies on WBANs—from their design to their difficulties in implementation—have been published during the past five years. Implementation and design difficulties, security concerns, diffusion modeling, data routing, energy efficiency, quality of service guarantees, and other practical concerns were all explored in the works cited in[8][40][41][42][43][44]. These papers covered all the bases when it comes to WBANs, from the basics to the technical issues that come with implementing them, from creating routing protocols to ensuring their security.

Using biosensors implanted or worn on the human body, WBANs are designed to continuously monitor the patient's health and trigger an alert in the event of an emergency. Research in [45]summarized the types of sensors utilized in body network systems and how effective they were. The study of WBANs is primarily concerned with the design of WBANs, the fusion of data, and the transmission of data through the network. Sensor placement, power use, and node routing are studied as they pertain to network architecture. Feature extraction, data reduction, and data categorization are the main areas of study in the field of data integration.

Researcher in [46] looked at how much power WBANs use, while researcher in [47] mapped out efficient ways to connect sensors like medical devices to the rest of the network.

Security algorithms shield the network to safeguard data in all its forms, ensuring that it can be verified, kept private, and kept in a state of perfect integrity.

The authors of [48][49] explained that the security of a secure communication session between biosensor nodes in an unfriendly environment must be based on the privacy of the security mechanisms so that the data can be made visible only to the authorized person. There was a lack of research that addressed both security and energy usage, which are both major issues but were not jointly addressed in any of the studies cited here. This review article's primary objective is to address this knowledge gap by looking at the twin concerns that the WBAN must face: security and energy efficiency.

After presenting a high-level overview of WBANs and WSNs in [50], the authors delved deeper into the topic, exploring the security needs of the WBAN in great detail. After introducing two concerns of security and privacy in the WBAN, this article attempted to examine the significance, need, and challenges of protecting the patient's privacy when collecting and transmitting their essential information. Energy efficiency and cost reduction were also mentioned as important goals toward which a complete and effective security system should strive. As important as it is to reduce energy consumption after implementing security measures, no concrete strategies are provided to do so in this study.

In [51], the authors do extensive study into the needs and difficulties of the WBAN. After thoroughly reviewing WBAN apps, they zeroed in on the specific needs and difficulties of the network. The article's analysis of technology and standards for data transmission in the WBAN stands out as a special feature. Next, a few words were said on why and how the WBAN may benefit by consuming less energy. This article has some flaws, one of which is that the security and privacy problem it raises is only touched on briefly. In this paper, we explore the use of artificial intelligence algorithms and protocols in the WBAN to close this gap and improve efficiency. The assaults are further broken down into categories, and the general and security issues of the WBAN are outlined.

5. UWB technology

The ultra- large band (ULB) technology, called ultra-wideband (UWB) because of its English abbreviation, was dedicated twenty years ago to military communications and radar applications. Its development has passed an important period in recent years. In February 2002, the United States Communications Regulatory Commission (FCC- Federal Communications Commission) implemented the UWB technical regulations, which authorize the use of the 7.5 GHz continuous frequency band between 3.1 GHz and 10.6 GHz, license-free suitable for consumer telecommunication application.

Since 2002, this 40-year-old technology has actually been implemented. It is based on a very short pulse transmission system, which allows it to provide high-speed transmission speeds of up to 480 Mbit / s for a range of 15 meters. Therefore, UWB uses a very wide frequency band (between 3.1 GHz and 10.6 GHz) to exchange data and complies with the IEEE 802.15.3 standard.

The FCC approved 2002 UWB communications in the frequency band between 3.1 and 10.6 GHz in the United States[52]. In Europe, the European Conference of the Post and Telecommunications Regulatory Authority (CEPT) began to take an interest in UWB communications in 2001 and took certain decisions in 2006 as shown in Figure 1.12. The CEPT has proposed a frequency band of 6 to 8.5 GHz for UWB communications [53]. To ensure coexistence with other wireless standards with minimal interference, regulators have associated very low transmit power with these frequency bands. The final determination of the regulations marks the start of a new era for research dedicated to UWB technology. Driven by several labs and companies (such as Staccato, Pulse-Link, and WiSair), many interest groups and standardization will form marketable products. In 2007, the Institute of Electrical and Electronics Engineers (IEEE) proposed the IEEE 802.15.4a standard for low-speed applications, [31].

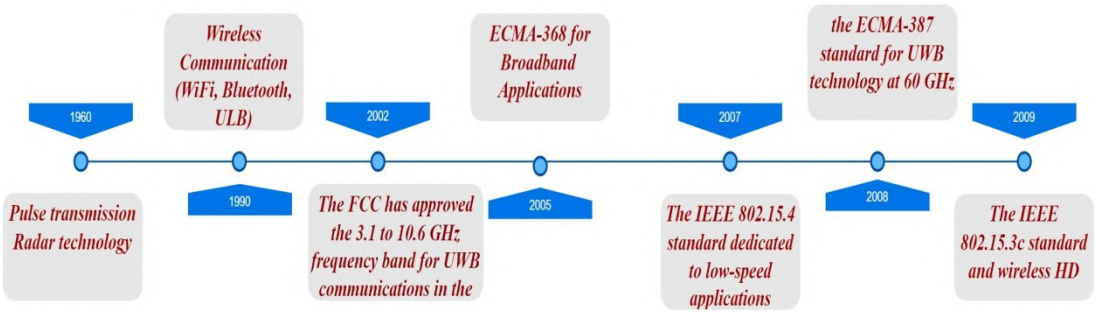

Figure 1.12. *History of UWB*

5.1. General characteristics of UWB technology

The fundamental principle of pulsed UWB technology is based on a signal with a strictly limited transmission time, where the duration of the signal is of the order of a few nanoseconds, as opposed to a narrow band signal that is transmitted continuously. Therefore, compared to the NB (Narrow Band) signal, which occupies a narrow frequency band, the frequency analysis of the UWB signal has a wider spectrum occupation. This is illustrated in Figure 1.13, which qualitatively compares the spectrum of the UWB signal to the NB signal.

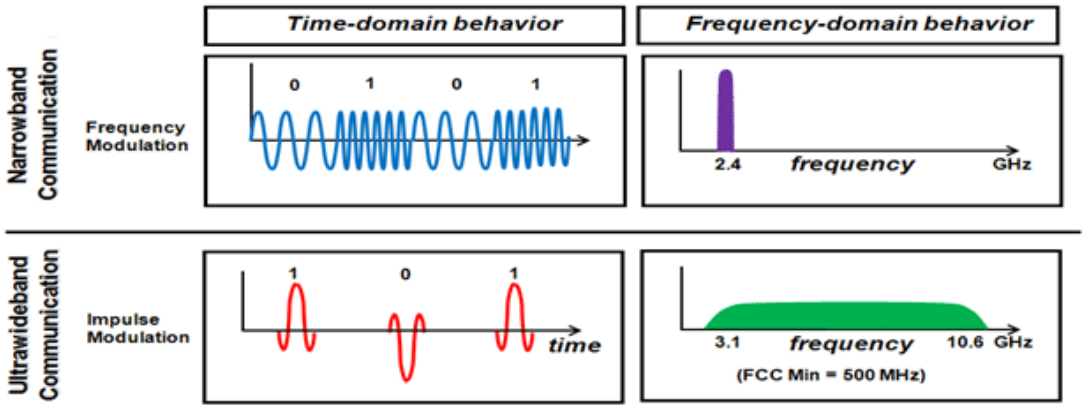

Figure 1.13. *Comparison of spectral characteristics between NB and UWB signals*

UWB technology exposes important characteristics. We can notice that the sensitivity to fading associated with multipath propagation is very low. This is because multipath fading will reduce the efficiency of traditional (NB) communication systems. Regarding UWB communication, the signal is transmitted at a larger bandwidth, where the temporal resolution is very good.

UWB signals are more discrete and potentially more difficult to detect than conventional radio communication signals because they occupy a large bandwidth and thus have a very low power spectral density equal to -41.3 dBm/MHz. It can be transmitted at a power spectral density level well below the noise floor of conventional radio communication receivers and can be transmitted with a unique synchronization code at millions of bits per second.

These features ensure that the signal transmission is protected and has a lower probability of detection and interception. One of the key components required by the standard is the simplicity of the system provided. Compared with NB transceivers, UWB transceivers have a relatively simple architecture, which can reduce equipment costs. In addition, the pulsed UWB method offers a promising solution to RF spectrum deficiency for new services by allowing coexistence with other radio systems with little interference. This coexistence has the advantage of avoiding the license fees that all other radio service providers have to pay.

The benefits of UWB technology that have been outlined above make it the best option for WBAN applications. Numerous implementation technologies have been introduced because UWB regulations do not specify a particular type of modulation technology. UWB pulse radio (IR-UWB) and multi-band UWB (MB-OFDM) are the two most often employed technologies.

IR-UWB is a carrierless modulation technology based on the transmission of very narrow pulse sequences. As a result, the IR-UWB system occupies more bandwidth, which leads to a high data rate (up to 500 Mbps [54]) and good positioning capabilities. These advantages open the door to the adoption of IR-UWB technology in many applications, such as radio frequency identification (RFID), ground radar penetration, radar detection, location tracking, and medical imaging [55].

The shape of the pulse is very important in the IR-UWB transceiver system because it determines the frequency spectrum of the transmitted signal. It is necessary to design an IR-UWB pulse generator, which is a key component of the transmitter, which can generate accurate pulse shapes and comply with the Federal Communications Commission's (FCC) mandatory spectrum mask [56][57].

5.2. Definitions and regulations

5.2.1. FCC Rule

The Federal Communication Commission (FCC) designated a frequency spectrum mask for UWB applications in the 3.1GHz to 10.6GHz frequency band in order to shield traditional communication systems from interference. There are four masks available for vehicle radar systems, through-wall UWB imaging applications, interior UWB applications, and outdoor UWB applications, correspondingly [1,3].

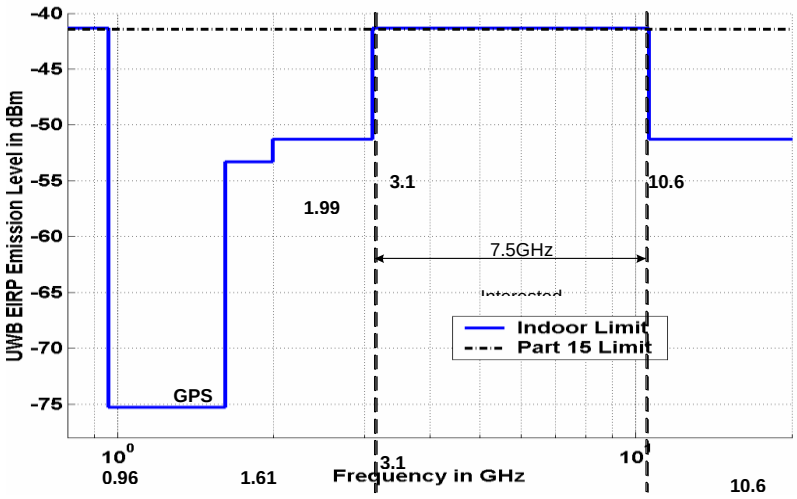

Figure 1.14. *FCC Spectral Mask*

The first sort of emission is taken into account in the design because this project is an indoor UWB application. The FCC's emission mask for indoor UWB applications is depicted in Figure 1.14.

The average output power spectrum density for indoor applications is restricted to -41.3 dBm/MHz between 3.1GHz and 10.6GHz and to -53 dBm/MHz between 1.99GHz and 3.1GHz. This restriction coexists with the well-established general emission restrictions set forth in FCC Part 15 for regulated radio interference [58]. The short pulse frequency content for this project lies in the range of 3.1GHz to 10.6GHz. As a result, the maximum transmitting power spectrum density level in this 7.5GHz frequency band is -41.3dBm/MHz. It is important to note that, despite FCC regulation of the UWB spectrum, the industrial standardization process has not yet been completed. The FCC masks serve as a model for restrictions in other nations, including Canada.

5.2.2. UWB systems by radio pulse (IR-UWB)

Given the recent spectrum allocation and the new definition of UWB adopted by the FCC shown in Figure 1.15, any transmitted signal that meets the FCC's UWB spectrum requirements can be used. Of course, this isn't limited to the pulse radio technology or broadband broadcast spectrum the company has already provided. This also applies to any technology that uses a bandwidth greater than 500 MHz in the authorized spectrum mask and has limitations on current emission restrictions [59]. The power spectral density (PSD) measured in a 1 MHz bandwidth must not exceed the prescribed FCC limit.

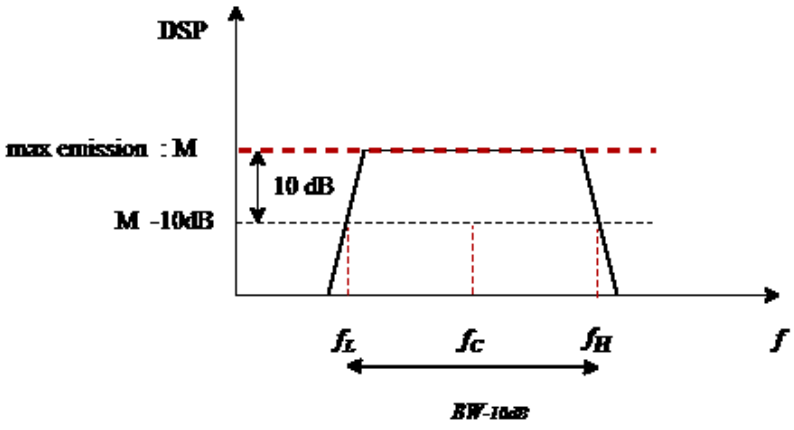

Figure 1.15. *Representation of the quantities (B-10dB, f_L, f_H, f_C), on a frequency spectrum (DSP), making it possible to define the occupied band at -10dB within the framework of the American regulations of the FCC*

PSD is directly related to the amplitude, bandwidth, and duty cycle of the UWB signal, the latter being defined as the ratio of signal repetition rate to bandwidth. This indicates that for a fixed PSD, the narrower the bandwidth, the smaller the authorized repetition rate for a fixed amplitude. UWB communication systems by radio pulses can be classified into two categories.

5.2.2.1. The single-band approach

The single-band approach consists of transmitting a low-duty cycle signal in the baseband, the spectrum of which occupies the entire available frequency band from 3.1 GHz to 10.6 GHz. It is characterized by the emission of pulses of short duration, as shown in Figure 1.16. This naturally provides greater bandwidth to the signal, as the duration is less than 1 ns and the absolute bandwidth criterion is validated. This approach presents little flexibility in the use of the radio spectrum and requires high-performance RF component solutions. Different pulse patterns are introduced for this type of system. The most commonly used are Gaussian pulses and their derivatives, which have long been referenced for UWB signals, pulses based on polynomial Hermite functions, Rayleigh pulses, and pulses modeled by filters (impulse response generator filters).

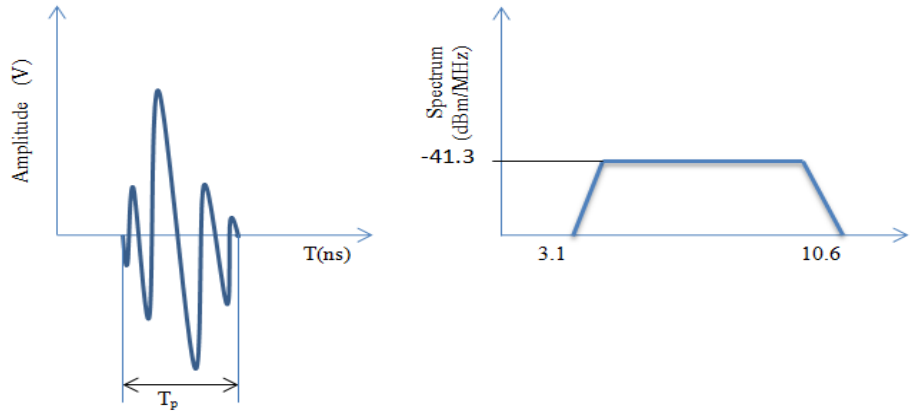

Figure 1.16. *(a) Time response, (b) Frequency response of a single-band UWB signal*

5.2.2.2. The ULB Direct Sequence approach

The Direct Sequence UWB (DS-UWB) method, also called Direct Sequence Code Division Multiple Access DS-CDMA, consists of dividing the frequency band allocated by the FCC into two double bands: a low frequency band with a width of 1.75 GHz of 3.1 GHz to 4.85

GHz and a high frequency band of equal width 3.5 GHz ranging from 6.2 GHz to 9.7 GHz as shown in Figure 1.17. However, this method can avoid the 5 GHz UNII frequency band used by Wi-Fi technology. The modulation method used in this method is UWB spread spectrum modulation or DS-UWB (Direct Sequence UWB) recommended by the group UWB.

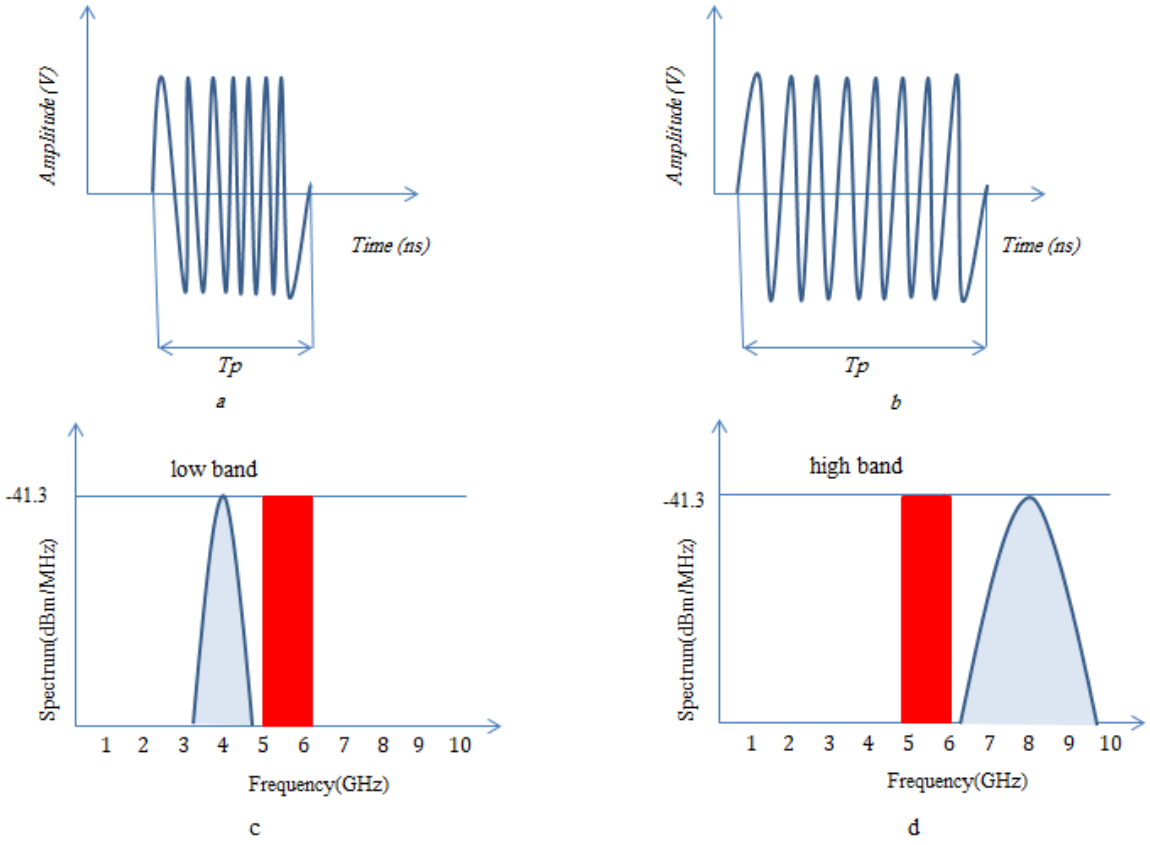

Figure 1.17. *(a) UWB low-band signal, (b) UWB high-band signal, (c) Low-band spectrum of the dual-band approach, (d) High-band spectrum of the dual-band approach*

Both bands can be used individually or simultaneously. This provides additional flexibility in system functionality. Unlike traditional DS-CDMA systems, which transmit spread spectrum signals, DS-ULB uses wideband pulses to effectively occupy a wide spectrum.

5.3. Techniques for modulating UWB signals

With the IR-UWB system, the information bits are first carried by short pulses that are directly modulated in the time domain before being sent out for transmission. In this section, a few widely used pulse modulation methods are covered. These are biphase modulation, on-off keying (OOK), pulse-amplitude modulation (PAM), pulse-position modulation (PPM) and

linear frequency modulation also called Chirped Spread Spectrum Frequency Shift Keying (CSS-FSK). In terms of system design factors including resistance to interference and noise, data rate, circuit complexity, and total system cost, various modulation techniques have varied benefits and downsides. This work used the CSS-FSK technique

5.3.1. Pulse-Amplitude Modulation

A one-dimensional signal modulation called pulse-amplitude modulation (PAM) changes the narrow pulse's amplitude to two values that correspond to either bit 1 or bit 0 [4]. Conventionally, data 1 is represented by a pulse with a high amplitude, and data 0 by a pulse with a low amplitude. The equation allows for the expression of the modulated signal.

$$s(t) = \sum_{m=1}^{\infty} a_m \,.\, P(t - mT\,) \tag{1.1}$$

This formula ∞, denotes continuous transmission of data bits, P(t) denotes an incredibly tiny energy pulse, and am denotes the two possible amplitudes of an information bit, either 1 or 0. The pulse period is T. (pulse duration and the rest in one cycle). An illustration of the output signals via PAM is shown in Figure 1.18.

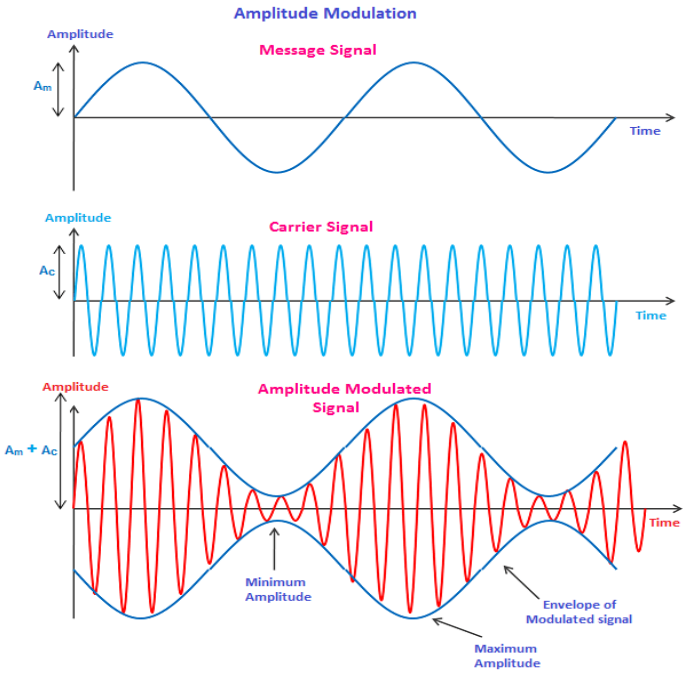

Figure 1.18. *Pulse-amplitude modulation*

Due to the fact that PAM only needs a single polarity to represent data, implementation is rather straightforward. PAM-type demodulators use an energy detector is used by PAM-type

demodulators to recover data. Nevertheless, PAM is susceptible to noise, and attenuation can muddle the difference between "1" and "0"[60].

5.3.2. Pulse inversion modulation (BPSK)

Pulse modulation by polarity inversion (BPSK: Binary Phase Shift keying), is also known as biphasic modulation. BPSK modulation is the simplest form of PSK. It uses two distinct phases: 0° and 180°. The concept is illustrated in Figure 1.19. Thus, the transmitted signal for this modulation can be expressed by the equation

$$s(t) = \sum_{k=1}^{+\infty} a_{k,l}\, p(t - kT) \qquad (1.2)$$

Where k represents the bits transmitted, p(t) is the waveform of the UWB pulse, T is the repetition period of the pulse, and $a_{k,l}$represents the lth bit of data, with $a_{k,l} = -1$ if k = 0 and $a_{k,l} = +1$ if k = 1

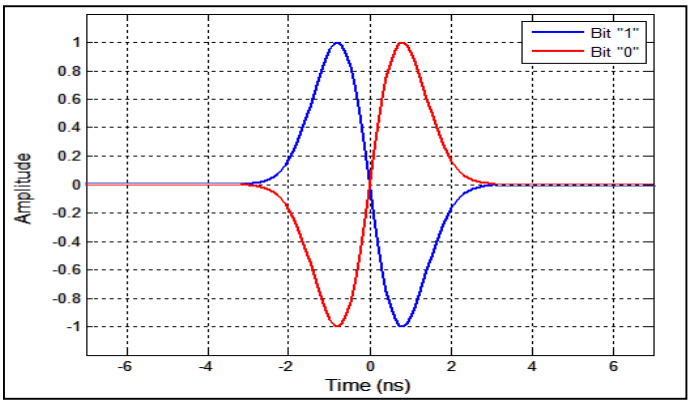

Figure 1.19. *Example of pulse waveforms used for pulse polarity inversion modulation*

5.3.3. Pulse Position Modulation (PPM)

Pulse Position Modulation (PPM) is a modulation technique used to transmit data where information is encoded on the position of the transmitted pulse by shifting it within a predefined time window. While a time-shifted pulse respecting a specific time reference represents a "1" data bit, a "0" bit is represented by a pulse with no time shift (Figure 1.20). Equation (1.3) provides the general signal model for PPM.

$$s(t) = \sum_{k=-\infty}^{+\infty} a_k \, p(t - kT) \tag{1.3}$$

Where ak is the amplitude of the pulse p(t) and T is the frame duration.

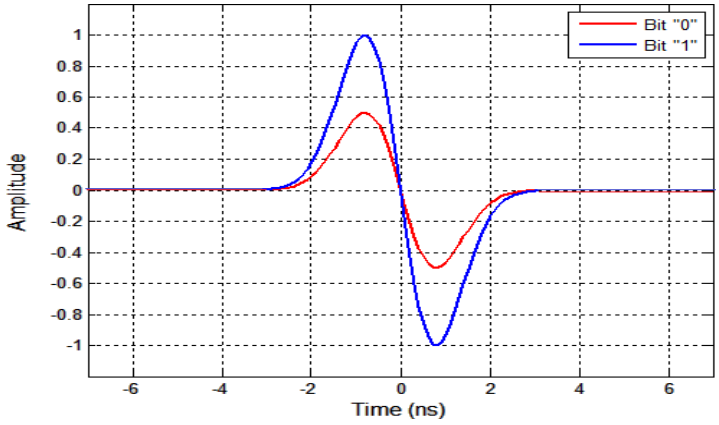

Figure 1.20. *Example of Pulse Waveforms Used for Pulse-Amplitude Modulation*

5.3.4. On-Off Keying (OOK) modulation

(OOK) is the simplest form of pulse modulation, in which the transmission of a pulse represents a "1" data bit and its absence represents a "1" data bit. 0" (figure 1.21). The general signal model for OOK is given by:

$$s(t) = \sum_{k=0}^{+\infty} a_k \, p\left(t - kT_f\right) \qquad with\ a_k = 1{,}0 \tag{1.4}$$

Where a_k is the amplitude of the pulse, which can have the values 1 or 0, and T_f is the duration of the frame. Although it is a simple modulation scheme, it is very sensitive to noise. When no pulse is transmitted to indicate a "0" bit, the spurious signals can add up and cause the receiver to make an incorrect bit decision.

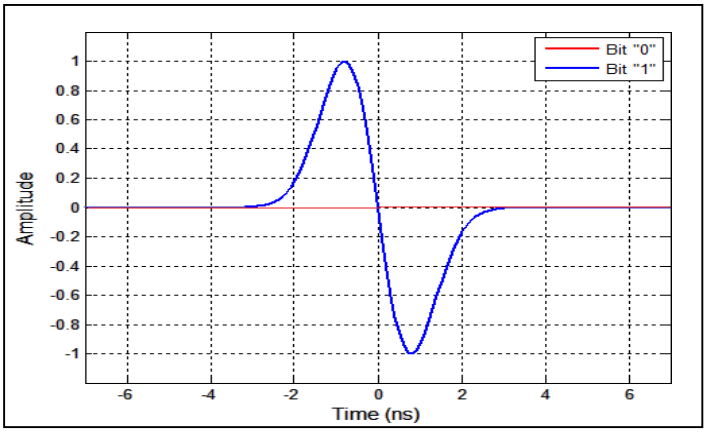

Figure 1.21. *Example of Pulse Waveforms Used for On-Off Keying Modulation*

5.3.5. Chirped Spread Spectrum Frequency Shift Keying (CSS-FSK) modulation

CSS-FSK is a modulation technique used to generate a sinusoidal signal characterized by a linear change in frequency. This technique has the property of pulse compression (Figure 1.22) and therefore spectrum spreading (Spread Spectrum). Among the reasons for choosing this technique, the good performance in terms of distortion and interference rejection which allows a minimum of energy consumption for its implementation. Since this method is difficult to detect when operating at low transmit power, it is convenient for sensor network applications. The chirp signal can be represented by equation (1.5):

$$s(t) = A.\cos\left(2\pi f_0 t + \varphi(t)\right) \qquad 0 \leq t \leq T \tag{1.5}$$

Where the initial chirp frequency is f_0, and T is the duration of the chirp pulse. The Chirp FSK modulation technique, also called double band (dual band) Binary FSK (BFSK) makes it possible to assign a fixed sub-band B0 for the bit "0" and a sub-band B1 for the bit "1" instead of assigning a particular frequency to each bit.

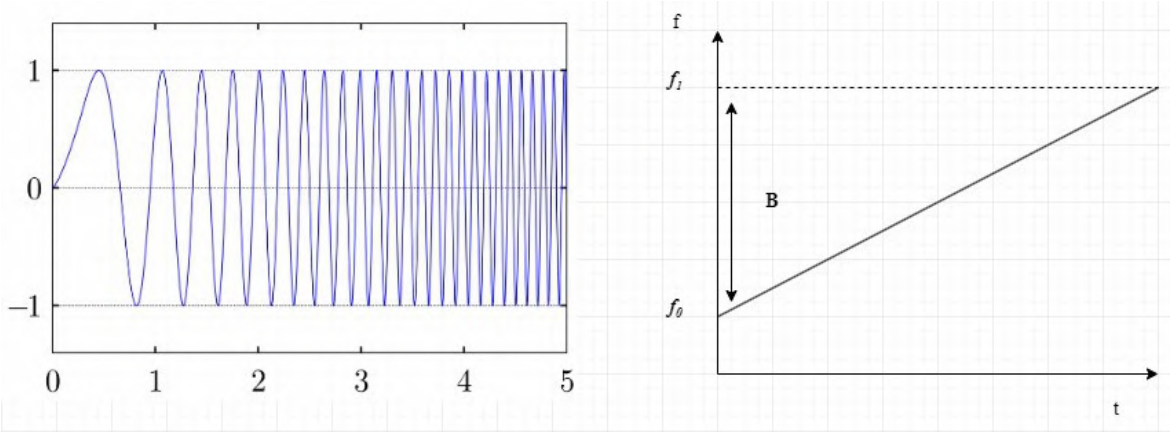

Figure 1.22. *Chirp signal and frequency versus time*

5.4. UWB Signal Detection

In order to reduce transceiver complexity while maintaining the maximum degree of accuracy, the demodulator at the receiver performs the role of retrieving the original data information from the modulated pulse trains. The two most common types of receivers for UWB signals which operate without a carrier are autocorrelation and rake receivers.

The incoming signal is matched with a waveform template by the correlation receiver before the operation of match filtering is carried out, and the output is integrated. When using matched filtering, also known as coherent detection, the oscillator output at the receiver and the carrier of the received signal must be phase synced for optimum detection. Figure 1.23 illustrates the best detection technique using a correlator[61].

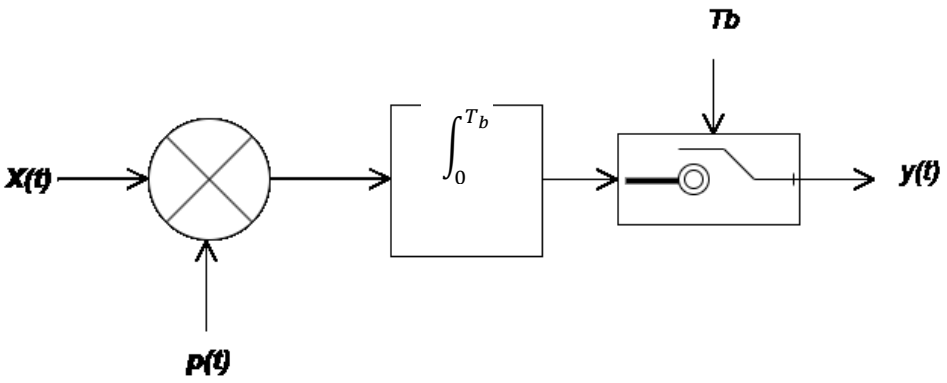

Figure 1.23. *Optimum Signal Detection using a correlator.*

Detected signal *y(Tb)* at the output of the correlator can be modeled as:

$$y(T_b) = \int_{t-0}^{t-T_b} x(\tau)p(\tau)d\tau \quad (1.6)$$

Where

$x(\tau)$ is the input signal

$p(\tau)$ is the pulsed signal

For each potential pulse position, the received signal and the waveform template are correlated by the UWB receiver, and the results are then sent to the baseband for further processing. The received signal $r(t)$, in the absence of interference from multiple access, can be modeled as:

$$r(t) = s(t) + n(t) \quad (1.7)$$

where

s (*t*) is the transmitted monocycle

n(*t*) is the zero mean white Gaussian noise with power spectral density No/2

Coherent detectors are used in UWB systems because they have lower bit error rates than their non-coherent counterparts [22].

5.5. Bandwidth of UWB Signals

UWB uses extremely short pulses to transfer data, necessitating a very large instantaneous bandwidth. The FCC specifies that a UWB signal must have a minimum bandwidth of 500 MHZ or a fractional bandwidth of at least 0.20 when measured from the -10db emission point. Fractional bandwidth defined as (B_f) is

$$B_f = \frac{2(f_h - f_l)}{(f_h + f_l)} \quad (1.8)$$

where

f_h is the maximum frequency determined by measuring it -10 dB below the peak emission point.

f_l Lower frequency is determined by measuring it -10 dB below peak emission point.

The Federal Communication Commission (FCC) allocated 7.5 GHz of unlicensed spectrum

bandwidth from 3.1 GHz to 10.6 GHz for UWB communications under strict emission limit. Figure 1.24 shows spectral masks for indoor application.

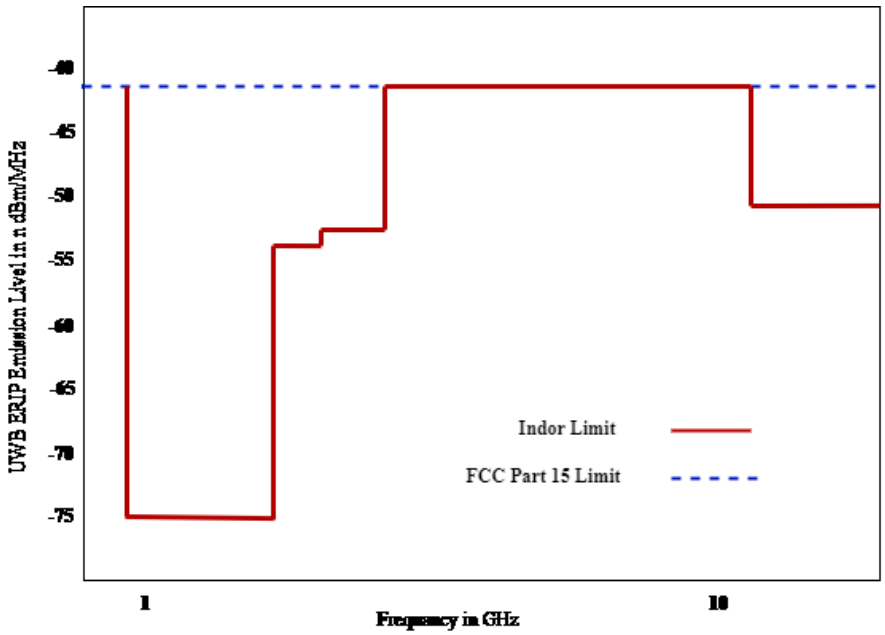

Figure 1.24. *Spectral Mask for Indoor Applications*

UWB signals may be transmitted at PSD levels as high as -41.3 dBm, as demonstrated in Figure 1.24. Existing 802.11a and WiMax users may cohabit in the overlapping frequency bands thanks to this emission restriction. Spectral masks for outdoor use are seen in Figure 1.25.

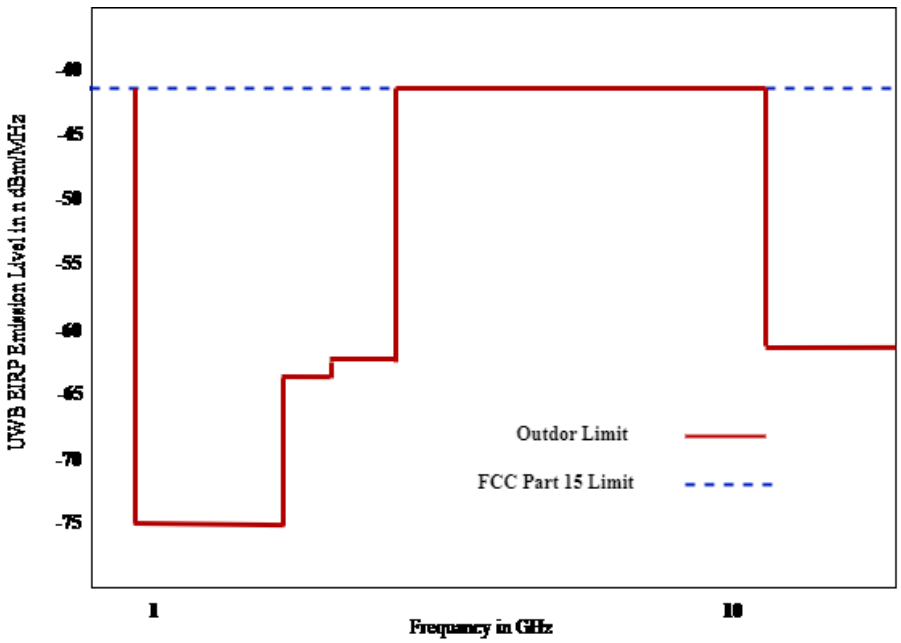

Figure 1.25. *Spectral Mask for Outdoor Applications*

In order to guarantee that GPS services and UWB systems can coexist, Figure 1.25 illustrates how outdoor UWB signals outside of the band have more attenuation than inside UWB signals.

5.6. UWB Channel Capacity

UWB uses up a lot of bandwidth instantly, as was already explained. According to the well-known Shannon's link capacity calculation, UWB technology offers a significant increase in channel capacity:

$$C = B.\log(1 + SNR) \tag{1.9}$$

The connection capacity has a logarithmic relationship with the signal-to-noise ratio and is directly related to bandwidth (SNR). A very low radiation power is required to produce a high data rate when the signal bandwidth is big due to the linear connection between channel capacity and bandwidth. In contrast to narrowband systems, which increase the data rate by using high transmission power levels, UWB systems increase the data rate by delivering signals over a wide frequency range at low power levels.

6. Conclusion

In the first chapter, we were able to introduce different communication techniques for wireless sensor networks. By studying different wireless communication technologies for WSN systems, we can conclude that UWB has great performance flexibility on the following criteria: consumption, cost, complexity, size, speed, and radio range. Additionally, IR-UWB technology has an excellent temporal resolution, making it capable of efficient and accurate localization.

Wireless sensor networks could be used to help with security and medical monitoring of patient health, among other things.

As part of our thesis work, we mainly target WBAN network systems. In the case of these applications, the low consumption aspect ,reduce the noise figure , increse the gain and good linearity are the most priority constraints, so our communication system will have operating autonomy as long as possible, in order to monitor the state of the network and assist in the maintenance process. To this end, the IR-UWB technology is, in our opinion, the most

promising for this type of application, thanks to the low power consumption possibilities it offers.

In the next chapter, we discuss the UWB transceiver architectures. the various RF transceiver designs as well as the key features that define the standards by which an RF transmitter's performance is measured will be explained. We will introduce the first important part which is the Low noise amplifier(LNA) from the receiver.

Chapter 2

UWB transceiver architectures and LNA design

1. Introduction

Ultra-Wideband (UWB) transceiver architectures are used for wireless communication systems that operate over a very wide frequency band. These architectures are designed to support high data rate and short-range communication applications, such as wireless sensor networks, high-speed data transfer, radar systems, and location-based services. There are two main types of UWB transceiver architectures: direct conversion (also known as homodyne) and superheterodyne. In this chapter, we will present the different architectures of RF transmitters and receivers as well as their fundamental characteristics. We will also focus on the advantages and disadvantages of each architecture to highlight the selection criteria of the radio frequency architecture. The choice of UWB transceiver architecture depends on the specific requirements of the application in terms of performance, cost, power consumption, and complexity.

Also, we explain the receiver's performance from the noise figure and sensitivity, the conversion gain, and linearity. In this chapter, we will establish the study of choosing an LNA that should be the most suitable for our UWB sensor node application. This is after a comparison and an optimization made based on the use or not of the inductors in the LNA circuit since the inductors thwart the challenge of the minimum surface and the possibility of integration on a single chip. Then, we will start the analysis and optimization of the front-end composed of the chosen LNA BALUN and the fully differential doubly balanced passive mixer in voltage mode with a duty cycle of 25% studied and proposed in the next chapter (see Chapter 3). The performance of gain, noise figure, linearity, and S11 are simulated for the proposed front-end and then a comparison with other front-ends is presented in other works.

2. Radio frequency transceiver architectures

The diagram in Figure 2.1 represents the three basic elements of a wireless communication chain: the transmitter, the receiver, and the channel. The data to be transmitted is processed by the transmitter to form a baseband modulated signal, which is amplified, then filtered, and reaches the antenna at the radio frequency. In the case of implants, the channels consists of

air, skin surface, and adipose tissue, which characterize the source parameters of transmission signal attenuation, thermal noise, and interference-induced losses.

Attenuation is due to the distance between transmitter and receiver, while fading is a function of time, geographic location, carrier frequency and the different paths taken by the transmitted signal. On the receiver, the RF signal is picked up by the antenna, filtered, amplified, and then frequency-translated to obtain baseband signals. Finally, the signal is processed and demodulated by a DSP (Digital Signal Processor). In the following, we will present the latest techniques for different transmitter and receiver architectures, because it is very useful to find a balance between performance and power consumption, which means making the right choices when designing.

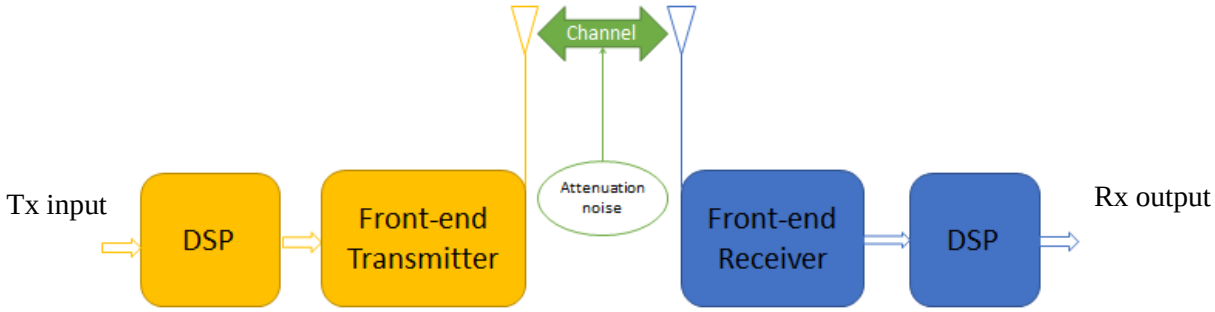

Figure 2.1. *Diagram of a chain of transmission*

The radio frequency architecture is determined on the basis of technical standards and strategic standards, such as the cost of the product. The integration of the radio architecture is strongly aimed at finding a "price/performance" compromise. Obviously, the signal recovered at the receiver's output must be close to the signal at the transmitter's input.

2.1. Superheterodyne architecture

2.1.1. Transmitter architecture

In the transmission chain, the analog information is first digitally processed in the baseband by the DSP, generating the I and Q signals as shown in Figure 2.2.

These digital modulation signals are orthogonal in the complex plane. Digital modulations using this type of signal are widely used in wireless communications as they provide a low bit error rate, higher spectral efficiency, and superior power efficiency.

In the case of the superheterodyne architecture, due to the use of the first local oscillator (LO_1), the I/Q modulator recombines the I and Q signals of the DSP into a single signal to achieve the intermediate frequency (IF). The second local oscillator (LO_2) associated with the mixer makes it possible to transpose the modulator signal around the carrier frequency of the channel (F_{RF}). The power amplifier is used to provide useful power for transmission. Eventually, the bandpass filter before the antenna will suppress any signals generated outside the transmission band.

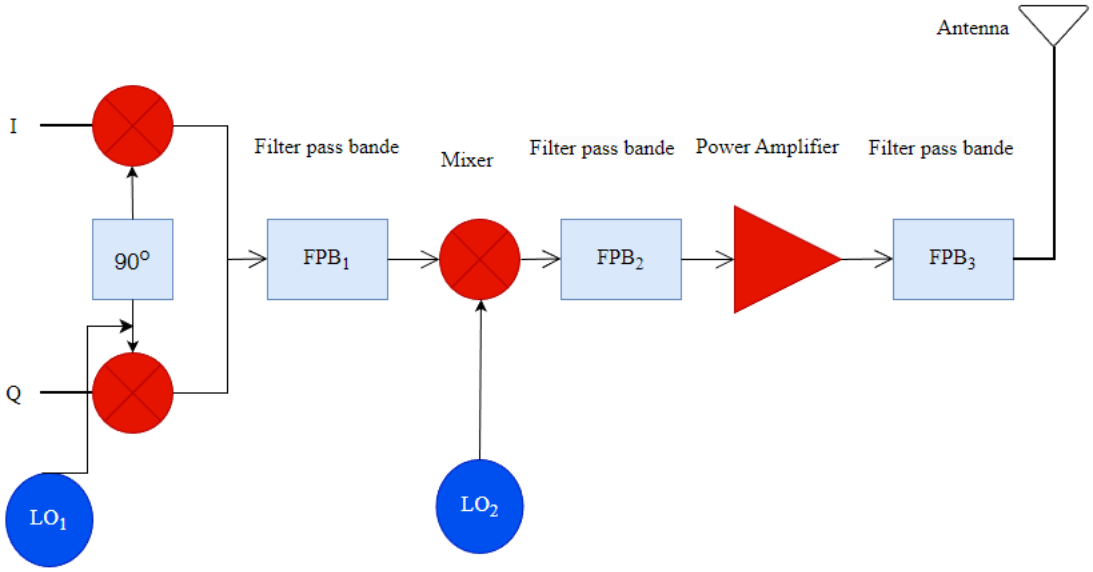

Figure 2.2. *Block diagram of the superheterodyne transmitter*

2.1.2. Receiver architecture

The superheterodyne receiver is one of the most popular discrete radio architectures and is characterized by excellent performance such as selectivity and sensitivity [62]. Due to its performance, it is the best compared to other receiver architectures. Figure 2.3 shows an example of a superheterodyne receiver.

The first block in the receive chain is the RF filter, which is used to select the standard receive frequency band used. Of course, it is desirable to remove out-of-band frequencies as much as possible, but there is a trade-off between the attenuation of these frequencies and the loss due to the insertion of the filter. As the noise figure of the receiver increases, this loss is critical. Usually, this discrete filter is made of ceramic or SAW (surface acoustic wave) technology.

Ceramic filters are usually the first choice, especially around 1 GHz due to their low insertion loss and better attenuation [63].

After the band pass filter is the LNA (Low Noise Amplifier), which can amplify the required signal with low noise. In this way, the contribution of the following stages to the noise figure of the receiver is reduced.

by using the mixer controlled by the local oscillator LO2 shown in Figure. 2.3, the frequency of the mixer (F_{LO}) is equal to the difference between F_{RF} and IF, so that the F_{RF}signal from the antenna is converted into an intermediate frequency (IF). This mixing operation results in obtaining the frequency components at the difference frequency (F_{LO}-F_{RF}=IF), but also in obtaining the sum frequency (F_{LO}+F_{RF}). The latter can be easily eliminated by low-pass or band-pass filtering.

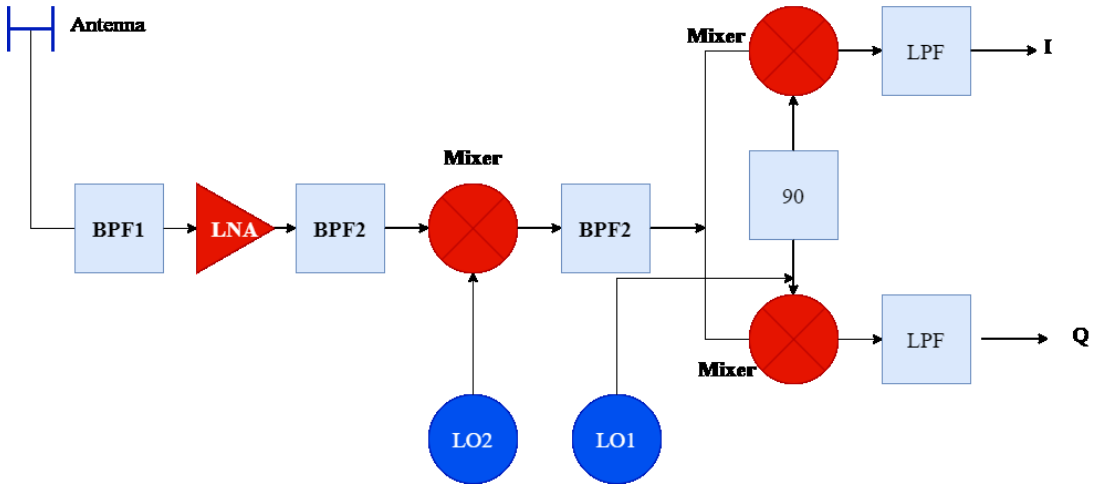

Figure 2.3. *Illustration of a heterodyne receiver chain.*

The choice of the intermediate frequency is not easy. In fact, the use of the intermediate frequency brings several difficulties including the frame rate. From the previous equation, we noticed that a frequency (called the image frequency) multiplied by the mixer is also converted into an intermediate frequency. In fact, the cosine function is even and there is no difference between negative and positive frequencies. Therefore, it also allows the signal present on the antenna and located at the frequency (LO-IF) to be converted into the IF frequency. The existence of an image frequency is a serious problem, because each wireless communication standard imposes restrictions on the signals sent by users in its application frequency band, but cannot handle the signals of external interference.

However, through this mixing operation, the signals appearing at the frequency of (F_{LO}+ IF) and (F_{LO}-IF = F_{RF}) at the input of the mixer are converted to the intermediate frequency FI. Only the channel at the FRF frequency will be received, so the other channel forms a spurious line called the "image frequency". Since the frame rate is converted directly into a useful channel, it must be removed. For this, the first solution consists in using a selective filter (FPB2) inserted before the mixer illustrated in figure 2.3. The greater the IF, the more flexible the constraints imposed on the filter, since the difference between the FRF frequency of the useful signal and the image frequency is 2xIF. However, the intermediate frequency cannot be chosen too high, because in this case the constraints on the quality factor imposed on the channel filter (FPB3) will become too strict.

The second bandpass filter can follow the LNA. Typically, this filter may be needed to achieve sufficient first conversion frame rate attenuation. However, in the case of using an image rejection mixer, if the required frequency band selectivity can be provided by the first frequency band selector filter, the use of this filter can be avoided [61]. After the first IF filter, a variable gain IF amplifier can be used. The IF signal is then transposed to baseband and processed in the digital domain.

2.1.3. Advantages of superheterodyne architecture

This architecture offers good performance in terms of selectivity and sensitivity and can be used with high frequency precision over a wide frequency band. In addition to using a large number of functions, this offers the possibility of a better distribution of the constraints of the system in the reception chain.

2.1.4. Disadvantages of superheterodyne architecture

The superheterodyne architecture raises issues related to the use of multiple frequency conversion stages, such as the frame rate that must be considered when designing the receiver. Also, the IF filter used is external, so integration can be a major problem because it cannot have a high quality factor. These SAW technology or ceramic filters are very expensive and take up a lot of space. There is a lot of research on integrating SAW components on silicon and other semiconductor substrates, but currently, there is no choice.

Another major drawback of the superheterodyne architecture concerns half of the intermediate frequency. This problem reflects the fact that the signal on the antenna is converted to IF/2 at the perfect frequency between F_{RF} and FOL. This frequency is a priori outside the useful band

at the IF frequency. However, the mixer is a non-linear element, so its 2nd harmonic frequency simply falls back to the useful channel (at the IF frequency), which becomes very annoying. In order to reduce the negative effects of this phenomenon, the mixer must have low second-order distortion (this is usually the case in a differential architecture). In addition, as shown in Figure 2.3, the superheterodyne architecture requires the use of bandpass filters needed to select the receive frequency band (filter FPB1) and channel (filter FPB3), but these are difficult to integrate and therefore expensive. However, despite its superficial complexity, this architecture is still considered the most reliable reception technology.

2.2. Homodyne or Zero-IF architecture (Direct Conversion)

2.2.1. Zero-IF Transmitter architecture

In the case of the homodyne (or direct conversion) architecture, for the following reasons, the I/Q modulator recombines the I and Q signals generated by digital processing into a single signal, and this time carries them directly to the carrier frequency (F_{RF}) of the channel To the single local oscillator OL as shown in Figure 2.4.

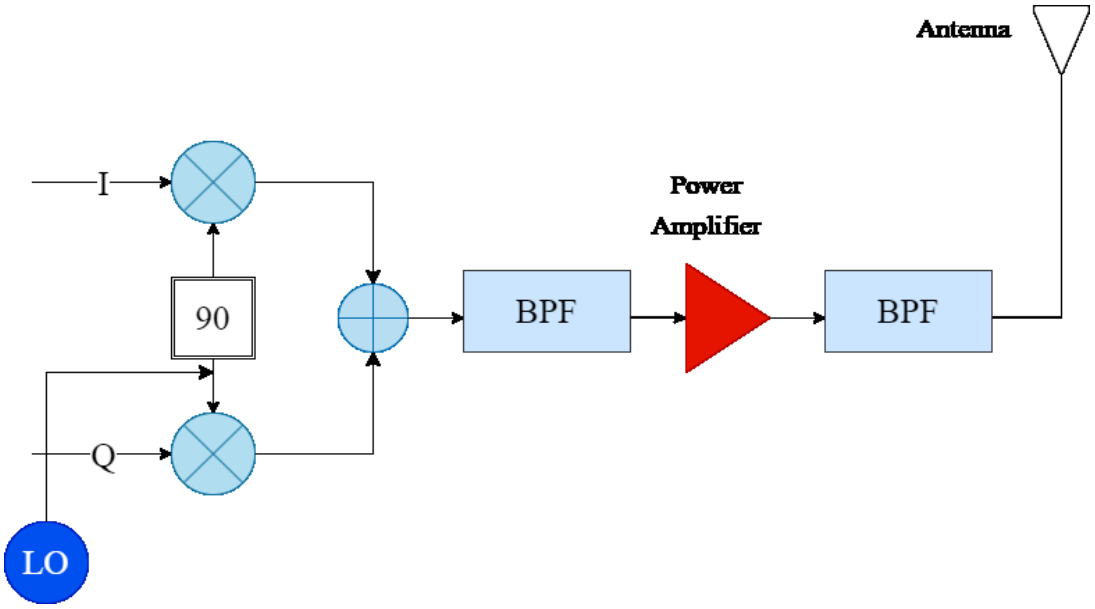

Figure 2.4. *Block diagram of the homodyne transmitter*

Therefore, baseband signals (I and Q) are directly converted to DCRF frequencies without the use of intermediate frequencies (IF). This is why this architecture is also called zero-IF architecture. Finally, the bandpass filter before the antenna will remove any signals generated outside the transmission band.

2.2.2. Zero- IF Receiver architecture

The principle of homodyne (or direct conversion) receivers, as shown in Figure 2.5, was invented decades ago [64]. Over the past ten years, it has been extensively researched due to its insensitivity to frame rate and is more suitable for monolithic integration than superheterodyne receivers [65].

Like the superheterodyne receiver described above, the first two blocks of this type of receiver are the receive band selection filter and the LNA. If the selection of the required frequency band can be completed with a single filter, the second bandpass filter can be omitted.

After filtering and amplifying the required frequency band, the signal undergoes quadrature frequency conversion of baseband I and Q signals. These signals (I and Q) are essential for phase and frequency modulation because the two sidebands of the RF signal contain different information, and if they overlap without dividing into two phases, it will cause irreversible damage[66]. The low pass filter allows you to select the desired channel.

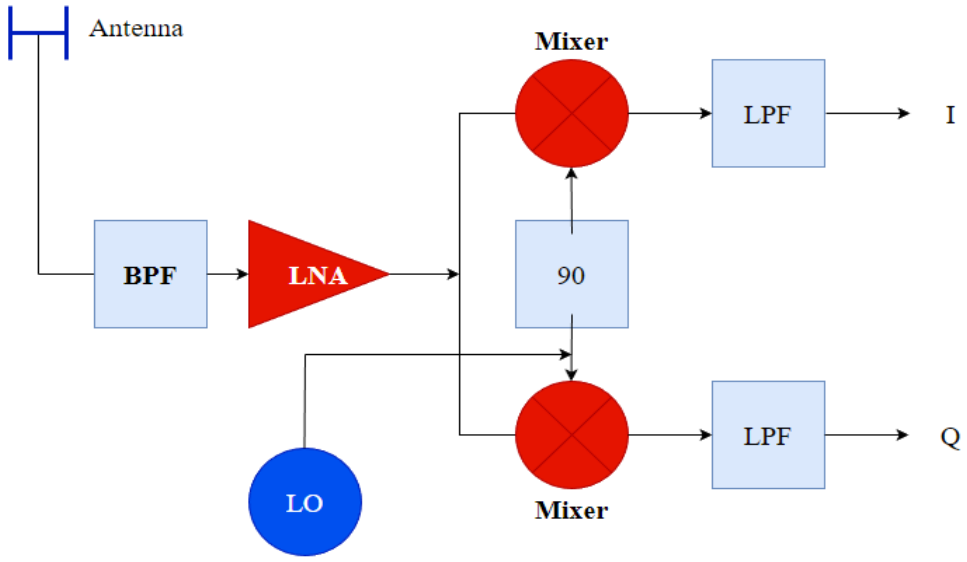

Figure 2.5. *Representation of a direct conversion receiver*

2.2.3. Advantages of homodyne architecture

The homodyne or zero-IF architecture seems to have more advantages than the superheterodyne architecture, because the intermediate frequency is zero. The direct consequence of this is to eliminate the image rejection filter in the receive chain.

Also, in this case, the filtering necessary for channel selection is performed at low frequencies (through the low-pass filter behind the I/Q demodulator). In this way, integrated active filters or digital filters can be used, which are much cheaper than bandpass filters for superheterodyne reception.

2.2.4. Disadvantages of homodyne architecture

2.2.4.1. Coupling between LO and power amplifier

In transmission and reception, the local oscillator frequency (F_{LO}) and the channel carrier frequency (F_{RF}) are the same. In the transmitter, the signal to be transmitted is highly amplified and there is a strong coupling between the power amplifier and the local oscillator as shown in Figure 2.6.

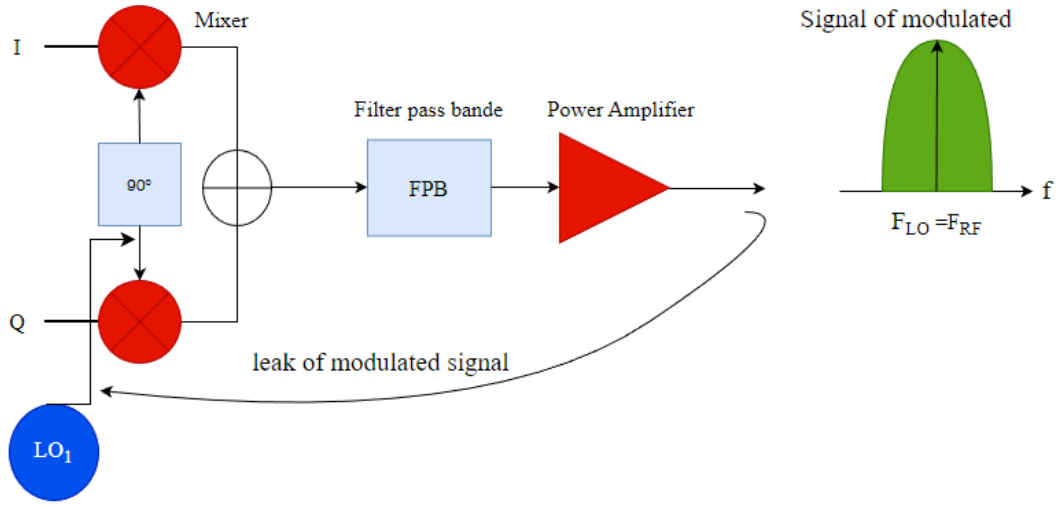

Figure 2.6. *Power Amplifier Leakage to Local Oscillator*

Therefore, the frequency spectrum of the local oscillator is reduced by the high power modulating signal from the power amplifier, and the frequency spectrum of the high power modulating signal is centered on F_{LO}. To overcome this problem, moving the local oscillator frequency away from the transmit frequency (FRF) is necessary.

For this purpose, the frequencies of the two local oscillators (LO1 and LO2) are mixed and filtered so that only the signal at this frequency (F_{LO1} +F_{LO2}) is retained, as illustrated in figure 2.7. Consequently, the frequencies F_{LO1} and $F_{LO2}$are far from the carrier frequency of the channel (F_{RF}=F_{LO1}+F_{LO2}).

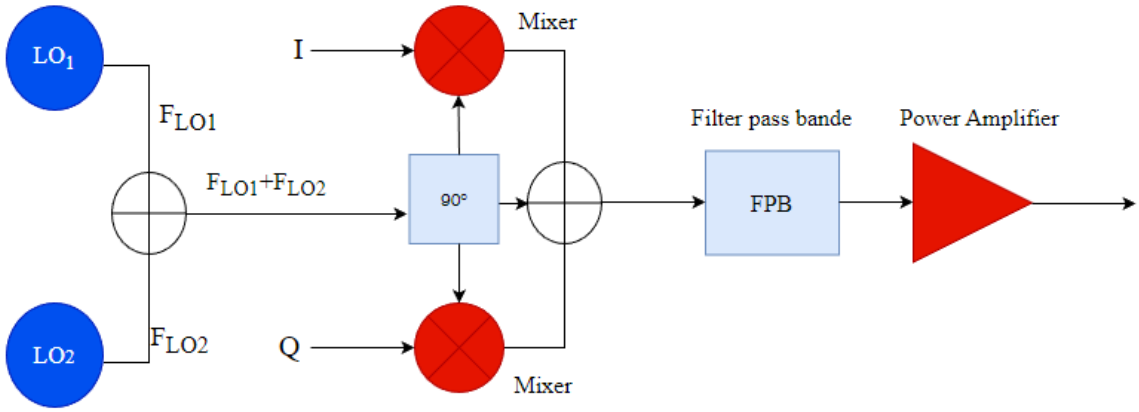

Figure 2.7. *Direct Conversion Transmitter with LO Frequency Shift*

Similarly, the high power interference source (interference) existing on the antenna can also reach the mixer and oscillator input through the LNA, thereby multiplying as shown in Figure 2.8

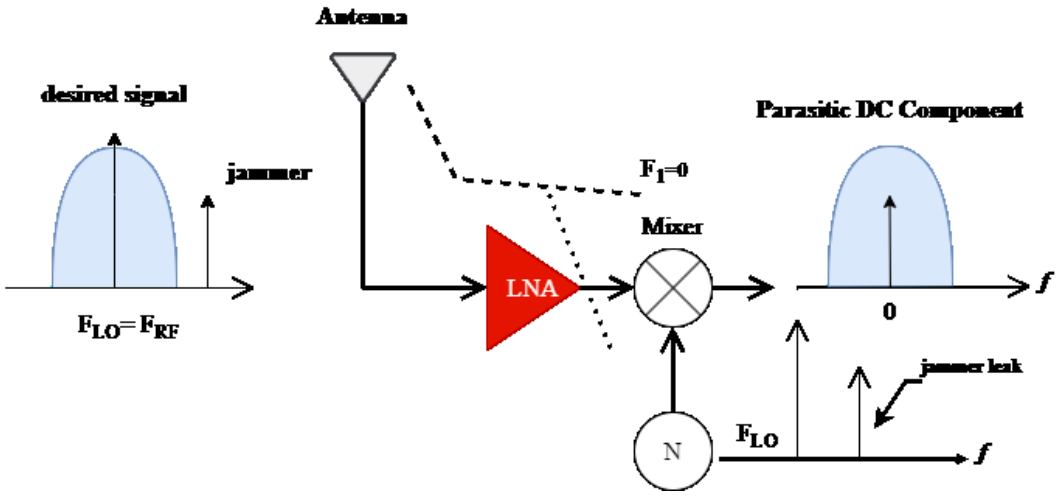

Figure 2.8. *Problem of leaks from jammers to the LO in a chain*

The technology based on high-pass filtering at the output of the I and Q channels can eliminate DC and low-frequency components (such as 1/f noise), which will be presented in the following paragraphs.

2.2.4.2. Noise in 1/f

In the pair of LNA mixers, the gain is close to 30dB and the output signal is around 10 microvolts. The input noise of the next stage (i.e. amplifier and filter) is always critical. In particular, since the frequency conversion is close to the zero frequency, the l/f noise of the component strongly reduces the useful signal, which is a practical problem for using MOS transistors instead of bipolar transistors. To give an order of magnitude, the l/f noise in MOS transistors is ten times that of bipolar transistors [67]. L/f noise makes it difficult to use MOS transistors in RF circuits because the main way to reduce noise is to increase the size of the transistor. However, the capacitance size increases accordingly, and then the RF gain decreases.

2.2.4.3. I/Q Channel imbalance

In reception, the demodulation of the frequency-phase type digital modulation signal requires the use of a secondary I/Q demodulator. Its architecture requires the signal phase shift of the LO oscillator to be 90°, as shown in Figure 2.9, but the error of the nominal 90° phase shift and the imbalance between the amplitudes of the I and Q channels will reduce the constellation. The bit rate of the converted signal directly increases the bit error rate (BER).

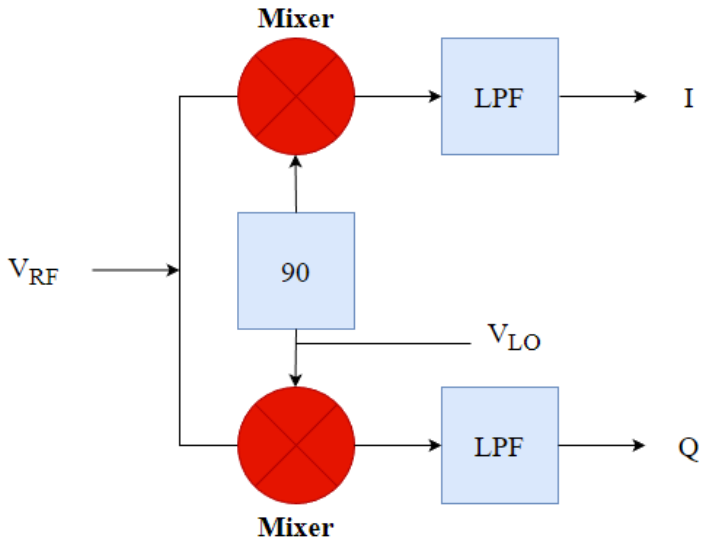

Figure 2.9. *Quadrature I/Q demodulator generated on the LO*

2.2.4.4. Even order distortion

In homodyne reception, the effect of even-order nonlinearity on system performance is very obvious, but this is not the case for superheterodyne receivers. Indeed, if two high power jammers F1 and F2 close to the desired signal arrive at the antenna at the same time, as shown

in Figure 2.10, the output signal contains terms with frequencies F1-F2, due to the second-order non-linearity of the LNA, Naturally, in the case of an ideal mixer, this frequency component is converted to a high frequency, so its effect is no longer troublesome.

Unfortunately, the mixer is leaking between the RF input and the IF output. Therefore, part of the mixer's input signal appears directly on the output without frequency conversion. Thus, low-frequency spurious frequency components will interfere with useful signals, as shown in Figure 2.10.

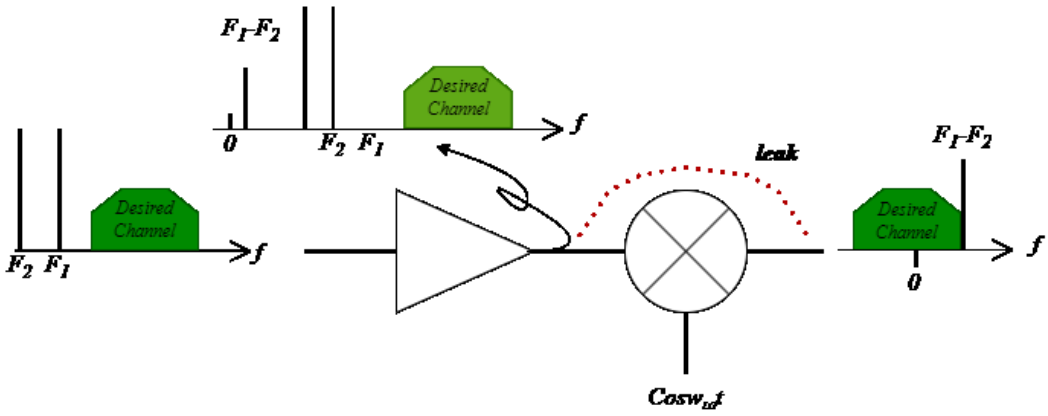

Figure 2.10. *Even order distortion effect*

Using low-noise amplifiers and differential mixers can reduce even-order distortion, although there may be problems converting the received signal to a differential signal.

3. Receiver Performance

Different standardized metrics measure the performances of a receiver. The following subsections present definitions of the performance metrics used to characterize a receiver.

3.1. Noise Figure and Sensitivity

Noise figure. The signal-to-noise ratio deterioration as it travels through a component is measured by the noise factor. A two-port network's noise factor is as follows:

$$F = \frac{SNR_{in}}{SNR_{out}} \qquad (2.1)$$

where $SNR_{in}$and $SNR_{out}$are the signal-to-noise ratios at the input and output respectively. The noise figure (NF) is the noise factor expressed in decibel as givenbelow:

$$NF = 10\log\frac{SNR_{in}}{SNR_{out}} = 10.logF \quad (2.2)$$

The input signal of a typical wireless receiver passes through a series of several parts, including a filter, an LNA, and a mixer. Each of these elements gradually degrades the signal to noise ratio. The noise factor of an n-component cascaded system with distinct noise factors and gains for each component is given by: The signal-to-noise ratio's deterioration as it travels through a component is measured by the noise factor. A two-port network's noise factor is as follows:

$$F = F_1 + \frac{F_2 - 1}{G_1} + \frac{F_3 - 1}{G_1 G_2} + \cdots + \frac{F_n - 1}{G_1 G_2 \ldots\ldots G_{n-1}} \quad (2.3)$$

where the stages are numbered from input to output in subscripts. Sensitivity. The lowest signal level that a receiver can detect is known as its sensitivity. The input source resistance's thermal noise, the noise figure, the signal bandwidth, and the necessary signal-to-noise ratio all play a role for signal identification. Sensitivity is provided by [68]:

$$P_{\min(dBm/\,Hz)} = P_{\mathrm{RS}(dBm/\,Hz)} + NF_{dB} + 10.logB + SNR_{\min(dB)} \quad (2.4)$$

3.2. The conversion gain

The first parameter to consider when designing a mixer is the conversion gain. To define the gain of the mixer, it is necessary to take into account the particularity of its variation

of frequency. In fact, the power transfer efficiency of the RF signal is very important. For this reason, RF circuits are optimized to have power gain rather than the voltage or current gain of low frequency circuits. This parameter represents the effect of the mixer on the power budget of the radio circuit, i.e. the increase or decrease in the power of the useful signal. It represents the ratio between the power of the useful signal leaving the mixer (PR) and the power of the same signal entering the same circuit (PBB). It can be represented in many forms, such as (2.5):

$$G_C = \frac{P_{RF}}{P_{BB}} \quad (2.5)$$

Or it can be expressed in the case of a mixer using field effect transistors by:

$$G_C = \left(\frac{V_{BB}}{V_{RF}}\right)^2 \times \frac{R_L}{R_S} \tag{2.6}$$

It is actually the ratio of the voltages and a power correction factor expressed by RS and RL which represent the input and output resistance of the mixer respectively.

3.3. Linearity

3.3.1. Harmonic Distortion

A sinusoidal signal applied to the input of a nonlinear system produces at the output multiple harmonics of the input frequency along with a DC component and the fundamental signal as shown in Figure 2.11, this phenomenon is called harmonic distortion.

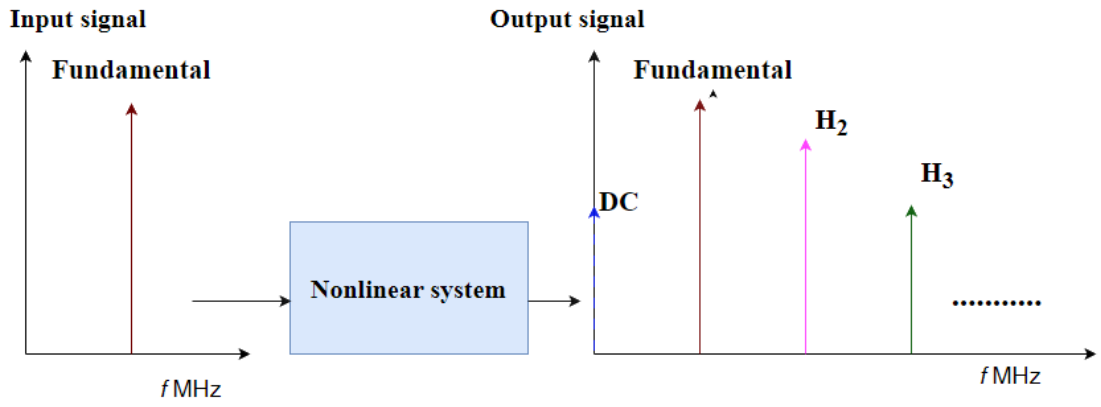

Figure 2.11. *Harmonic Distortion*

For the input signal $(t) = A\cos(\omega t)$, we obtain at the output by polynomial approximation:

$$V_{out}(t) = \alpha_1 A cos(wt) + \alpha_2 A^2 cos^2(wt) + \alpha_3 A^3 cos^3(wt) + \cdots \tag{2.7}$$

$$V_{out}(t) = \alpha_1 A cos(wt) + \alpha_2 A^2[1 + cos(2wt) + \alpha_3 A^3[1 + cos(wt) + \cos(3wt)] \tag{2.8}$$

$$V_{out}(t) = \alpha_1 A^2 + (\alpha A + \alpha 3A^3)cos(wt) + \alpha_2 A^2 cos(2wt) + \alpha_3 A^3 cos(3wt) \tag{2.9}$$

Since the receiver is based on nonlinear principles in the frequency conversion process, it is considered a major source of spurious signals. This behavior can be characterized by two parameters: the 1dB compression point and the third-order intermodulation point. But sometimes second order intermodulation (IP2) products are also taken into account, during design, especially zero IF receive chain.

3.3.2. The 1dB compression point

The 1dB compression point represents the deviation of the conversion gain from 1dB and is plotted against the input power of the mixer, because for high power signals applied to the mixer the output will naturally clip, thus reducing conversion gain. The saturation principle and calculation of the 1dB compression point is illustrated in Figure 2.12, where the dotted line represents the ideal response.

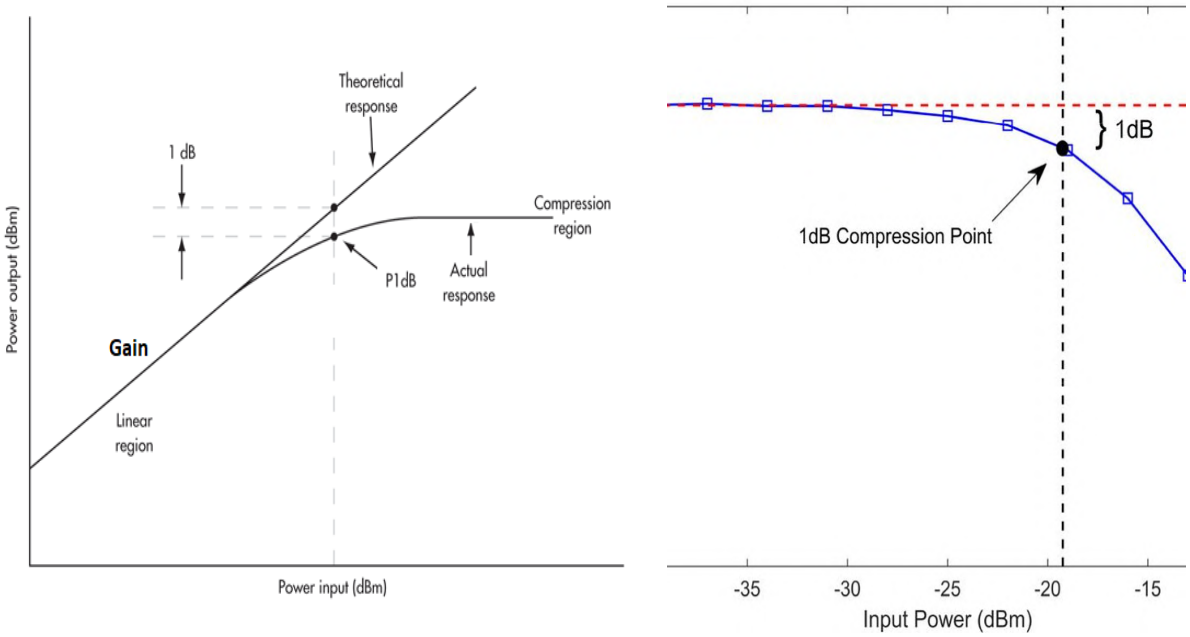

Figure 2.12. *1dB Compression Point*

3.3.3. Third-order intermodulation distortion

The third-order intercept point (IP3) or "third-order intercept point" is a fictitious point, but very interesting to characterize the linearity of a mixer. IP3 corresponds to the point where the amplitudes of the fundamental and the third harmonic are equal. We define IIP3 (input IP3) as the amplitude of the input signal corresponding to IP3 and OIP3 (output IP3) as the amplitude corresponding to the fundamental output and IM3.

3.3.4. Second Order Intercept point (IP2)

A hypothesized location known as the Second Order Intercept location (IP2) is when the power of second order components will equal that of fundamental components.

As a result, when we plot the power input vs power output, IP2 represents the interpolated position where the basic component power curve and the second order intermodulation (IMD2) component curve converge.

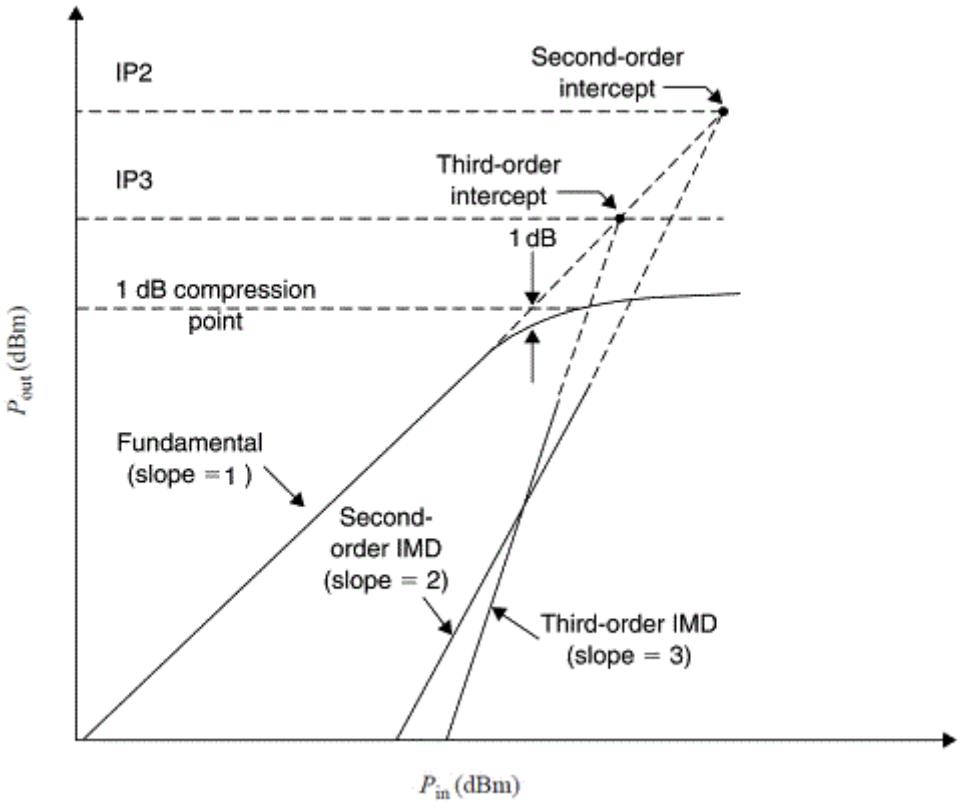

Figure 2.13. *Third-order intermodulation product and Second Order-Intercept point*

Figure 2.13 represents the power of the output signal as a function of the power of the input signal at the fundamental frequencies and the harmonic of order 3. The IP3 is defined by the intersection of the asymptotes of the two curves. Also, ip2 is shown in this figure.

3.3.5. Intermodulation Distortion (IMD)

If a non-linear system uses two or more signals, intermodulation distortion (IMD) will develop. The non-linear device's output spectrum will include the input signals' sum and difference as well as their harmonics in addition to the original signals. As a result, if a non-linear system receives two signals at its input, let's say at frequencies f_1 an f_2d, the non-linearity would result in additional output signals at other frequencies, such as $f_1 + f_2$, $f_2 - f_1$, and $2f_1$, as shown in figure 2.14, which are also known as **2nd** order intermodulation products. The "harmonics" $2f_1$ and $2f_2$, which are merely copies of a signal that appears at integer multiples of the fundamental signal, are the products $2f_1$ and $2f_2$. It is thought that these sideband frequencies are undesirable.

These 2nd intermodulation products will combine with the initial signals to produce 3nd intermodulation products in the following phase. The component signals, including the initial signals (f_1 and f_2) and 2nd order intermodulation products (f_1 + f_2, f_2 - f_1, $2f_1$ and $2f_2$), will be added to and subtracted from one another to produce additional signals. Most of these intermodulation signals are not close to the original signal so can easily be filtered out or do not cause issues. However, due to their proximity to the original signal, the two intermodulation products $2f_1$- f_2 and $2f_2$-f_1 might be problematic and create interference. These products are known to cause intermodulation distortion.

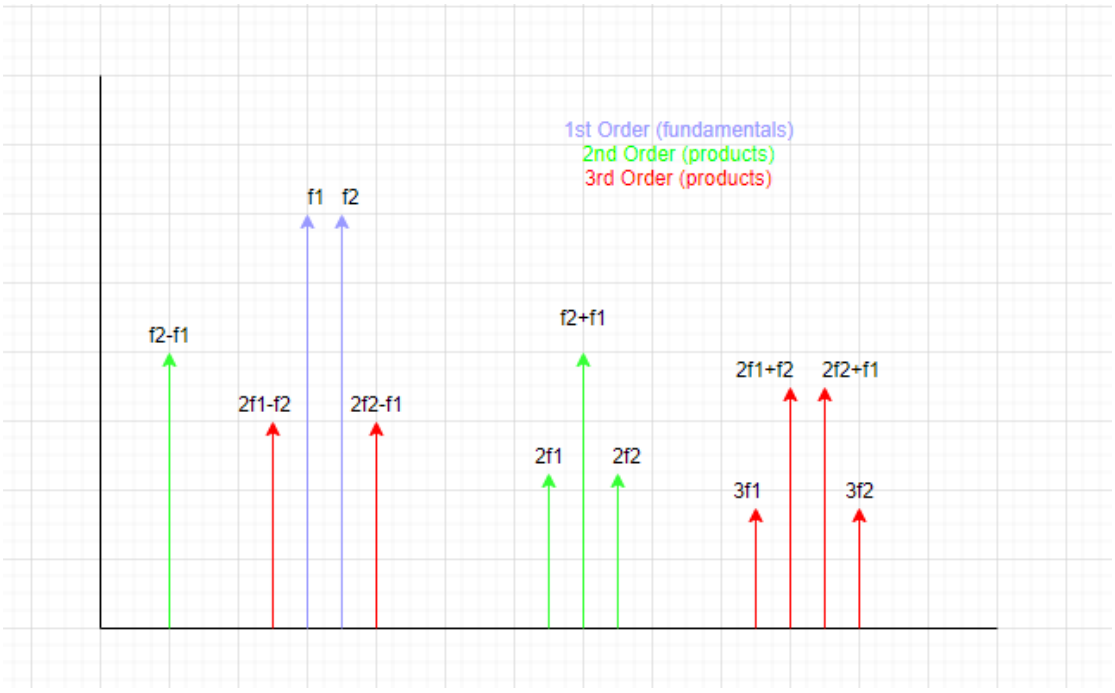

Figure 2.14. *Output spectrum of second and third order IM products*

Filtering is typically used to cope with these problematic IMD products, but when they are extremely near to the intended (fundamental) frequencies, filtering becomes challenging. In contrast to 2nd order distortion products, which seem to be farther away from the originating signals ($f_1$and f_2), these 3rd order intermodulation products are of major concern since they are challenging to filter out. 'Spectral Regrowth' is a term used to describe the increased frequency content produced by the third order distortion. Poor linearity can cause spectrum regrowth in a transmitter, which can disrupt other wireless channels. In a receiver, however, it can result in out-of-band signals causing the desired signal to be distorted. IMD and harmonics cause neighboring channel leakage, noise, or distortion, which lowers the system performance as a whole.

Some Interesting Things to Note:

- The amplitude of harmonics usually decreases as the harmonics order increases. Higher-order harmonics have very low amplitudes and thus can usually be ignored. And most of the higher-frequency products often fall outside of amplifier bandwidth, filter passbands, etc.
- Third-order intermodulation products have an amplitude proportional to the cube of the input signal whereas second-order components have an amplitude proportional to the square of the input signal.
- The best way to avoid IMD products is to operate the device in the linear region before it starts generating distortions.
- The order of harmonics and intermodulation is the sum of their (unsigned) coefficients:
    - $2f_1$ is second-order (2)
    - $f_1 + f_2$ is also second order (1+1)
    - $3f_1$ is third order (3)
    - $2f_2 - f_1$ and $2f_2 + f_1$ are both third-order (2 + 1)

3.4. Bandwidth

The bandwidth characterizes the signal processing limit desired by the circuit. Obviously, mixers cannot handle signals with just any shape or envelope. This parameter determines the operating frequency range of the mixer, defined by a 3 dB drop in the conversion gain.

3.5. Mixer port isolation

Isolation is a measure of circuit balance within a mixer. When the isolation is high, the amount of "leakage" between the hybrid ports will be very low. Typically, the isolation in a mixer decreases with frequency due to unbalanced capacitance between transformers, inductors, or diodes. Typically, a double-balanced mixer operating at the highest operating frequency provides 30dB of isolation.

Achieving better isolation depends on the choice of mixer topology. Next, we specify the isolation terms between the ports as defined in Figure 2.15. This parameter corresponds to the operating frequency range of the mixer and is defined by a 3dB drop in the conversion gain Typically, the LO-RF isolation of the conversion mixer's ability to prevent LO signal leakage

at the port RF is the most critical of the three parameters. Indeed, the amplitude of the LO signal is large and its frequency is close to that of the RF signal. Isolation for BB-LO and BB-RF is generally acceptable due to the low amplitude of the BB signal at the circuit input.

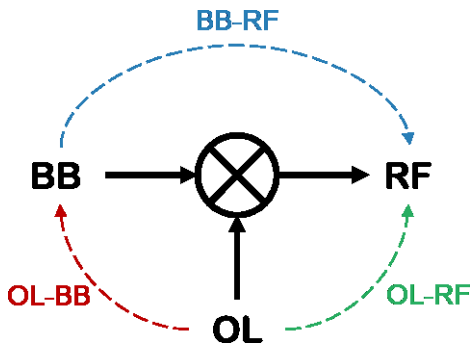

Figure 2.15. *Port isolation in a mixer*

4. Design for direct conversion UWB receiver

4.1. State of art of UWB receiver

In [69] presents a low-complexity IR-UWB receiver front-end circuit, which is implemented in a 0.18-µm CMOS technology, operating under 1.8V. Simulation results show that the receiver can correctly detect the envelope detection, with the smallest input power being 90 dBm. The wideband of the signal is 500MHz and carrier center frequency is 4 GHz. Results show that the performances meet the requirement of low band of UWB spectrum from 3 GHz to 5 GHz.

In [70] An interferer-tolerant receiver for the first set of ultra-wideband frequencies (3.1-4.8 GHz) is presented. It has two modes of operation: detecting and receiving. The signal is routed through a low-noise amplifier (LNA), a multiplier, a phase, and a decision circuit in the detecting mode. It travels via the LNA, three adjustable notch filters, a mixer, and a BB filter when it is being received. Blockers are located by the blocker detector, which then reports their positions to the receiver's notch filters for rejection. The complete system uses between 23.8 and 9.6 mW of power and is built into a conventional TSMC CMOS 65-nm technology. The receiver can reject up to three out-of-band interference sources simultaneously and has a maximum IIP3 and IIP2 of 18.9 and 46 dBm, respectively.

In [71]This study describes a two-stage common source-common gate architecture with source inductive CMOS low-noise amplifier (LNA) with a 0.3V, 5.1GHz frequency. A 0.3 V power supply results in a simulation with a low noise figure of 3.05 dB and low power usage of 0.5 mW. By employing a redesigned structure to lower the supply voltage, which results in decreased power consumption, degeneration is minimized.

The design of a wideband low-noise amplifier is one of the key difficulties in wideband communications systems. The LNA should provide enough gain and have low noise as the first active element in the receiver chain to keep the total receiver noise figure as low as feasible. Wideband on-chip input matching to a 50 antenna/filter, strong linearity, and low power consumption are desirable in the majority of applications. To achieve the design requirements, gain-flatness throughout the whole frequency range of interest is also required. These qualities are the pillars of the wideband LNA design and have an impact on the characteristics of the entire broadband communication system.

4.2. LNA Topologies

Typically, the matching network used to differentiate LNAs. Numerous topologies of various kinds have been suggested in the literature based on the criteria. An overview of these topologies is provided in this section.

4.2.1. Resistive Termination

The most straightforward topology in terms of matching is probably resistive termination [72]. An easy resistor of value RS is employed in parallel with the input transistor gate to accomplish impedance matching with the source impedance. Figure 2.16 illustrates this.

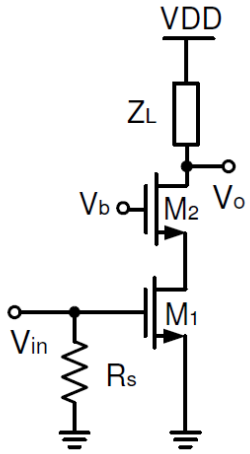

Figure 2.16. *Simple resistive termination*

The topology's obvious benefit is its straightforward broadband matching. Since there are no inductors in this arrangement, it requires a minimal amount of space overall. However, such a structure performs poor in terms of noise. This is mostly caused by the termination resistor RS's noise contribution and the input voltage attenuation at the transistor M1's gate. This topology's noise component is displayed as

$$F \geq 2 + \frac{4\gamma}{\alpha}\frac{1}{R_s} \tag{2.10}$$

The structure can achieve a minimum noise figure level of 6dB. Of course, the attenuated input at the M1 gate improves linearity, but at the expense of reduced gain.

4.2.2. Common Gate Topology

For matching reasons, the 1/gm impedance present in a transistor's source can be utilized in place of an actual resistor, as in the prior scheme. As seen in Fig. 2.17, when the source resistance R S is matched to 1/gm2 of the transistor M2, this is known as a common gate topology [73].

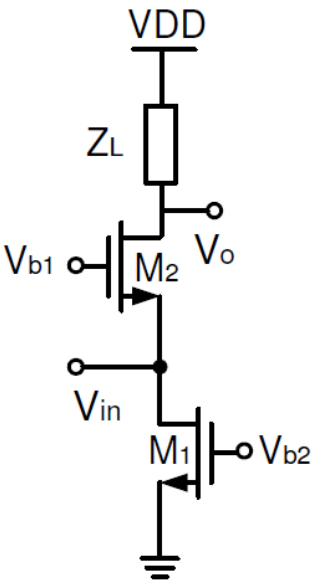

Figure 2.17. *Common gate topology*

When the gate noise current is ignored, the noise factor for this architecture(topology) is roughly given by

$$F \geq 1 + \frac{\gamma}{\alpha} \tag{2.11}$$

From the equation above, it is simple to deduce that the lowest noise level that may be achieved in long channel devices is 2.2 dB and in short channel devices is 4.8 dB. The main disadvantage of employing this structure is the higher power consumption. The transistor M2's gm must be 20mA/V in order to match the input impedance to 50Ω, which increases power consumption. Broadband matching and a smaller region are benefits.

4.2.3. Resistive Feedback Topology

Figure 2.18 illustrates another broadband input matching LNA architecture that utilizes resistive feedback [72]. By dividing the gain of the LNA by the feedback resistor Rf and applying the Miller Theorem, one may get the input impedance. This implies that for broadband 50Ω matching, a higher RF may be employed, which also yields a lower noise figure. As a result, low noise figures may be obtained with increased gain across a wide frequency range. Listed as input impedance is

$$Z_{in} = \frac{R_F}{1 + \left(g_m - \frac{1}{R_F}\right)(R_F \| R_L \| r_o)} \tag{2.12}$$

This topology's approximate noise figure is given by

$$F = 1 + \frac{R_s}{R_F} \tag{2.13}$$

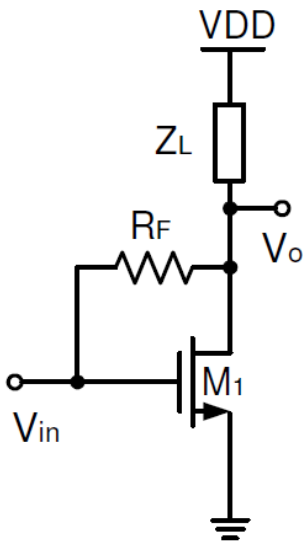

Figure 2.18. *Resistive feedback amplifier*

4.2.4. Topology for Inductive Source Degeneration (ISD)

As seen in Figure 2.19, inductive source degeneration [74] is a useful technique for attaining simultaneous noise and power match. It is possible to write that because of the source degeneration inductor, LS, a real portion in the input impedance (Zin) occurs and the imaginary part is zero at the resonance frequency.

$$Z_{in} = jw(L_g + L_s) + \frac{1}{jwC_{gs}} + \frac{g_m}{C_{gs}}L_s \tag{2.14}$$

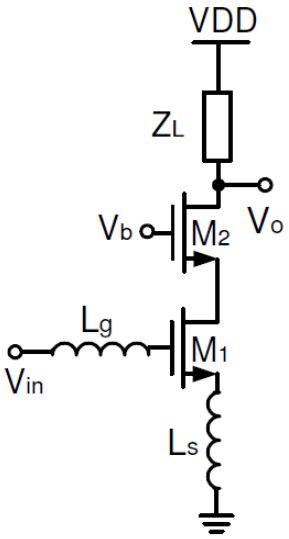

Figure 2.19. *Inductive source degenerated LNA*

Noise figure expression for this topology is given approximately by

$$F \geq 1 + 2.3\left[\frac{w}{w_T}\right] \tag{2.15}$$

As a result, it is clear that very low noise numbers are achievable for this architecture. Since narrow-ban amplifiers may achieve high Q.

4.3. Design and analysis of the Proposed Balun LNA

With the advancement in integrated circuits (IC) technology, biomedical applications with wireless communication have opened new paths to solve medical problems. The small-sized IC with low power consumption and transmission range can be embedded in the body and help in debugging the illness[75][69]. The modern circuits are inductorless to achieve the low cost and size[76]. The ultra-wideband (UWB) technology is suitable for this. The UWB with

a 7500 MHz bandwidth from 3.1 GHz to 10.6 GHz [77][70] is approved by the Federal Communications Commission (FCC) in 2002. UWB has the advantages of low energy consumption and high transmission data rate. These advantages make the UWB a dominating technology [78]. UWB has grown in popularity due to its inexpensive cost, low transmission power, low power dissipation, high data rate, and resilience to multipath fading [79]. Due to hard attenuation of the transmitted signal, the signal at the received antenna is very weak. low noise amplifier (LNA) has to be used to amplify the received signal. The key objective is to develop a very small, low-cost LNA with a high gain and good linearity LNA. Narrowband and wideband LNAs are readily available in the literature[80] [73], but each has own drawbacks. Narrowband LNA makes the use of inductor circuits which make it bulky and energy hungry circuits. Though these have low noise figure but their integrated area is higher and requires technology with RF options to have inductors with high Q. On the other hand, wideband LNAs are complex in design. While RC wideband LNAs have a less complicated design, topologies exhibit high noise figures (NFs)[81]. Recently indcutorless LNAs are also proposed which unveils low NFs and require less on chip area [82][83].

The LNA design in this work is developed with the PMOS transistors as resistors [84]. As will be demonstrated, this strategy introduces a new degree of flexibility that may be exploited to optimize the LNA gain and, therefore, the NF[5].

Our work describes an upgrade to a sort of balun LNA that is entirely transistor-based and devoid of inductors for medical worn communication service. The balun LNA uses common gate and a common source configuration which cancels the noise generated by the common gate. This work uses the transistors in place of resistors to minimize the integrated circuit's area, as well as finding the best values for the dimensions of the transistor to minimize energy consumption, achieve a high gain and good linearity. This reduces the noise figure. The designed system utilizes the UWB frequency range of 3–5 GHz and a voltage supply of 1.8V.

A critical option must be taken while designing a wideband LNA. A single-ended LNA doesn't need a balun to convert the single input to differential as balun reduces the NF substantially and higher losses [11]. It needs only the antenna and RF filters. However, the differential input gives lesser harmonic distortions and improved power supply with noise rejection. The advantages of both single-ended and balun are used to investigate the LNA (see Figure 2.20) to design the simple and low-cost LNA. The load resistors have been eliminated

in this design in favor of PMOS transistors and (M3, M4) that operate in the triode region and are ideally approximated by a resistor between the drain and source.

$$r_{ds} = {}^{1}/_{g_{ds}} \tag{2.16}$$

Where g_{ds} is the channel conductance. To compare the suggested design with the LNA with load resistors, the initial design specifies th V_{dd} ıe resistance value for r_{ds} as in the LNA with load resistors.

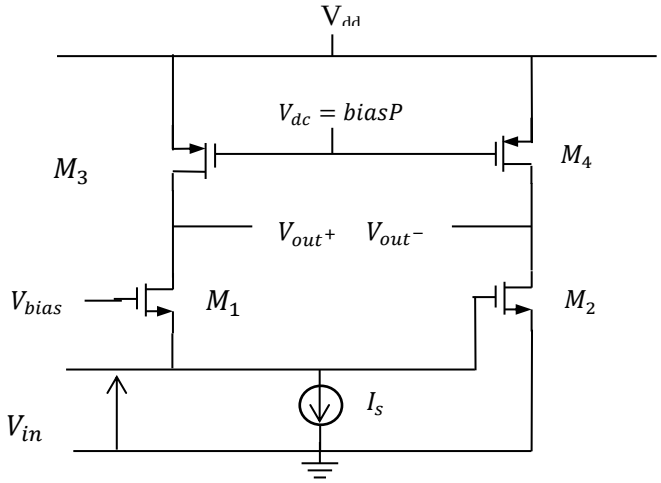

Figure 2.20. *Balun LNA*

The suggested inductorless balun LNA circuit with combined common gate (CG) and common source (CS) configuration is illustrated in Figure 2.20. The single-ended input signal is amplified and transformed into differential output. The CG M1 transconductance g_{m1} governs the input impedance of this circuit. The noise at the input transistor M_1 is canceled when the gain of CS and CG are equal and opposite [85][86]. Additionally, distortion cancellation is possible, enabling the development of very linear LNAs. The impedance matching at the input is achievable if the CG-stage Zincg's input impedance equals to the source resistance R_s. We can modify the current in M_2 by adjusting the DC voltage (Vbias) at the gate of M_1 in order to get an equal voltage gain at Vout+ and Vout-. The DC voltage (biasP) is utilized to alter the magnitude and NF of the LNA by adjusting the output conductance g_{ds3} and g_{ds4} of of M_3 and M_4, respectively.

4.3.1. Small signal analysis

Figures.2.21 and 2.22 represent equivalent small signal circuits of the common-gate stage and common-source stage, respectively. In the following equation g_m and g_{mb} are the transistor's transconductance and body effect transconductance, respectively, $r_o$is the transistor's output

resistance. The capacitance C_{gs}gate-source capacitance. C_{gd} gate-drain capacitance, C_{sb} source-bulk capacitance and C_{db} drain-bulk capacitance. R_s is the signal source resistance. We denote by A_{CG} and A_{CS} the voltage gain of common-gate circuit and common-source circuit, respectively.

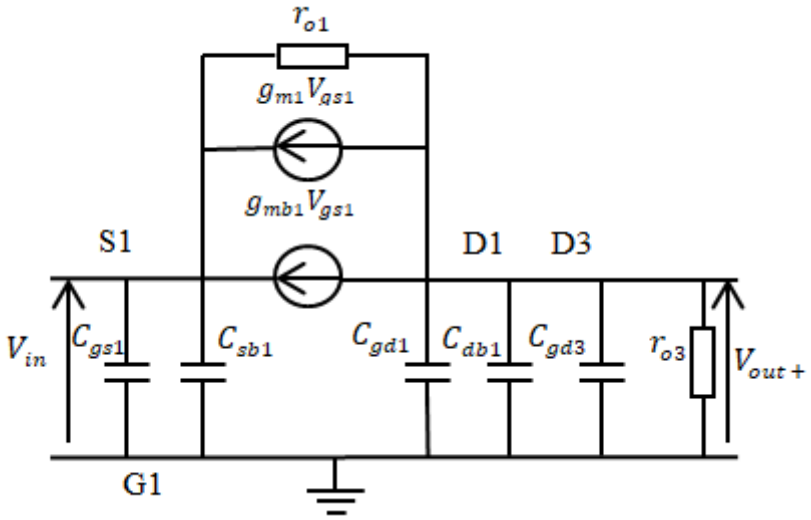

Figure 2.21. *Small signal circuits of the common-gate stage*

4.3.1.1. Small signal equivalent circuit common-gate and common-source stage

In Figure 2.21 we denote by $Z_1 = r_{o3} \parallel \frac{1}{jC_{13}w}$ and $C_{13} = C_{gd1} + C_{db1} + C_{gd3}$. Here $V_{in} = -V_{gs1}$;when summing the currents on the output result in:

$$\frac{V_{out}^{+}-V_{in}}{r_{o1}} - g_{m1}V_{in} + \frac{V_{out}^{+}}{Z_1} = 0 \qquad (2.17)$$

Now solving for $\frac{V_{out}^{+}}{V_{in}}$

$$A_{CG} = \frac{V_{out}^{+}}{V_{in}} = \frac{r_{o3}(1+(g_{m1}+g_{mb1})r_{o1})}{r_{o3}+r_{o1}+jwC_{13}r_{o1}r_{o3}} \qquad (2.18)$$

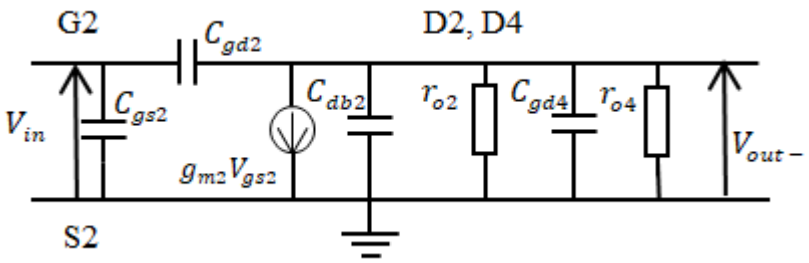

Figure 2.22. *Small signal circuits of the common- source stage*

4.3.1.2. Small signal equivalent circuit common-source stage

For the common-source stage figure 2.22 we denote by $R_o = r_{o2} \parallel r_{o3}$ and $C_{24} = C_{db2} + C_{gd4}$

Here $V_{in} = V_{gs2}$; summing the currents on the output result in:

$$(V_{out}^- - V_{in})jwC_{gd4} + g_{m2}V_{in} + \frac{V_{out}^-}{R_o \| \frac{1}{jw(C_{24})}} = 0 \quad (2.19)$$

Solving for $\frac{V_{out}^-}{V_{in}}$ gives the voltage gain of common-source circuit:

$$A_{CS} = \frac{V_{out}^-}{V_{in}} = -g_{m2}R_o \quad (2.20)$$

Capacitors C_{gs3} and C_{gs4} of transistors M_3 and M_4 don't affect the frequency behavior because both sides are connected to the AC ground. The differential gain of the LNA is given by:

$$G = \frac{(V_{out}^+ - V_{out}^-)}{V_{in}} = A_{CG} - A_{CS} \quad (2.21)$$

If we neglect the effect of parasitic capacitance and g_{mb}, the common-gate voltage gain will be:

$$A_{CG} = \frac{V_{out}^+}{V_{in}} = \frac{r_{o3}(1+g_{m1}r_{o1})}{r_{o3}+r_{o1}} \quad (2.22)$$

and the common-source voltage gain will be:

$$A_{CS} = \frac{V_{out}^-}{V_{in}} = -g_{m2}R_o = -g_{m2}\frac{r_{o2}\,r_{o4}}{r_{o2}+r_{o4}} \quad (2.23)$$

In order to have a differential output circuit and cancels the output noise, the magnitude of the two gains should be equal. This is possible if we make; $r_{o3} = r_{o4} = r_{oPmos}$; $r_{o1} = r_{o2} = r_{oNmos}$; $(g_{m1} + g_{mb1})r_{o1} \gg 1$

and neglecting the transistor body effect. Then $g_{m1} = g_{m2}$, so, it's important to fix the same length dimension L_1=L_2 =0.18μm of the transistors M1 and M2. If we take in account those conditions the LNA gain will be expressed as in (9):

$$A_{LNA} = \frac{(V_{out}^+ - V_{out}^-)}{V_{in}} = A_{CG} - A_{CS} = 2g_{m1}\frac{r_{oNmos}\,r_{oPmos}}{r_{oNmos}+r_{oPmos}} \quad (2.24)$$

Indeed to attain the best performance a suitable scaling of the CS stage is required not only for a lower noise figure but also for lower distortion too. The nonlinearity of the transconductance g_m and the output conductance g_{ds} are the principal cause of this distortion

besides the dependence of g_m on the drain source bias voltage [85]. More a best balun –LNA linearity is obtained if the CS stage has the best linearity.

As the input impedance of the LNA is very significant for the overall receiver performance

$$Z_{inLNA} = Z_{inCG} \tag{2.25}$$

$$I_{inCG} = V_{in} jw(C_{gs1} + C_{sb1}) - \frac{V_{out}^{+} - V_{in}}{r_{o1}} - (g_{m1} + g_{mb1}) * V_{gs1} \tag{2.26}$$

We denote $C_2 = C_{gs1} + C_{sb1}$ and $C_3 = C_{gd1} + C_{db1} + C_{gd3}$

$$-\frac{V_{out}^{+} - V_{in}}{r_{o1}} - (g_{m1} + g_{mb1}) * V_{gs1} = \frac{V_{out}^{+}}{r_{o3}} + V_{out}^{+} * jwC_3 \tag{2.27}$$

$$V_{out}^{+} = \left[\frac{r_{o1}+r_{o3}}{r_{o1}r_{o3}} + jwC_3\right] = \left(g_{m1} + g_{mb1} + \frac{1}{r_{o1}}\right) V_{in} \tag{2.28}$$

$$V_{out}^{+} = \frac{g_{m1}+g_{mb1}+\frac{1}{r_{o1}}}{\frac{r_{o1}+r_{o3}}{r_{o1}r_{o3}}+jwC_3} V_{in} \tag{2.29}$$

$$I_{inCG} = jwC_2V_{in} - \frac{g_{m1}+g_{mb1}+\frac{1}{r_{o1}}}{\frac{r_{o1}+r_{o3}}{r_{o1}r_{o3}}+jwC_3} V_{in} + \frac{1}{r_{o1}} V_{in} + (g_{m1} + g_{mb1}) V_{in} \tag{2.30}$$

$$\frac{I_{inCG}}{V_{in}} = jwC_2 - \frac{g_{m1}+g_{mb1}+\frac{1}{r_{o1}}}{\frac{r_{o1}+r_{o3}}{r_{o1}r_{o3}}+jwC_3} + \frac{1}{r_{o1}} + (g_{m1} + g_{mb1}) \tag{2.31}$$

$$\frac{1}{Z_{inCG}} = jwC_2 - \frac{g_{m1}+g_{mb1}+\frac{1}{r_{o1}}}{\frac{r_{o1}+r_{o3}}{r_{o1}r_{o3}}+jwC_3} + \frac{1}{r_{o1}} + (g_{m1} + g_{mb1}) \tag{2.32}$$

Neglecting the capacitance effects, we obtain

$$\frac{1}{Z_{inCG}} = -\frac{g_{m1}+g_{mb1}+\frac{1}{r_{o1}}}{\frac{r_{o1}+r_{o3}}{r_{o1}r_{o3}}} + \frac{1}{r_{o1}} + (g_{m1} + g_{mb1}) \tag{2.33}$$

$$Z_{inCG} = \frac{r_{o1}+r_{o3}}{r_{o1}(g_{m1}+g_{mb1})+1} \tag{2.34}$$

4.4. Simulation and result

The analysis and simulation of the proposed wideband LNA is evaluated on the gain, noise figure and linearity. The simulation is done with the help of Advanced Design System (ADS) tool and TSMC RF 0.18µm CMOS process.

4.4.1. Gain, S11 and NF

The S_{11} plot in Figure 2.23 shows that the S_{11} is less than -15dB for the frequency range of 3-5GHz, which indicates that the designed LNA has good reflected coefficients in this

frequency band. The range of the gain is equal 25.5-22.47 for the frequencies 3 to 5 GHz which means we have a good performance for the gain, shown in Figure 2.24. The wideband LNA consumes 7.2mW at a Vdd of 1.8V.

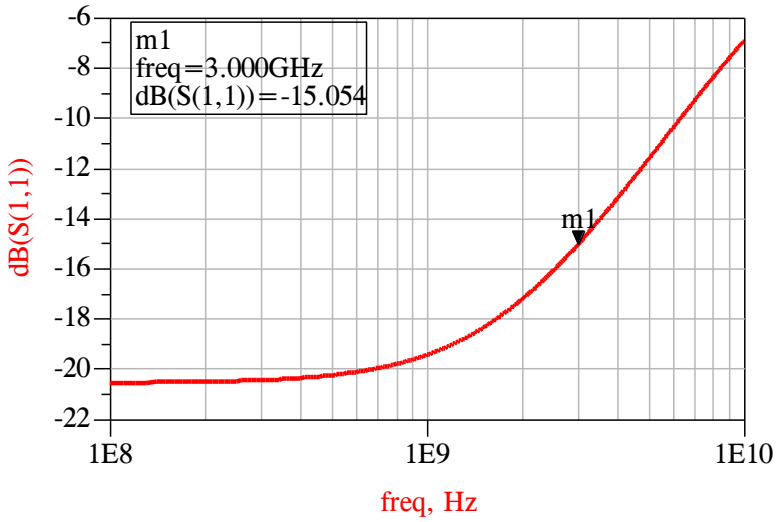

Figure 2.23. *S11 of the LNA*

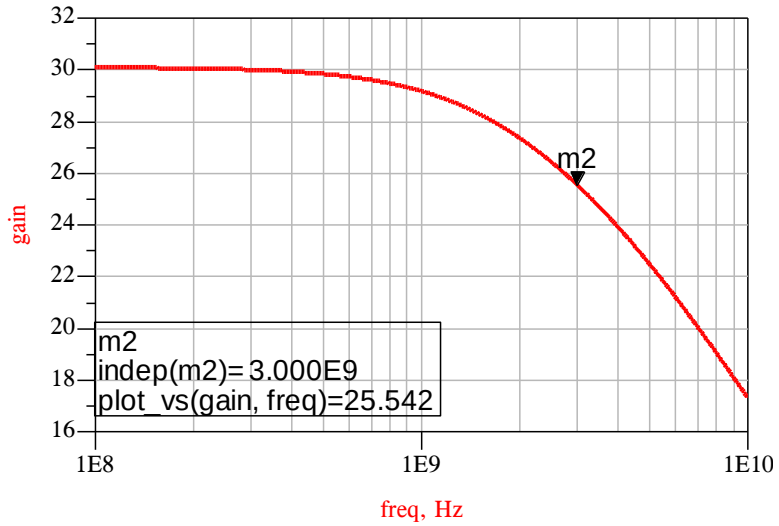

Figure 2.24. *Gain in dB of the LNA*

As shown in Figure 2.25, the Noise figure (NF) vary from (3.2 dB to 3.5 dB) for the frequencies 3 to 5 GHz.

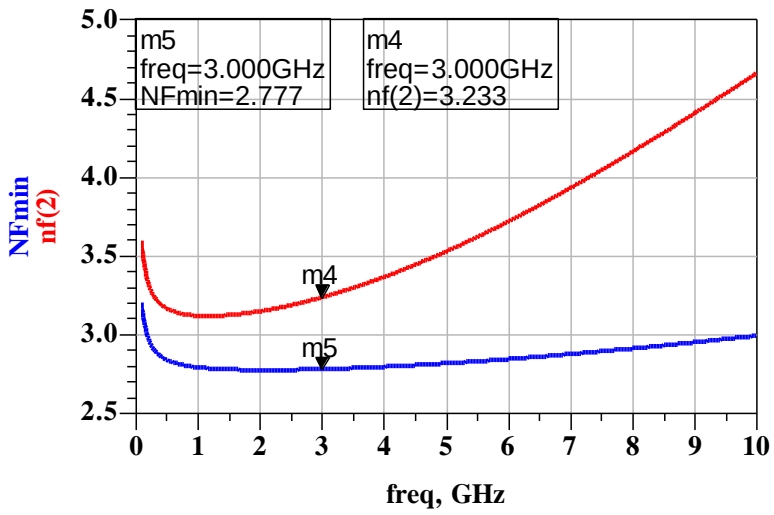

Figure 2.25. *NF of the LNA*

4.4.2. Linearity, IIP3, IIP2 and P-1dB

The distortion performance is analyzed in the simulation for the second and third intermodulation intercept input IIP3 and IIP2, respectively and is depicted in Figure 2.26 and 2.27. An IIP3 of 2 dBm and IIP2 =21.018dBm are achieved and a 1 dB compression point P-1dB(in dBm)=-14 dBm as shown in Figure 2.28. Knowing that the UWB receiver receives a maximum power of -41.3dBm / Mhz, the values found by simulation show that the LNA has an excellent linearity performance.

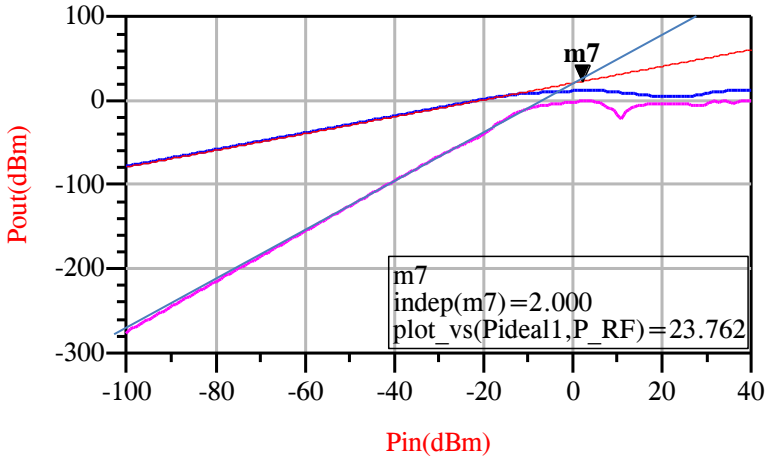

Figure 2.26. *IIP3 of the LNA*

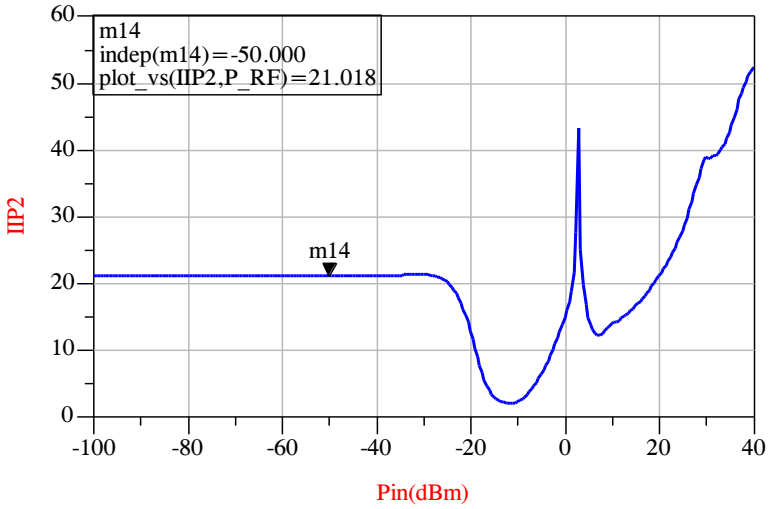

Figure 2.27. *IIP2 of the LNA.*

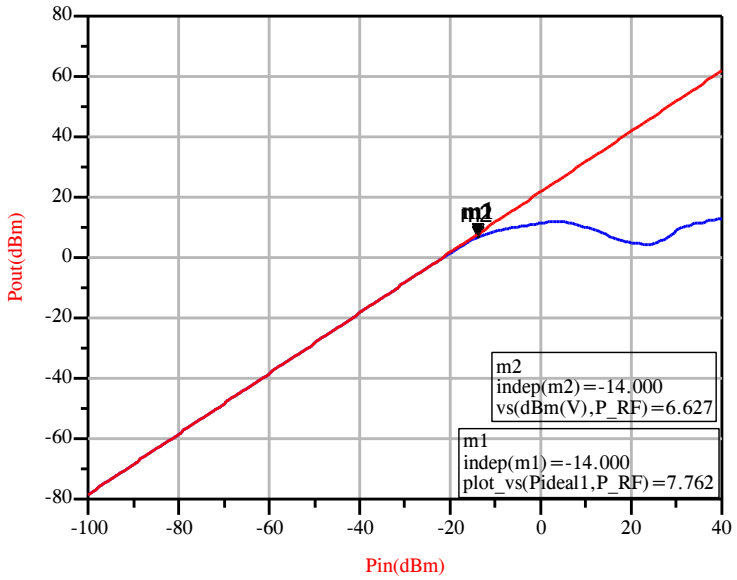

Figure 2.28. *P-1dB(in dBm) of the LNA.*

4.5. Comparison with other work

The results of the proposed circuit are compared with the state-of-the-art works as shown in Table 2.1. The balun usage at the input with a mix of common source and common gate configuration has increased the gain, minimized the NF, reduces the IIP3 and improves the linearity.

Table 2.1 LNA comparsion with other work

	Freq. band (GH)	**Tech. (nm)**	**Gain (dB)**	**NF (dB)**	**IIP2 (dBm)**	**IIP3 (dBm)**	**Power (mW)**	**S11**
[78]	3-5	180	17	8-9	-	-	26.6	<-10
[79]	0.2-10	130	12.2	3.2	6.2	0.7	4.8	<-10
[69]	3-5	180	16.8	2.6-3.1		-3.47	35.1	<10
[87]	0.2-5.2	65	13-15	<3.5	>+20	>0	21	<-10
[88]	0.8-6	90	18-20	<3.5	-	>-3.5	12.5	<-10
This work	3-5	180	25.5-22.4	3.2-3.5	21.02	2	7.2	<-15

5. Conclusion

The basics of receiver designs, sensitivity linearity, etc. are covered in this chapter. Understanding the communication system architecture that is discussed in the following

chapter requires an awareness of these receiver properties. Also, the proposed a wideband LNA structure for high gain and low noise figure with excellent linearity performance is presented. The proposed circuit can amplify the signals of frequencies between 3GHz and 5GHz with a gain ranging from 25.5dB to 22dB respectively, which shows good wideband performance. The design is based on the MOSFET only and uses the balun to convert the single-ended input to differential output with a mix of the common gate and source stages. The analytical solution is also derived for gain and input matching. The validation of the analytical solution is done through simulation in ADS software.

The 180 nm CMOS technology simulation shows that, the NF is 3.2 to 3.5 dB for a power consumption of 7.2 mW. The inductorless Balun-LNA is optimized in order to provide minimal NF, very good linearity, good gain, small chip area and low cost while consuming low power. This obeys to mostly chip constrains. In conclusion, the proposed inductorless Balun-LNA is the best candidate for the UWB transceiver used in the WBAN nodes.

The mixer, which is the second part of the receiver, was investigated and assessed in the next chapter. The many types of mixers were explained, along with the benefits and drawbacks of each type. Then, using the ADS program, the proposed mixer was presented, analyzed, and verified through simulation.

Chapter 3

Design and Analysis of Passive Mixer-based UWB Receiver Front-End

1. Introduction

The development of ultra-low power consumption wireless communication ICs for medical applications is a major challenge [89]. These ICs should meet the following characteristics: small size, low complexity, low noise and low power consumption [90]

The deployment of an ultra-wide band (UWB) communication system in medical applications is highly desirable [91] because of its potential advantages, such as low probability of interception, promotion of the coexistence with existing wireless communication systems, increased data rates [92], decreased power dissipation and enhanced security of medical data, due to the -41.3 dBm/MHz power spectral density emission limit. [93].

Because of the wide frequency range of the UWB signal, it may penetrate biological materials including skin, fat, and other organic tissues, and the reflection from interior organs allows for vital sign monitoring [75].

The UWB wireless body area network (UWB-WBAN) is well-known for providing a reliable, low-power, optimised wireless connection between worn transceivers for physiological signal monitoring [94]. With the improvement of the CMOS technology, the receiver's front end can now be optimised for linearity, noise figure (NF), low power and chip area [95].

Currently, UWB systems are essentially established on two schemes, namely, orthogonal frequency division multiplexing (OFDM) and impulse radio (IR). On the one hand, although OFDM-UWB can provide a reliable broadband solution, it does so at the expense of circuit complexity and energy consumption due to the need for intensive digital signal processing [96]. The IR-UWB system, on the other hand, has been shown to be accommodated at low power consumption and provides simple transceiver topologies that can be readily integrated on a minimal chip area due to its intrinsically cyclical nature [97].

The objective of this chapter is to design an innovative solution for the receiver part of a wireless sensor node device that maximizes the autonomy in a WBAN. A double balanced passive mixer-based receiver operating in the 3-5 GHz UWB for medical applications is

described. The receiver front-end circuit is composed of an inductorless low noise amplifier (LNA) followed by a fully differential voltage-driven double-balanced passive mixer. A duty cycle of 25% was chosen to eliminate overlap between LO signals, thereby improving receiver linearity. The LPF after the mixer, the LNA and the down-conversion passive mixer are designed differentially to reduce the second-order nonlinearity and cancels common-mode noise.

2. Sensor Node

A block schematic of a typical sensor node is shown in Figure 3.1. The sensing unit collects weak physiological data like as oxygen levels in a patient's blood, body pressure, and so on. Signals from the human body are often weak and accompanied by noise, necessitating amplification/filtering operations to boost signal intensity while removing undesirable signals and noise. The processing unit is in charge of communication protocols and signal processing. The data is sent via wireless link from the RF transceiver unit to a portable personal base station or a remote healthcare center for medical specialists to analyze and diagnose. The integration of the sensor node's digital and RF parts on the same chip, utilizing a cost-effective technology like CMOS and WBAN standard, is justified. As a result, many researchers focus on the design of RF transceiver because it is the most power-hungry part.

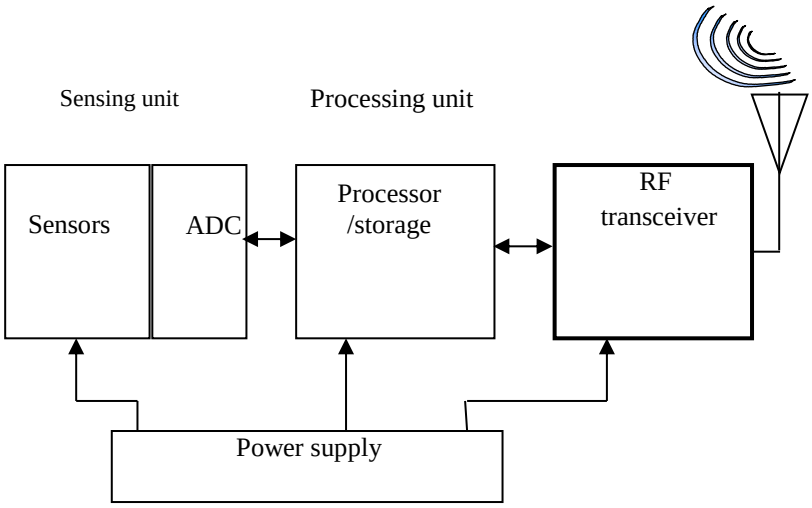

Figure 3.1. *A typical sensor node.*

3. Receiver Architecture

The transceiver architecture is shown in Figure.3.2. Hardware minimisation can be achieved by using a direct conversion architecture that eliminates the image-reject filter and other IF components, enabling a monolithic transceiver[96].

The transmitting chain consists of an UWB pulse generator, a chirp FSK modulator followed by a power amplifier and an antenna. Depending on the transmitter binary information input, the chirp FSK modulator generates a dual-band FSK modulated signal by switching between two sub band signals. The antenna emits the modulated signal once it has been amplified by the power amplifier.

The received signal is first amplified with a LNA. The UWB RF differential LNA signal drives the input of a differential double-balanced down-conversion passive mixer. Four rectangular LO signals with a 25% duty-cycle LO wave set to 4 GHz drive the mixer switches. The differential double-balanced down-conversion passive mixer is connected to the LNA through AC coupling capacitor to isolate the LNA and mixer DC voltages and block the LNA second-order intermodulation products signals. The mixer operates in voltage mode and is loaded with capacitors C_{IF} and a voltage amplifier. Resistors R_B are used to set the mixer bias.

A low pass filter (LPF) is often used to filter the voltage amplifier's output signal .The latter passes only the selected down-converted channel signal and suppresses the other channel. Finally, the chirp FSK demodulator will retrieve the digital transmitted data [92]. Given that the I and Q channels are active at the same time, the 50% duty cycle mixer suffers from IQ crosstalk and its effects on linearity and noise. Then, the Q channel loads the I channel, and vice versa. This phenomenon does not occur in the case of the 25%-duty-cycle mixer, where only one channel is active at any given time.

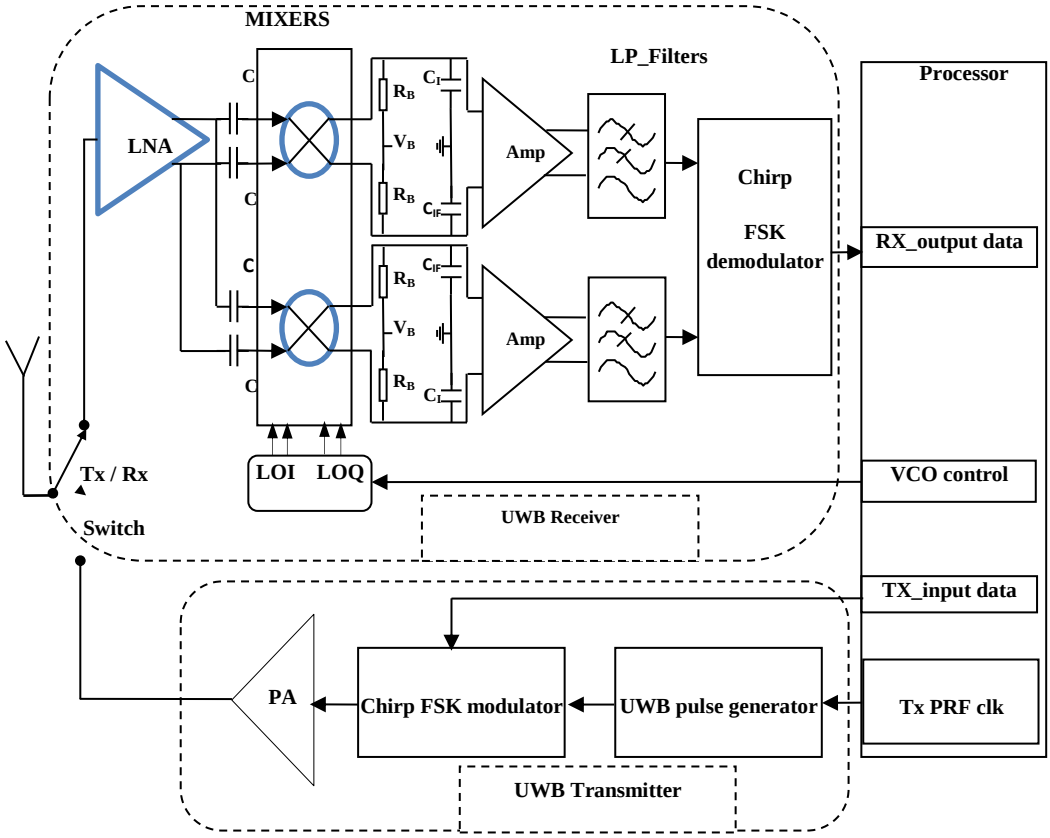

Figure 3.2. *Front-end topology of the UWB transceiver*

The IQ crosstalk in a 25%-duty-cycle mixer is much lower than in a 50%-duty-cycle mixer. The CMOS passive mixer has good linearity and no DC power, except for its clock generation circuit and is less dependent on process variations and has a smaller die area and a better LO-RF feed through performance than an active mixer. Moreover, the LNA, LPF and down-conversion passive mixer is designed differentially to reduce the second-order nonlinearity and cancels common-mode noise.

3.1. LNA CIRCUIT DESIGN

Designing a wideband LNA is one of the major challenges in the design of an UWB communication system [98]. As the first active element in the receive chain, the LNA must achieve sufficient gain while incurring a small additional noise to minimize the overall receiver noise figure (NF). Furthermore, the LNA must provide good linearity while consuming low power [88]. The differential LNA offers several advantages, such as the rejection of the noise travelling in the substrate, the supply noise and attenuates the common mode signal.

Proposals for wideband LNAs with cancelations of noise and distortion have been recently reported in[81]. Thus, a balun is needed at some point in the receiving chain to convert the single-ended RF signal into a differential signal [87]. Broadband passive baluns usually have large losses that greatly degrade the total NF of the receiver. The LNA used in the front end receiver is presented in section (4.3) chapter II. The second device in the receiver it is a down-conversion passive mixer with 25% duty cycle double balanced.

3.2. Mixer circuit design

3.2.1. Mixers Architectures

Any nonlinear component, such as a bipolar transistor, FET, or diode, can be used to create mixers. The design of mixers may be divided into passive and active structures. We want to reduce the conversion loss in the passive architecture since it typically ensures low-noise operation. High gain in microwave FET mixers is very simple to achieve, but this does not guarantee that other performance characteristics will be satisfactory.

Wireless sensor nodes are expected to be battery powered for up to ten years. Unlike passive mixers used in transmitters, there is very little work involving passive mixers used in UWB receivers. The advantages of active mixers are their high conversion gain and good isolation between baseband port and RF. Different circuit techniques have been proposed to increase the conversion gain and improve the linearity of the active mixer over a wide bandwidth, [99].

The receiving chain's mixer is an essential component. Because it must be able to ensure good linearity and a low noise figure, the architecture choice is important [100][101]. The passive mixer is attracting interest, particularly for its intriguing impedance transparency feature and the benefit of its bidirectional nature. This feature makes the passive mixer adjustable and enables out-of-band interference to be filtered without the need of any extra circuitry[102][103]. Also the Passive mixers do not dissipate DC current, they have extremely low power consumption, excellent linearity and good noise figure performance, the receiver based on the passive mixer occupies a very small integration area and better isolation performance between ports (LO-RF and LO-BB) [104].

On the other hand, the passive mixer has the disadvantage of a large conversion loss and a large voltage of the local oscillator (LO) to switch the transistors from an on state to the off state and vice versa. The passive mixer operates in current mode if it is loaded with a very low impedance (the baseband amplifier is a transimpedance amplifier (TIA)). If the passive

mixer is loaded with a high impedance compared to the input impedance, it will function in voltage mode (the baseband amplifier is a voltage amplifier) [102]. In this part, we will study the Mixer fundamentals, type of Mixer, and Metrics of Mixer and introduce performances for down-conversion double balanced passive mixer with a 25% duty cycle.

3.2.2. Mixer Fundamentals

Because linear and time invariant circuits cannot provide outputs with spectrum components that differ from those present in the input, mixers must either be nonlinear or time variant. Mixer action is a time-domain multiplication. To demonstrate this idea, have a look at the mixer model in Figure 3.3

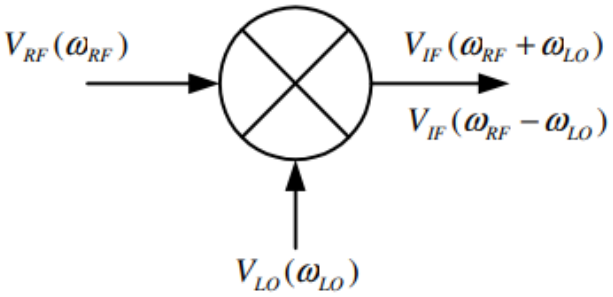

Figure 3.3. *Mixer model*

The output of the mixer is given by

$$V_{IF}(t) = A_{RF}cos(w_{RF})t \times A_{LO}cos(w_{LO})$$

$$= \frac{A_{RF}A_{LO}}{2}cos(w_{RF} - w_{LO})t + cos(w_{RF} + w_{LO})t \quad (3.1)$$

For down-conversion mixers, $cos(w_{RF} + w_{LO})t$ term is filtered out.

3.2.3. Active Mixer

The CMOS Active mixers (frequency multiplier) have a broad bandwidth and can provide conversion gain. The most well-known active mixer design is the current commutating mixer, seen in Figure3.4 This topology was pioneered by Barrie Gilbert [105] in bipolar technology. The majority of FET mixers feature a topology where IF is filtered from the drain and LO and RF are applied to the gate and source, despite the fact that other mixer configurations have been proposed. The main factor affecting frequency conversion is time-varying transconductance.

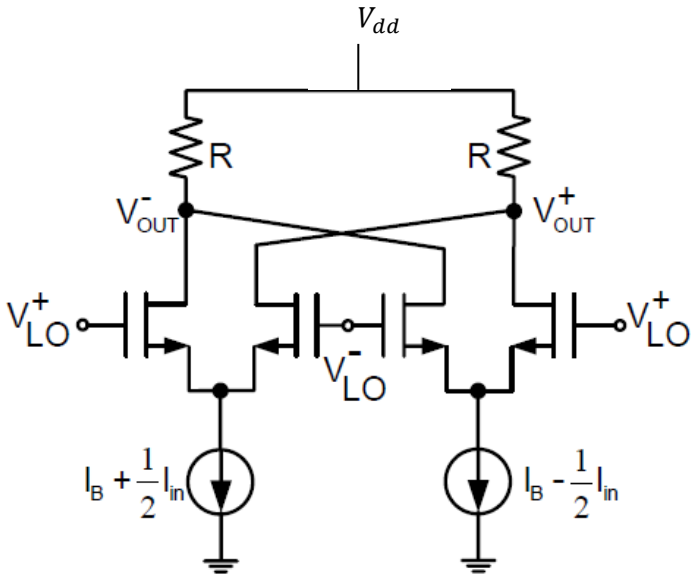

Figure 3.4. *Current commutating active mixer.*

An additional source of loss is added when the average output conductance increases in tandem with the peak drain-to-source conductance. The FET should be biased at the same drain voltage that an amplifier would need. Although it could be marginally sensitive to the dc gate voltage, a well-designed mixer is frequently unaffected by minute fluctuations in the dc drain voltage.

3.2.4. Passive Mixer

The passive mixer's key benefit is that it doesn't waste static power. More significantly, passive mixers have extremely low 1/f noise and very low distortion. The noise figure is dependent on the conversion loss since the high frequency noise is totally thermal. Two examples of the FET passive mixers are displayed in Figure.3.5[106].

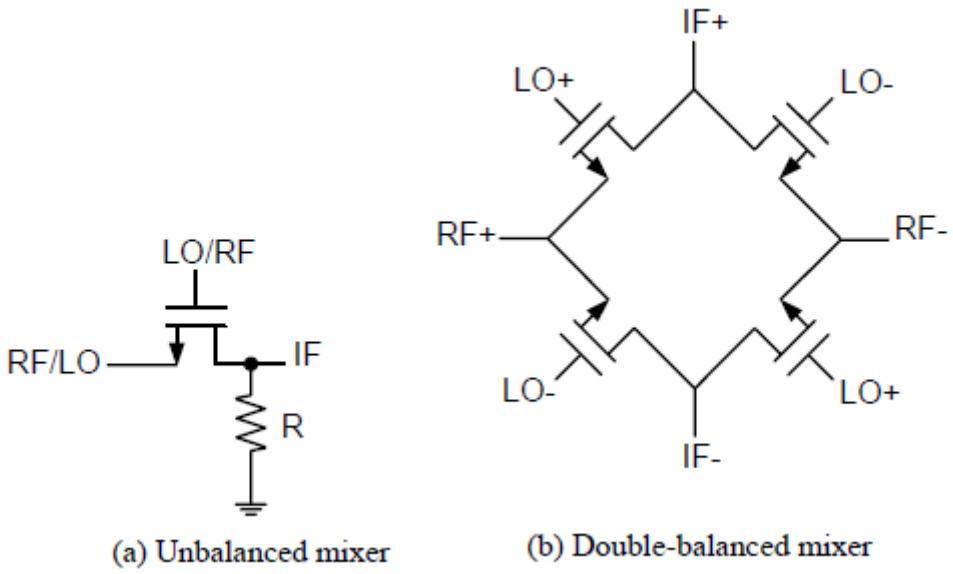

Figure 3.5. *Passive mixer structures.*

Passive mixers often exhibit high linearity since no current flows through the switches. Even if the switch resistance is not linear, the performance of their linearity is superior to that of an active mixer. There are two types of passive mixers: voltage mode passive mixers [107][108], shown in Figure3.6, and current mode passive mixers shown in Figure.3.7.

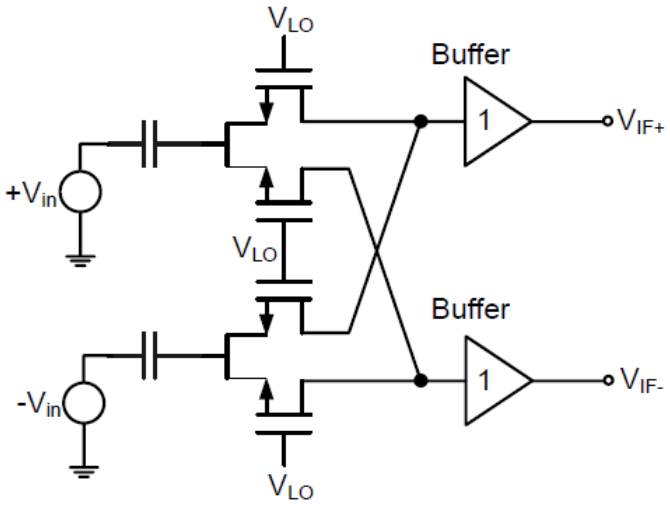

Figure 3.6. *Double balanced voltage-mode passive mixer.*

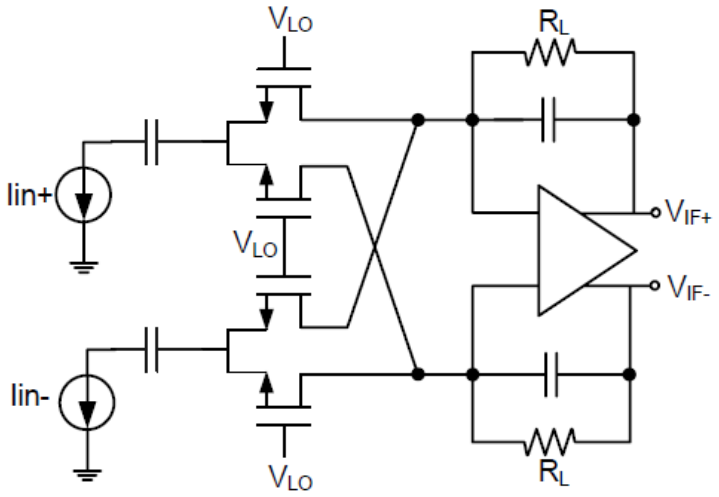

Figure 3.7. *Double balanced current-mode passive mixer.*

In a voltage-mode passive mixer, voltage is commutated using a voltage switch. Compared to the transimpedance stage-loaded current-driven passive mixer, which has a modest signal swing across the switches and further improves linearity. The voltage mode passive mixer has a significant voltage swing across the switches. In a voltage commutating passive mixer, a buffer is required after the switching transistors. All of the MOSFET switches in the current-mode and voltage-mode passive mixer are constantly in the triode region, in contrast to the active mixer. Because of this, its architecture is referred to be passive. The RF transconductor in Figure 3.5 converts the LNA's RF output voltage to a current. Assuming perfect LO square wave switching, the conversion gain of this design is stated as

$$CG = \frac{2}{\pi} g_m R_L \tag{3.2}$$

where *gm* is the transconductance of RF stage in current-driver stage, *RL* is the feedback resistor of the transimpedance amplifier. In actuality, the parasitic components at the common source of the mixer switches and the output of the transconductance stage, which shunts a portion of the RF signal to ground, will result in a reduced real gain. As a result, it's crucial to pay attention to device dimensions, switching stage architecture, and transconductance stage device matching. The IIP3 of the active mixer at high frequency may be made more linear from a linearity standpoint by increasing the DC bias current. [109]. The passive mixer doesn't consume a lot of static power, though. Even though the switches are non-linear, the linearity of the passive mixer is superior than that of the active mixer. In comparison to the voltage-mode passive mixer, the current-mode passive mixer has a lower signal swing across

the switches, which improves its linearity performance. The difference between the loading step in these two designs can be used to identify the cause.

In many frontend receiver systems, low frequency noise from the switches in the mixer design is a serious problem that can degrade the output performance of the entire system. The transimpedance amplifier (TIA) stage is dominant in reducing the flicker noise of the passive current-mode mixer. Any device mismatch in TIA increases the mixer's overall flicker noise. Additionally, the mixer stage's input parasitic capacitance contributes significantly to the noise. Reducing the device width is one way to lower the switches' parasitic capacitance. The device's ON-resistance does, however, rise. As device width shrinks, the ON-resistance value approaches the driving stage's output impedance, which lowers gain and boosts noise contribution. However, in an active mixer, this parasitic capacitance is much lower if the switches stay in the saturation region throughout the entire LO period.

3.2.5. Mixer Metrics

3.2.5.1. Conversion Gain

The proportion of the desired IF output to the RF input is known as conversion gain. This gain can be stated as either power or voltage, for example

$$\text{Voltage Conversion Gain} = \frac{\text{r. m. s voltage of the IF signal}}{\text{r. m. s voltage of the RF signal}} \tag{3.3}$$

$$\text{power Conversion Gain} = \frac{\text{IF power delivered to the load}}{\text{power available from the RF source}} \tag{3.4}$$

3.2.5.2. Noise figure

Input or output referred to as noise voltage or power spectral density can be used to represent the noise of a mixer. A different approach is to employ a noise measure that is proportional to the source impedance's RS noise contribution. One such metric is noise figure, which for a mixer is defined as the difference between the signal-to-noise ratios at the mixer's RF and IF ports. Based on the method of frequency translation, there are two approaches to determine the signal to noise ratio at the mixer's output.

3.2.5.3. Double Side Band (DSB) Noise Figure

Consider the illustration in Figure.3.8. Here, the mixer has a gain of G, and the input signal and noise power are represented by Si and Ni, respectively. As can be seen, if the same signal is present in two frequency bands with the center frequencies of RF1 and RF2, both the signal

and the noise in these bands are downconverted to the IF. The mixer's output results in a signal power of 2GSi and a noise power of 2GNi+No, where No represents the mixer's noise contribution [74].

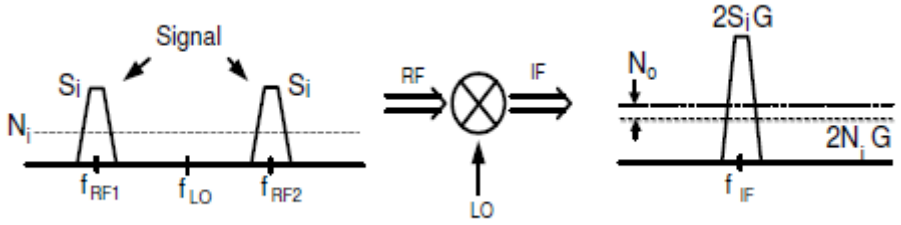

Figure 3.8. *Double side band frequency translation*

Resulting noise figure is known as double side band (DSB) noise figure which can be expressed as

$$F_{DSB} = \frac{S_i/N_i}{GS_i/(2GN_i + N_o)} = 2 + \frac{N_o}{2GN_i} \tag{3.5}$$

3.2.5.4. Single Side Band (SSB) Noise Figure

Now take a look at Figure 3.9's frequency translation [74].The absence of a signal sideband at RF2 is the sole thing that sets this scenario apart from the prior one. However, RF2 white noise may be down-converted to IF. The resultant noise figure may be represented as using the same notation as for the DSB example.

$$F_{SSB} = \frac{S_i/N_i}{GS_i/(2GN_i + N_o)} = 2 + \frac{N_o}{2GN_i} = 2F_{DSB} \tag{3.6}$$

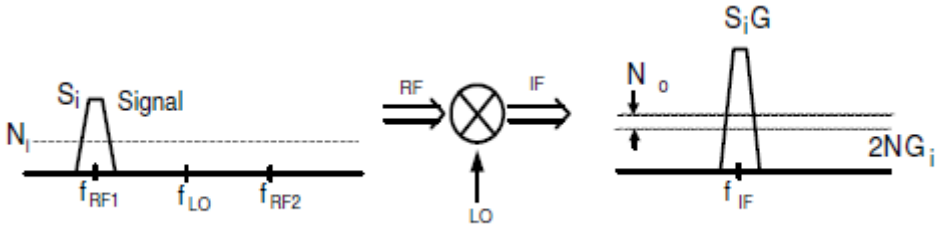

Figure 3.9. *Single side band frequency translation*

F_{SSB} is therefore 3 dB louder than F_{DSB}. The introduction of an image reject filter, however, changes this since it lowers the noise component at the image band. F_{DSB}, however, is higher than F_{SSB}.

3.2.5.5. Port-to-Port Isolation

Port-to-port isolation is a metric for leakage of signal from one port of the mixer to another. It is defined as the ratio of the signal power available into one port of the mixer to the measured power level of that signal at the one of the other mixer ports. Assuming each port has a 50 Ω impedance. Each port has a variable level of leaking criticality. The LO to RF leakage, which is seen in Figure 3.10, is one of the significant leakages. Because LO signals are often significantly stronger, they can readily leak to the RF port through the substrate and parasitic capacitances of the mixer or the LNA. After leaking from the LNA, LO can potentially leak back to the antenna and become broadcast. A DC offset might emerge from this LO leakage when it combines with LO signal inside the mixer and is downconverted to DC. The baseband, especially the VGA, might get saturated by this dc offset. The worst case is when this DC offset changes over time.

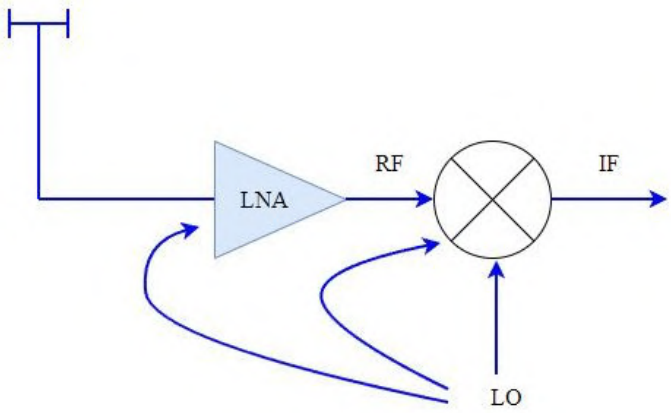

Figure 3.10. *LO to RF leakage*

The port leakage from LO to IF is another significant one. As previously stated, LO power is significantly higher than IF and RF power levels. High amplitude LO signal can quickly saturate the baseband if LO-IF isolation is weak. Due to the low-frequency even-order intermodulation product, RF to LO leakage will allow the interferers and spurs present in the RF signal to interact with the LO, which may lead to problems for the direct conversion design.

4. Proposed Passive Mixer-Based UWB Receiver

4.1. Passive mixer-based UWB receiver circuit

Compared to an active mixer, the main advantages of a passive mixer include low power consumption, low 1/f noise and good linearity. The LO feed-through in the single-balanced

passive mixer is generated by DC current in the RF input[110]. As a result, we selected a double-balanced passive mixer with a fully differential architecture to avoid LO feed-through.

The passive mixer-based UWB receiver circuit is depicted in Figure3.11. First, the LNA amplifies the UWB RF signal coming from antenna. Then the differential RF signal V_{LNAout} is down-converted by the double-balanced passive mixer and appears through the baseband load (C_{IF} || R_B). To prevent the DC bias and the second-order intermodulation components produced inside the LNA, capacitors (C) are added in each mixer input[100].

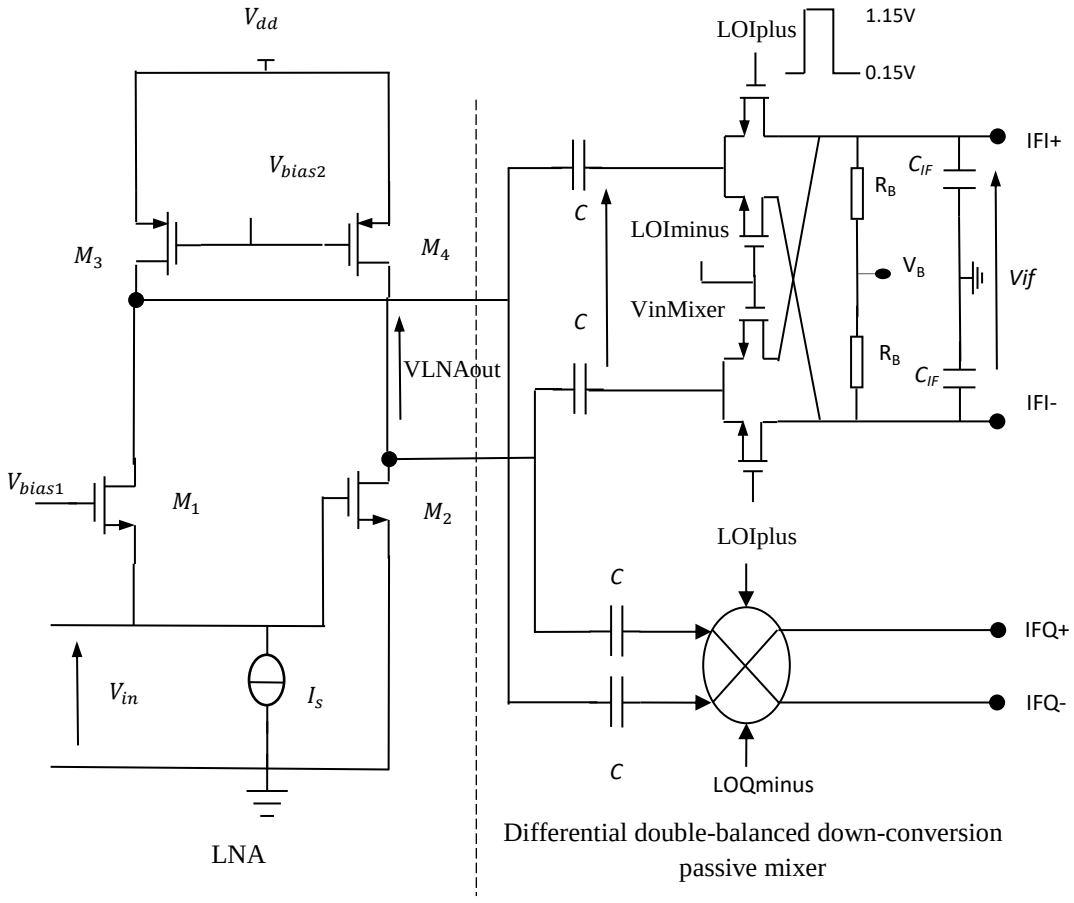

Figure 3.11. *Passive mixer-based UWB receiver circuit.*

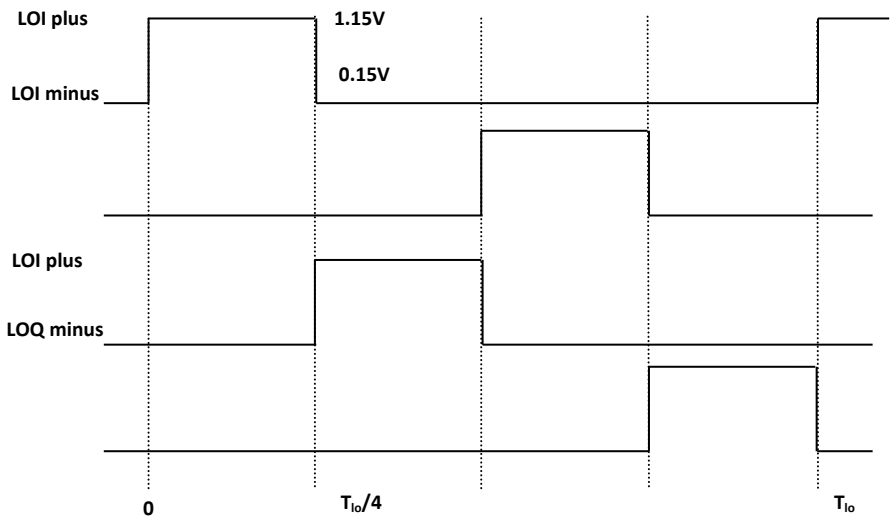

Figure 3.12. *Time representation of LO rectangular signals with a 25% duty cycle.*

As illustrated in Figure 3.12, four rectangular LO signals are employed to operate the NMOS switches, each with a duty cycle of 25%. Because there are no overlap periods between the LO phases, the 25% duty cycle is unaffected by LO rise and fall times, resulting in enhanced NF and linearity. Unlike the 50% duty cycle mixer, this can interfere at any moment. To reduce the mixer sensitivity to process, voltage and temperature (PVT) changes, complete NMOS switching must be ensured. Therefore, the voltage of the LO signal must satisfy the following inequality: $\mathrm{LOvoltage} > V_B + V_{\mathrm{inmixer}} + V_{GS}$, where Vinmixer is the voltage variation of the RF signal at the mixer input and VGS is the voltage necessary for the conduction of the transistors. In this design, we set V_B to 0.3V and the rectangular LO signals to have a maximum LO voltage of 1.15V.

4.2. Time Dependent Analysis of Double Balanced Passive Mixer in Voltage Mode at 25% Duty Cycle

The doubly balanced quadrature passive mixer in voltage mode is shown in Figure 3.13(a). With a simple balanced passive mixer the RF component passing through the mixer can be eliminated at the output but the LO component cannot be eliminated if there is a DC component at the input of the mixer. This is why we used two simple balanced mixers connected so that the LO component is canceled but their useful output signals are not (Figure 3.13(a))

The I suffix indicates the in-phase LO signal, and the Q suffix indicates the quadrature LO signal. Fully differential RF signals (LNAout+ and LNAout-) are converted through the mixer

switches and appear through the baseband load (C_{IF}//R_{IF}). The link capacitors (C_{rf}) block the second order intermodulations generated in the LNA and isolate the biases (DC bias) of the LNA and the mixer. The mixer loads the LNA directly without using a common-gate transconductance as an intermediate stage which usually is placed before the mixer to guarantee an impedance match at 50 Ω. The elimination of transconductances greatly improves the linearity of the front-end. Therefore, mixer input and output impedances interact and influence mixer performance[102].

The switches are controlled by four rectangular LO signals, each having a duty cycle of D = 25%, as shown in Figure 3.13(b). The switches of channel I are clocked by the clocks LOI+ and LOI-, the shift is Tlo/2 between the two. Channel Q switches are clocked by LOQ+ and LOQ- clocks, as for channel I, except are shifted by Tlo/4. The mixer whose duty cycle is 50% suffers from the interactions between the I and Q channels (IQ crosstalk) and their impact on the linearity and the noise figure because both the I and Q channels are in the ON state simultaneously[103]. Then channel I is loaded by channel Q, and vice versa. On the other hand, this is not the case with the mixer, whose duty cycle is 25%, in which, at the same time, only one channel is in the active state.

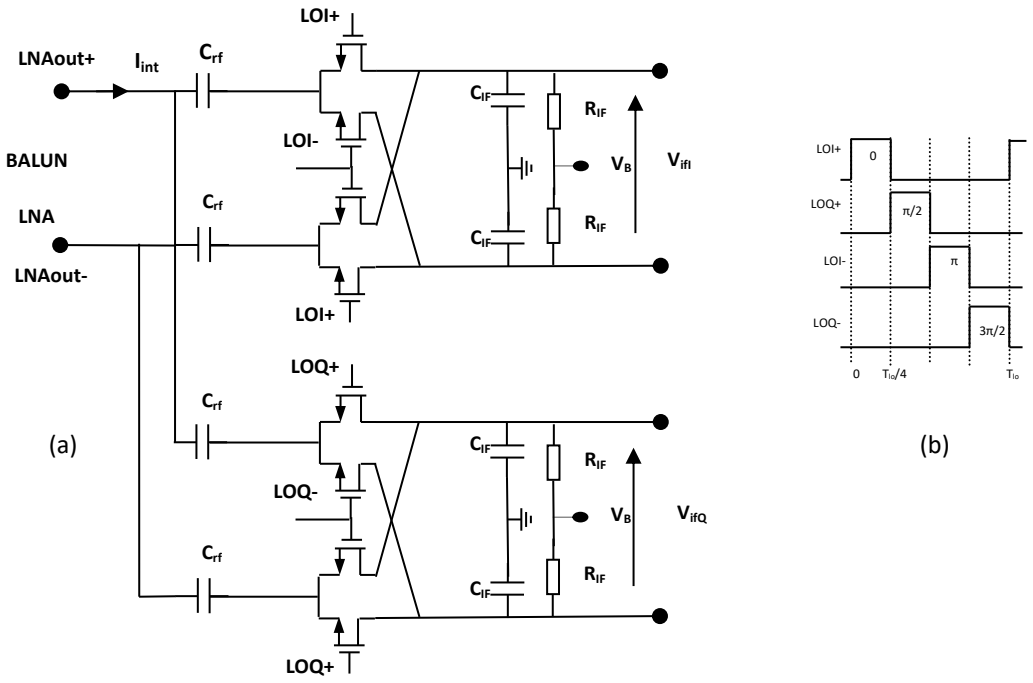

Figure 3.13. *a)Double-balanced passive mixer in voltage mode, (b) rectangular LO signals, D=25%.*

Compared to the 50% duty cycle mixer, the crosstalk IQs of the 25% duty cycle mixer decrease significantly and the voltage conversion gain is larger by 3 dB [103].

Since this circuit is time-varying, we begin by describing its fundamental operations in the time domain in order to assess the mixer's performance. To make the study of it simpler, we first approximate the analogous LTI circuit. Then, while taking into consideration the limitations of our application, we look for the principal parameters of the passive mixer's optimal values. The simulations will be run at 37°, which is the average body temperature.

4.3. Baseband voltages

Figure 3.14(a) shows the schematic of channel I of the mixer, and Figure 3.14(b) shows half of the proposed circuit used to analyze the passive mixer in voltage mode.

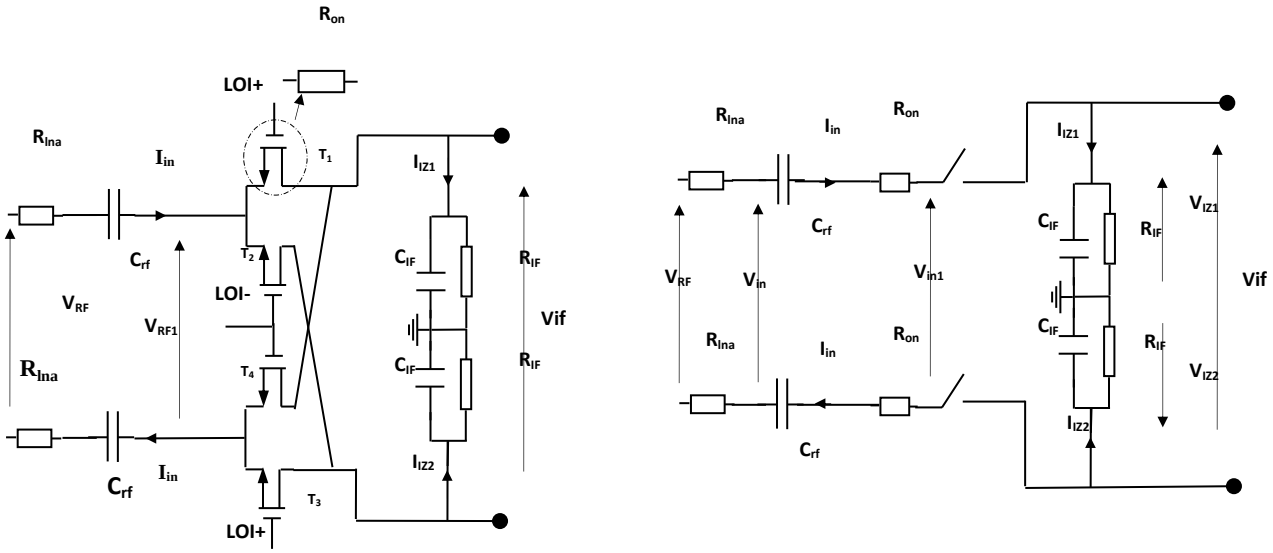

Figure 3.14. *(a) Channel I of the doubly balanced passive mixer. (b) half of the proposed circuit was used to analyze the mixer.*

The differential input voltage from the LNA is given by:

$$V_{RF}(t) = 2Vcos(w_{RF}t + \varphi) \qquad (3.7)$$

Where w_{RF}= w_{IF} + w_{LO}, 2V is the amplitude and φ is the initial phase. The mixer will be used in the zero IF receiver, which means $w_{IF} \ll w_{LO}$. R_{IF} and C_{IF} are chosen so that $\frac{1}{R_{IF}C_{IF}} \ll w_{LO}$. It is assumed that the transistors operate as ideal switches, except that they do not have an ON

resistance of zero but equal to Ron. The four LO signals are named ($VI_{LO+}(t)$, $VI_{LO-}(t)$,) for channel I and ($VQ_{LO+}(t)$, $VQ_{LO-}(t)$) for channel Q. They can be written as follows:

$$VI_{LO+}(t) = \begin{cases} 1 \; if \; k\,T_{LO} \le t \le \left(K + \frac{1}{4}\right) T_{LO} \\ 0 \; if \; \left(K + \frac{1}{4}\right) T_{LO} < t < (k+1)\,T_{LO} \; Where \; k \in Z \end{cases} \quad (3.8)$$

$$\mathrm{VI_{LO-}(t) = VI_{LO+}(\,t - T_{LO}/2)} \quad (3.9)$$

$$VQ_{LO+}(t) = VI_{LO+}(t - T_{LO}/4) \quad (3.10)$$

$$VQ_{LO-}(t) = VI_{LO+}(t - 3T_{LO}/4) \quad (3.11)$$

Two On phases and two Off phases are present for a single LO cycle, as seen in the example in Figure 3.13. During the On phase, $V_{IZ1}(t)$ is written as follows:

$$V_{IZ1}(t) = V_M \cos(\omega_{LO} t + \varphi) \text{ where } V_M < V \quad (3.12)$$

So the channel I voltages across C_{IF} are:

$V_{IZ1}(t) = V_M \cos(\omega_{LO} t + \varphi)$ when $VI_{LO+}(t)$=1 and $V_{IZ1}(t) = -V_M \cos(\omega_{LO} t + \varphi)$ when $VI_{LO-}(t)$=1.

The Q Channel voltages across C_{IF} are:

$V_{QZ1}(t) = -V_M \sin(\omega_{LO} t + \varphi)$ when $VQ_{LO+}(t)$=1 and $V_{QZ1}(t) = V_M \sin(\omega_{LO} t + \varphi)$ when $VQ_{LO-}(t)$=1.

When transistors T_1 and T_3 are in the On phase (see Figure 3.12(a)), each baseband capacitance charges, and the current is expressed as:

$$I_{in} = \frac{\frac{V_{RF}}{2} - V_{IZ1}}{Z_{RF}} \quad (3.13)$$

$$where \;\; Z_{RF} = R_{LNA} + R_{on} + \frac{1}{jC_{rf} w_{RF}}$$

When $VI_{LO+}(t)$=1, the amount of charge in C_{IF} during $\frac{T_{LO}}{4}$ is Qc given by (8):

$$Q_C = \int_0^{\frac{T_{LO}}{4}} I_{in} dt = \int_0^{\frac{T_{LO}}{4}} \frac{\frac{V_{RF}}{2} - V_{IZ1}}{Z_{RF}} dt = \frac{(V - V_M) T_{LO}}{\pi\sqrt{2} Z_{RF}} COS\varphi \quad (3.14)$$

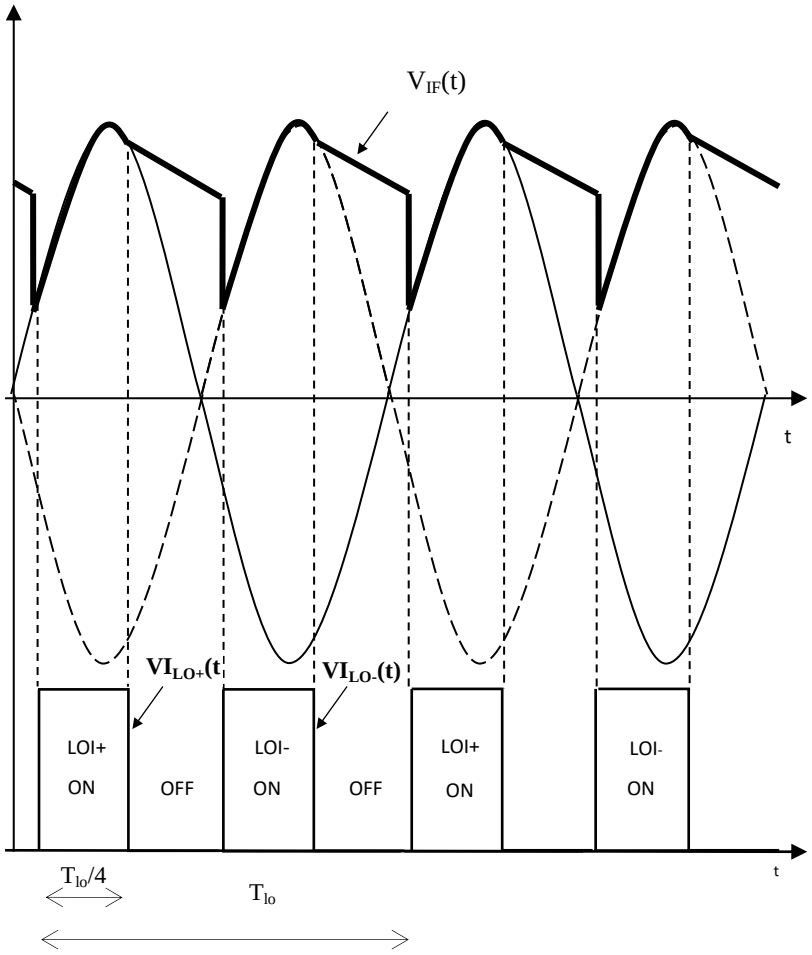

Figure 3.15. *exemple of base band voltage $V_{IF}(t)$, $V_{ILO+}(t)$ and $V_{LO-}(t)$ of channel I.*

When the two transistors T_1 and T_3 are in the Off phase, the capacitors C_{IF} are discharged through R_{IF} during $T_{LO}/4$, this happens between two charging phases. Figure 3.15 shows that the baseband does not hold the voltage constant.

If $\tau = R_{IF}C_{IF}$ is the capacitor discharge time constant then the voltage at the C_{IF} terminals is:

$$V_{IZ1}(t) = V_M.\exp\left(-t/\tau\right) \approx V_M.\left(1 - t/\tau\right) \qquad \frac{T_{LO}}{4} << \tau \tag{3.15}$$

The discharge of C_{IF}through R_{IF} corresponds to the charge Q_d in RIF is expressed in (3.16):

$$Q_d = \int_0^{\frac{T_{LO}}{4}} \frac{V_M}{R_{IF}}\left(1 - \frac{t}{\tau}\right)dt = \frac{V_M}{R_{IF}}\frac{T_{LO}}{4}\left(1 - \frac{T_{LO}}{8\tau}\right) \tag{3.16}$$

We can use the load balance in (3.17) and find the expression for V_M.

$$Q_c = Q_d \Rightarrow V_M = \frac{R_{IF}}{R_{IF}cos\varphi + \frac{\sqrt{2}\pi}{4}\left(1 - \frac{T_{LO}}{8\tau}\right)Z_{RF}} V\ cos\varphi \quad (3.17)$$

A good estimate of the V_{IZ1} value over a T_{LO} period is its average value. The average value of $V_{IZ1}(t)$ over the period T_{LO} is given by (3.18):

$$V_{IZ1av} = \frac{2}{T_{LO}}\left[\int_0^{\frac{T_{LO}}{4}} V_M\left(1 - \frac{t}{\tau}\right)dt - \int_{\frac{T_{LO}}{4}}^{\frac{T_{LO}}{2}} V_M \cos(w_{LO}t)\right] = \frac{V_M}{2}\left(1 - \frac{T_{LO}}{8\tau}\right) + \frac{V_M}{\pi} \quad (3.18)$$

By replacing V_M in the expression (3.17) we obtain the expression (3.19):

$$V_{IZ1av} = \left[\frac{1}{2}\left(1 - \frac{T_{LO}}{8\tau}\right) + \frac{1}{\pi}\right]\frac{R_{IF}}{R_{IF}cos\varphi + \frac{\sqrt{2}\pi}{4}\left(1 - \frac{T_{LO}}{8\tau}\right)Z_{RF}}\ V\ cos\varphi \quad (3.19)$$

With the same analysis steps we find the mean of $V_{QZ1}(t)$ given by (3.20):

$$V_{QZ1av} = \left[\frac{1}{2}\left(1 - \frac{T_{LO}}{8\tau}\right) + \frac{1}{\pi}\right]\frac{R_{IF}}{R_{IF}cos\varphi + \frac{\sqrt{2}\pi}{4}\left(1 - \frac{T_{LO}}{8\tau}\right)Z_{RF}}\ V\ sin\varphi \quad (3.20)$$

In the next paragraphe, we determine the up-converted voltage $V_{in1}(t)$ (see Figure 3.13(b) for the whole mixer.

4.4. The voltage $V_{in1}(t)$ of the full mixer

According to [102] and [111], the passive mixer's bilateral characteristic allows current to flow through the switches (transistors) in both directions. In other words, the mixer may work in both ways. The baseband voltages for the four LO phases that are transformed to high frequencies (RF side) can be added since the four LO phases do not overlap in time. From Figure 3.14(b) the baseband voltages are: $V_{IZ2}(t) = -V_{IZ1}(t)\ and\ V_{QZ2}(t) = -V_{QZ1}(t)$. Then the up-converted voltage $V_{in1}(t)$can be found using the following equation:

$$V_{in1}(t) = 2V_{IZ1av}\left(VI_{LO+}(t) - VI_{LO-}(t)\right) + 2V_{QZ1av}.\left(VQ_{LO+}(t) - VQ_{LO-}(t)\right) \quad (3.21)$$

To find the components of $V_{in1}(t)$, first we represent the LO signals by their Fourier Series as follows:

$$VI_{LO+}(t) = \sum_{n=-\infty}^{n=+\infty} C_n\, e^{(jnw_{LO}t)} \quad (3.22)$$

$$VI_{LO-}(t) = \sum_{n=-\infty}^{n=+\infty} (-1)^n C_n\, e^{(jnw_{LO}t)} \quad (3.23)$$

$$VI_{LO+}(t) = \sum_{n=-\infty}^{n=+\infty} e^{\left(-jn\frac{\pi}{2}\right)} C_n \, e^{(jnw_{LO}t)} \tag{3.24}$$

$$VI_{LO+}(t) = \sum_{n=-\infty}^{n=+\infty} e^{\left(jn\frac{\pi}{2}\right)} C_n \tag{3.25}$$

Where

$$C_n = \frac{1}{T_{LO}} \int_{-\frac{T_{LO}}{2}}^{\frac{T_{LO}}{2}} VI_{LO+}(t) e^{(-jnw_{LO}t)} dt = \frac{1}{T_{LO}} \int_{0}^{\frac{T_{LO}}{4}} e^{(-jnw_{LO}t)} dt = \left(\frac{1}{4}\right) sinc\left(\frac{n\pi}{4}\right) \frac{1}{T_{LO}} e^{\left(-jn\frac{\pi}{4}\right)} \tag{3.26}$$

$C_n =$

By replacing the LO signals by their Fourier Series in (3.21) we obtain (3.27):

$$V_{in1}(t) = 2V_{IZ1av}.2\left(\sum_{n=1,3,5}^{n=+\infty} C_n \, e^{(jnw_{LO}t)}\right)$$

$$+2V_{QZ1av}.2\left(\sum_{n=1,3,5}^{n=+\infty} e^{\left(-jn\frac{\pi}{2}\right)} C_n \, e^{(jnw_{LO}t)}\right) \tag{3.27}$$

If we ignore the harmonic components of the odd frequencies of order 3 and more of LO, we can find the up-converted voltage Vin1(t) in (3.28) and (3.29):

$$V_{in1}(t) = 4V_{IZ1av}C_1 e^{j(w_{LO}t)} - j4V_{QZ1av}C_1 e^{j(w_{LO}t)} \tag{3.28}$$

where $c_1 = \left(\frac{1}{4}\right) sinc\left(\frac{\pi}{4}\right) e^{\left(-\frac{j\pi}{4}\right)}$

$$V_{in1}(t) = 4V_{IZ1av}\frac{1}{\pi\sqrt{2}} e^{j\left(w_{LO}t-\frac{\pi}{4}\right)} + j4V_{QZ1av}\frac{1}{\pi\sqrt{2}} e^{j\left(w_{LO}t-\frac{\pi}{4}\right)} \tag{3.29}$$

using equations (3.19), (3.20), and (3.29) the fundamental component of the up-converted voltage at frequency f_{lo}, $V_{in1,flo}$ is obtained in (3.30) :

$$V_{in1,flo} = \frac{2}{\pi\sqrt{e}}\left[\frac{1}{2}\left(1-\frac{T_{LO}}{8\tau}\right)+\frac{1}{\pi}\right]\frac{R_{IF}}{R_{IF}cos\varphi+\left(1-\frac{T_{LO}}{8\tau}\right)Z_{RF}} V_{RF} \tag{3.30}$$

the amplitude of Vin1,flo depends on the capacities C_{rf}, C_{IF}, the period T_{LO} and cosφ.

With the approximation ($\frac{T_{LO}}{8\tau} \ll 1$) equation (3.30) can be simplified into (3.31) and (3.32):

$$V_{in1,flo} = \frac{\pi+2}{\sqrt{2}\pi^2}\frac{R_{IF}}{R_{IF}cos\varphi+\frac{\sqrt{2}\,\pi}{4}Z_{RF}} V_{RF} \tag{3.31}$$

$$V_{in1,flo} = 0.3686\frac{R_{IF}}{R_{IF}cos\varphi+1.11Z_{RF}} V_{RF} \tag{3.32}$$

4.5. (LTI) linear Time-invariant equivalent circuit of the 25% duty cycle double-balanced passive mixer

The fundamental term of the current at the input of the mixer (Figure 3.13(a)) $I_{int,flo}$ is given by (3.33):

$$I_{int,flo} = \frac{V_{RF} - V_{in1,flo}}{Z_{RF}} \tag{3.33}$$

According to equation (3.33) and (3.34) the fundamental current can be found.

$$I_{int,flo} = \frac{V_{RF}(t) - V_{in1,flo}(t)}{Z_{RF}} = \frac{\frac{\sqrt{2}\pi}{4} Z_{RF} + R_{IF}\left(cos\varphi - \frac{\pi+2}{\sqrt{2}\pi^2}\right)}{Z_{RF} R_{IF} cos\varphi + \frac{\sqrt{2\pi}}{4} {Z_{RF}}^2} V_{RF} \tag{3.35}$$

From (3.35) it is possible to write the expression between $V_{RF}(jw_{RF})$ and $I_{int}(jw_{RF})$ as follows:

$$V_{RF}(jw_{RF}) = \frac{Z_{RF} R_{IF} cos\varphi + \frac{\sqrt{2\pi}}{4} {Z_{RF}}^2}{\frac{\sqrt{2}\pi}{4} Z_{RF} + R_{IF}\left(cos\varphi - \frac{\pi+2}{\sqrt{2}\pi^2}\right)} I_{int}(jw_{RF}) \tag{3.36}$$

Note that if $R_{IF} \to \infty, V_{RF} = \frac{Z_{RF} cos\varphi}{\left(cos\varphi - \frac{\pi+2}{\sqrt{2}\pi^2}\right)} I_{int,flo}$, then there is an equivalent impedance Z_{in} parallel with R_{IF}.

If $R_{IF} \to 0, V_{RF} \to Z_{RF} I_{int,flo}$. This means that R_{IF} is in series with Z_{RF}.

Now, the double balanced passive mixer with a 25% duty cycle shown in Figure 3.13(a) can be presented by a linear invariant time equivalent circuit LTI in Figure 3.16 for $\omega_{IF} = 0$ and by the circuit in Figure 3.17 when $w_{IF} \neq 0$. In these models, the weighting factor α estimated for the conversion gain, and Z represents an additional energy loss due to the harmonics converted from the baseband side to the RF side (up-converted). Note that these circuits are valid only if the harmonic components of the third-order and higher odd frequencies of the LO are ignored.

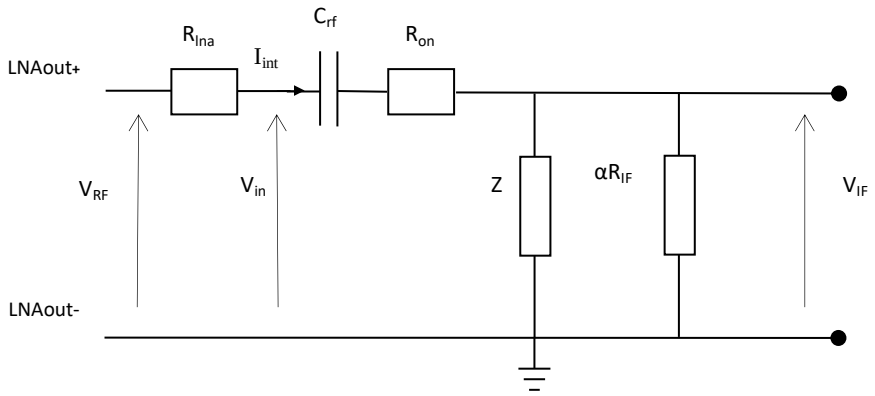

Figure 3.16. *LTI equivalent circuit of the 25% duty cycle fully differential double-balanced passive mixer ($\omega_{IF} = 0$).*

Part of the circuit equivalent to Figure 3.16 of the tension VRF(jωRF) is not parring (30):

$$V_{RF}(j\omega_{RF}) = I_{int}(j\omega_{RF})[Z_{RF}(j\omega_{RF}) + Z(j\omega_{RF}) \parallel \alpha R_{IF}] \tag{3.37}$$

$$V_{RF}(j\omega_{RF}) = I_{int}(j\omega_{RF}) \left[\frac{\alpha Z_{RF}(j\omega_{RF})R_{IF} + Z_{RF}(j\omega_{RF})Z(j\omega_{RF}) + \alpha Z(j\omega_{RF})R_{IF}}{Z(j\omega_{RF}) + \alpha R_{IF}}\right] \tag{3.38}$$

where $Z_{RF}(j\omega_{RF}) = R_{lna} + \frac{1}{jC_{rf}\omega_{RF}} + R_{on}$

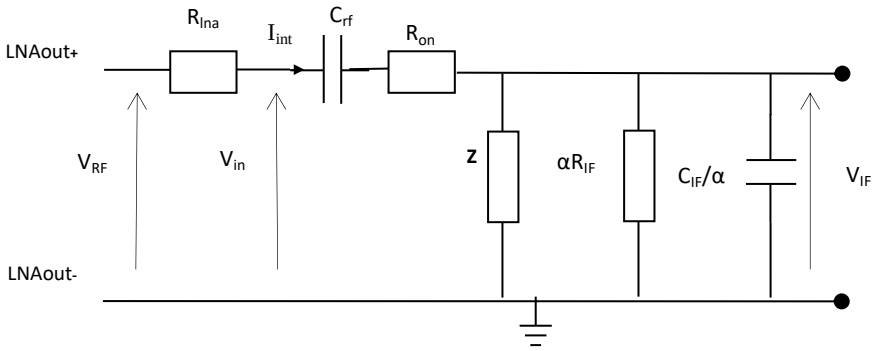

Figure 3.17. *Linear time invariant equivalent circuit of the 25% duty cycle fully differential double-balanced passive mixer ($\omega_{IF} \neq 0$)*

By writing the RF voltage from equation (3.36) equal to the RF voltage from equation (3.38) we can find the factor α and the shunt (parallel) impedance Z.

$$\alpha = \frac{2}{\pi^2} + \frac{4}{\pi^3} \approx 0.33205 \tag{3.39}$$

For $0° \leq \varphi \leq 45°$,

$$Z(jw_{RF}) = \frac{\frac{\pi+2}{\sqrt{2}\pi^2}}{cos\varphi - \frac{\pi+2}{\sqrt{2}\pi^2}} Z_{RF}(jw_{RF}) = \frac{\frac{\pi+2}{\sqrt{2}\pi^2}}{cos\varphi - \frac{\pi+2}{\sqrt{2}\pi^2}} \left(R_{ina} + \frac{1}{jC_{rf}w_{RF}} + R_{on}\right) \quad (3.40)$$

For $45° \leq \varphi \leq 90°$,

$$Z(jw_{RF}) = \frac{\frac{\pi+2}{\sqrt{2}\pi^2}}{sin\varphi - \frac{\pi+2}{\sqrt{2}\pi^2}} Z_{RF}(jw_{RF})$$

$$= \frac{\frac{\pi+2}{\sqrt{2}\pi^2}}{sin\varphi - \frac{\pi+2}{\sqrt{2}\pi^2}} \left(R_{ina} + \frac{1}{jC_{rf}w_{RF}} + R_{on}\right) \quad (3.41)$$

4.6. Input impedance of fully differential doubly balanced passive mixer with 25% duty cycle

The input impedance of the mixer must match the output impedance of the LNA in order to have maximum power transmission between the LNA and the mixer. It's crucial to identify the mixer's input impedance expression. However, because a passive mixer's circuit is time-varying, we are unable to calculate its input impedance by introducing a voltage or current source to the input port. We will show how the mixer's input impedance may be determined using the LTI equivalent circuit. The analogous circuit depicted in Figure 3.17 may be used to write the mixer input impedance for $w_{IF} = 0$. It looks like this:

$$Z_{in} = \frac{V_{in}}{I_{int}} = R_{on} + \frac{1}{jC_{rf}w_{RF}} + [Z(w_{RF}) \| \alpha R_{IF}] \quad (3.45)$$

For $w_{IF} \neq 0$, the input impedance can be written from the equivalent circuit in Figure 3.17 as follows

$$Z_{in} = \frac{V_{in}}{I_{int}} = R_{on} + \frac{1}{jC_{rf}w_{RF}} + [Z(w_{RF}) \| \alpha Z_{IF}(w_{IF})] \quad (3.46)$$

Where $Z_{IF}(w_{IF}) = R_{IF} \left\| C_{IF} = \frac{R_{IF}}{1+jR_{IF}C_{IF}w_{IF}} \right.$

The amplitude of Zin depends on the ON resistance of the transistor (Ron), the output impedance of the LNA (R_{LNA}), the capacitors (C_{rf}), $Z_{IF}(w_{IF})$, cosφ for the I channel, and

sinφ for the Q channel. To take into account the two channels I and Q in the LTI model, we must consider cosφ=sinφ. Which means taking φ = 45deg.
We can note that in order to adapt Zin of connect to the output impedance of the LNA equation (3.46) it shows that the input impedance of Zin may be adjustable by changing RIF. The adjustment range is limited as follows:

$$\left|R_{on}+\frac{1}{jC_{rf}w_{RF}}\right| < |Z_{in}| < \left|R_{on}+\frac{1}{jC_{rf}w_{RF}}+Z(w_{RF})\right| \quad (3.47)$$

This result is very important because one can eliminate the LNA, directly connect the 50Ω impedance antenna to the mixer, and achieve impedance matching for maximum power transfer by varying R_{IF} on the baseband side. In this case, the amplification operation will be done easily and without constraint at the low IF frequency.

5. Receiver simulation results

5.1. Simulation results in time domain

Given that the proposed receiver is a time-variant circuit, we start by presenting its time domain simulation. The LO frequency is set at 4 GHz, and the duty cycle equals to 25%. Figure3.18 shows the time representation of the V_{in}, V_{in}Mixer and V_{if} signals corresponding to one period of the baseband signal (V_{if}).

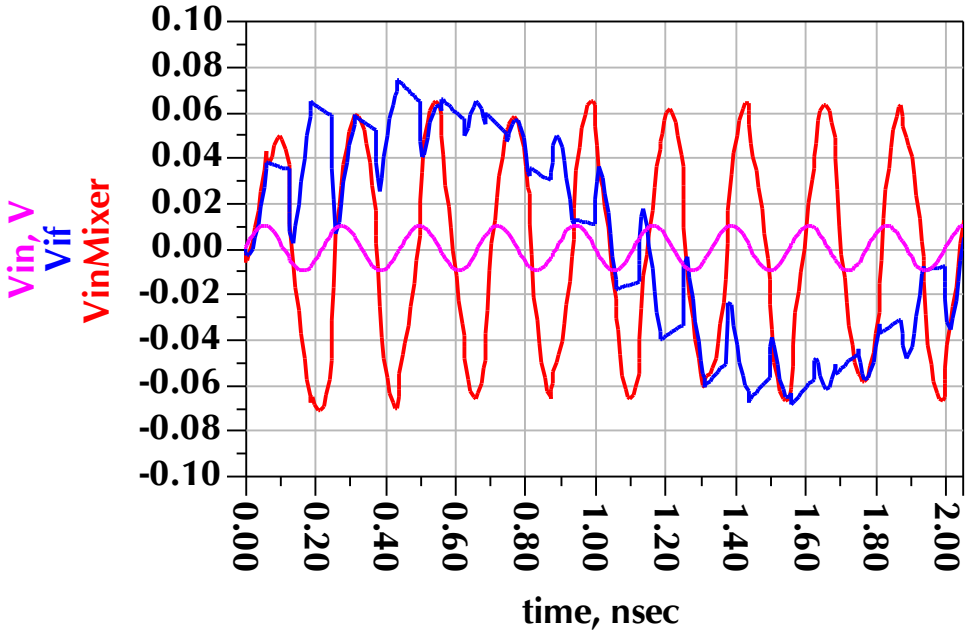

Figure 3.18. *Time representation of V_{in}, V_{in}Mixer and V_{if}.*

Figure 3.18 shows the time domain simulation results at each node of the UWB receiver circuit from the RF side to the IF side of the circuit shown in Figure.3.11.

The receiver output spectrum (V_{if}_spectrum) and the up-converted signal spectrum (V_{in}Mixer_spectrum) are presented in Figure3.19.

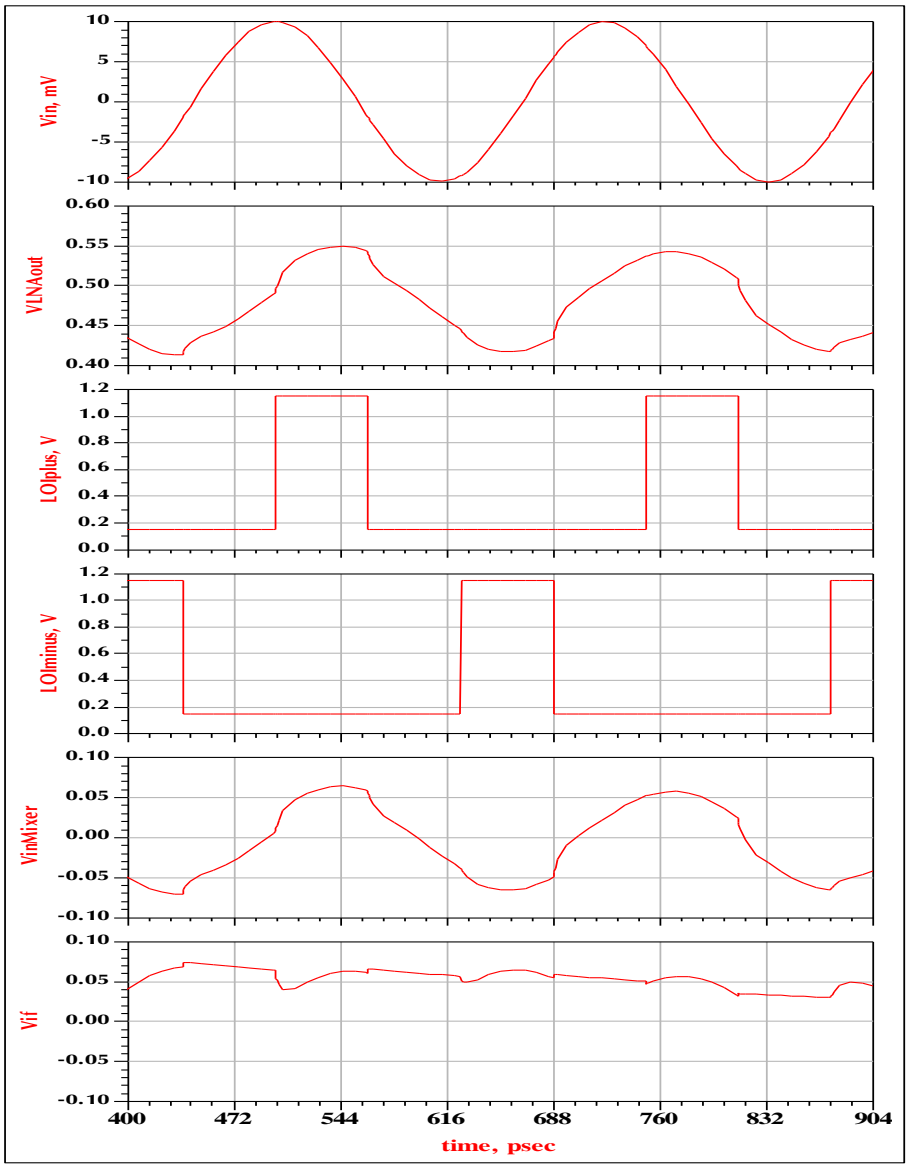

Figure 3.19. *Time representation of V_{in}, V_{LNAout}, LOIplus, LOIminus, V_{in}Mixer and V_{if} signals.*

Figure 3.19 shows the time domain simulation results at each node of the UWB receiver circuit from the RF side to the IF side of the circuit shown in Figure 3.11. The receiver output spectrum (V_{if}_spectrum) and the up-converted signal spectrum (V_{in}Mixer_spectrum) are presented in Figure3.20. V_{if}_spectrum include the IF constituent of interest is located at (f_{RF}– f_{LO}= 0.5 GHz), the image constituent is located at (f_{RF}+ f_{LO}= 8.5 GHz) and the odd high order harmonics and inter modulation products are located at ($3f_{LO}$ – f_{RF}= 7.5 GHz). This intermodulation product component is 16.7 dB under the component of interest level. Given the transparency property of this mixer, it simultaneously down-converts the RF signals (V_{in}Mixer) to IF signals (V_{if}) and up-converts those to RF.

The up-converted voltage spectrum (i.e. V_{in}Mixer_spectrum) contains the RF component at the mixer input (f_{RF} = 4.5 GHz) and the harmonics component at (7.5 GHz + f_{LO} = 11.5 GHz) that is outside the UWB frequency range (3.1–10.6 GHz). The RF feed through rejection (at 4.5 GHz) is 78 dB and the LO feed through rejection (at 4 GHz) is 60 dB. These results show that the proposed receiver with the down-conversion differential double-balanced passive mixer has a good ports isolation performance.

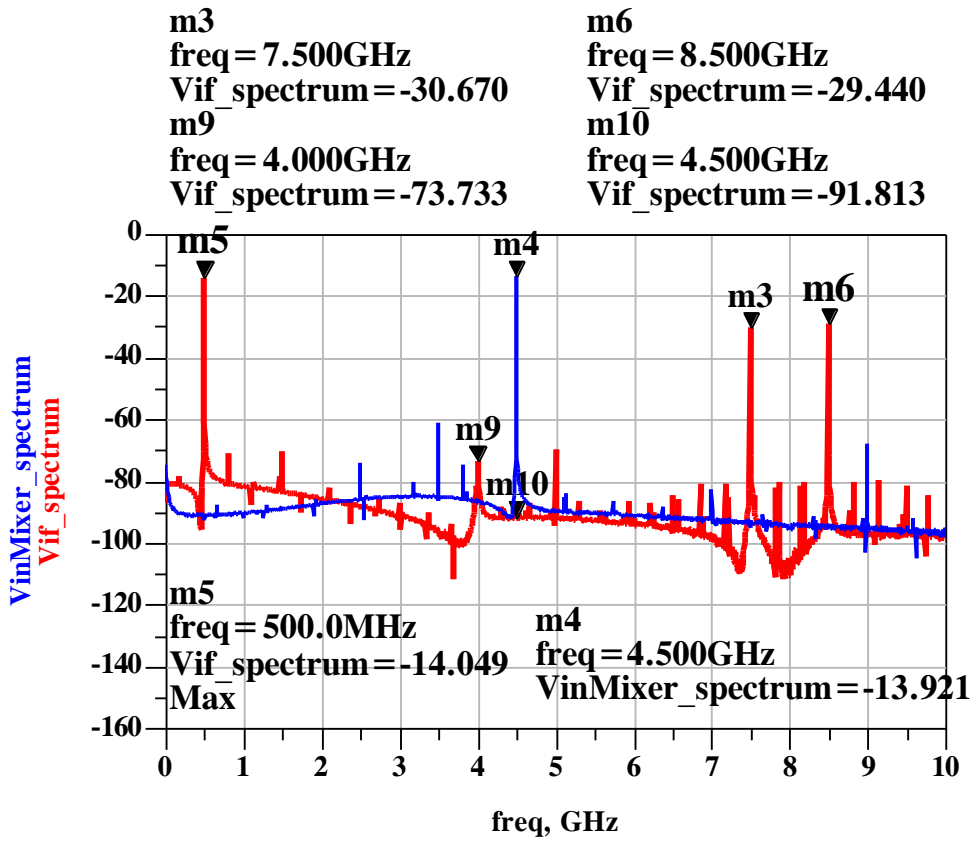

Figure 3.20. *Receiver output spectrum (Vif_spectrum) and mixer input spectrum (VinMixer_spectrum) in dBm.*

Table 3.1 indicates that the receiver exhibits an excellent conversion gain of approximately 16 dB, while the differential double-balanced passive mixer incurs a conversion loss of approximately 0.13dB only. These values are very competitive.

Table 3.1 Conversion gain of the receiver (RX) and the mixer

Conv_GainMixer	Conv_G_dBMixer	Conv_GainRx	Conv_G_dBRx
0.985	-0.128	6.275	15.952

5.2. Receiver linearity performance

We run on ADS tool harmonic balance simulation to determine the linearity performance of the receiver. Figure3.21 shows the receiver gain versus the LNA input power in dBm. The receiver achieves a gain of more than 16 dB for an input power less than 20 dBm which is regarded as a good value. Figure 3.22 shows that the 1dB compression point P_{-1dB} equals to -12.77 dBm. To evaluate the distortion performance of the receiver's front end, a simulation was conducted for third and second-order inter modulation intercept inputs IIP3 and IIP2 as shown in Figure 3.23 and Figure3.24. An IIP3 of 3.14 dBm and an IIP2 of 17.5 dBm were achieved. The proposed mixer-based UWB receiver front end consumes 7.6 mW from a 1.8-V power supply, while the passive mixer consumes nearly zero power (0.72 pW).

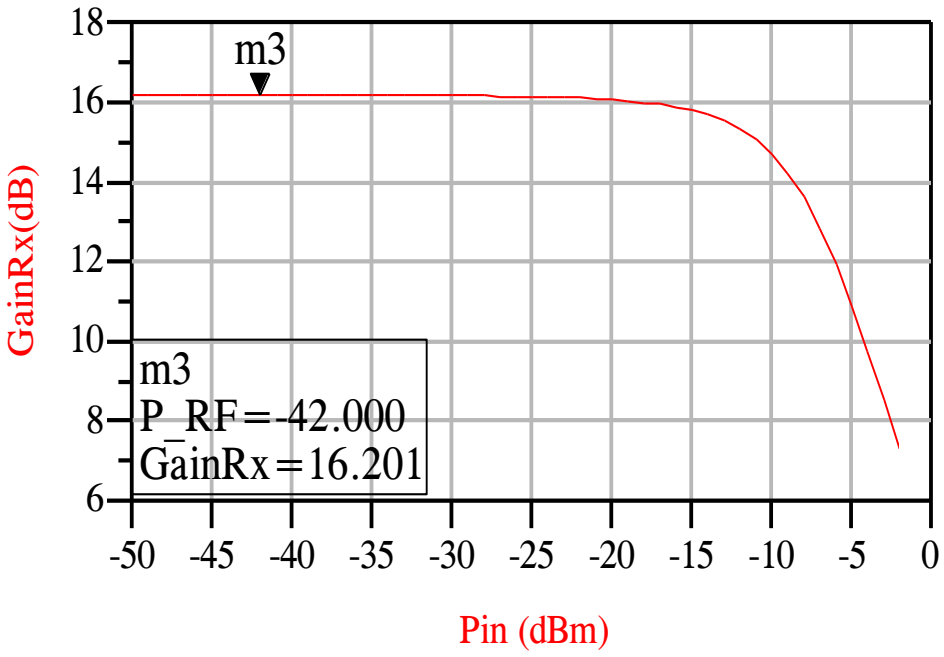

Figure 3.21. *Fiure.3.20. Receiver gain*

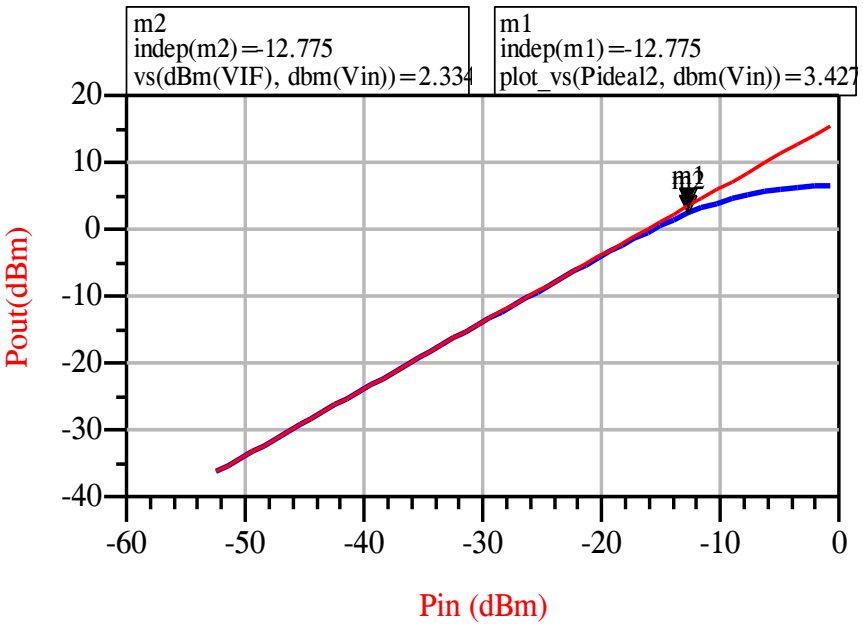

Figure 3.22. *P_{-1dB} of the receiver.*

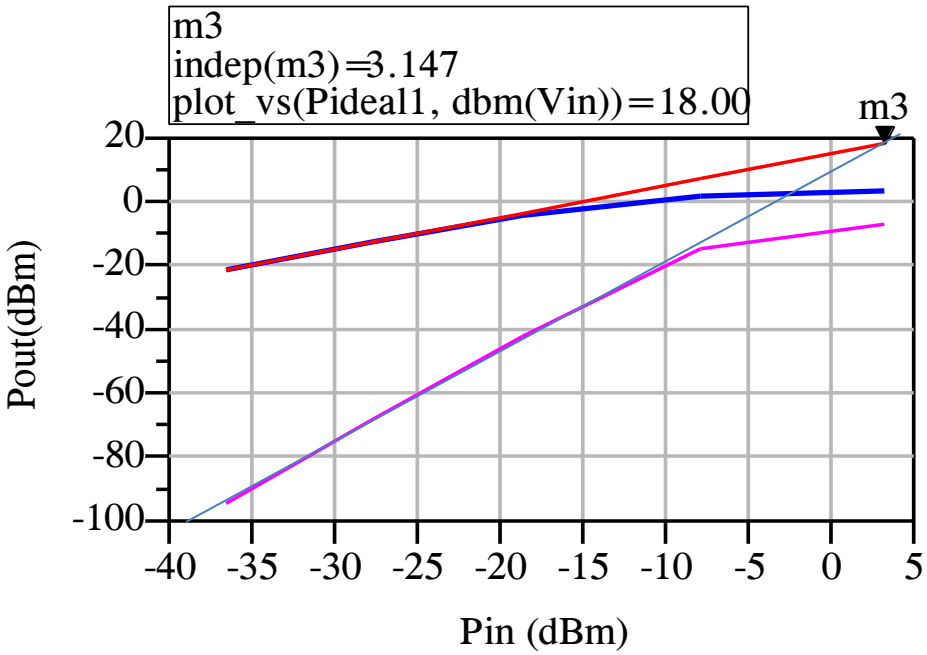

Figure 3.23. *IIP3 of the receiver.*

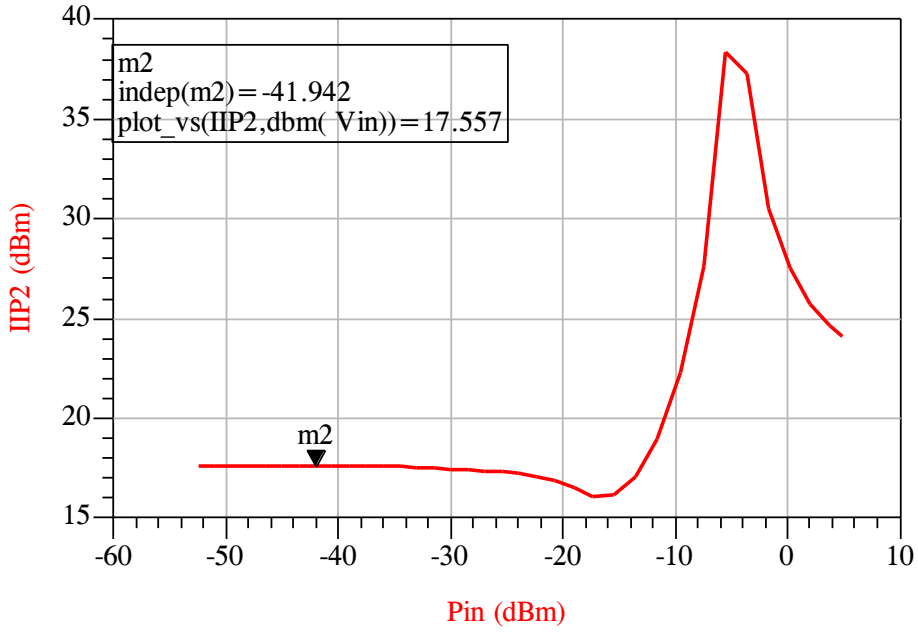

Figure 3.24. *IIP2 of the receiver.*

Table 3.2 shows a comparison with previously published UWB receivers. We can see that the proposed double balanced passive mixer-based UWB receiver archives the best performances in term of linearity, input return loss, ports isolation and power consumption. Also the proposed LNA circuit has the highest gain and a comparative noise figure to the other references

Table 3.2 comparison with previously published receiver.

	This work	[69]	[112]	[113]	[114]
CMOS technology (nm)	180	180	180	90	180
Bandwidth (GHz)	3-5	3-5	3.15–3.9	3-5	3-5
LNA gain (dB)	25.3	16.8	18	15	17
LNA NF (dB)	2.9	2.6-3.1	10	3.1	2.5-3.5
Receiver gain (dB)	16	15	31	6	8
Receiver IIP3 (dBm)	3.14	-3.4	-15	-	0.5
Receiver S11 (dB)	<-12.5	<-10.1	<-9	<-10	<-12
Port isolation (dB) LO_IF - RF_IF	60-78	-	25-25	-	-
Receiver power cons. (mW)	7.6	35.1	99	22.3	26.6

6. Conclusion

In this chapter, a differential passive mixer-based UWB receiver front-end was designed and analyzed, using TSMC RF 0.18 μm CMOS process. The front-end circuit utilizes an inductorless balun LNA and a 25% duty cycle double-balanced passive mixer. Operating at 3–5 GHz, the receiver front-end exhibits a gain of 16 dB an IIP3 of 3.14dBm and an IIP2 with 17.5 dBm leading to improved linearity.

The designed receiver demonstrated an excellent RF and LO feed through rejection. Therefore the proposed double balanced passive mixer-based UWB receiver with differential topology is a good candidate to be integrated in a single chip UWB transceiver for WBAN medical application.

Chapter 4

System level simulation and analysis of device Mismatches effect on the UWB Receiver

1. Introduction

This chapter consists of two parts the first part explains the modeling for our receiver. This part presents a chirp spread spectrum receiver operating in the 3-5 GHz UWB for WBAN medical applications. The receiver uses direct conversion architecture without RF bandpass filter. Modeling, design, and simulations of the entire receiver architecture are described. Time domain and frequency domain analysis and simulation were done to determine the receiver's optimized blocks parameters[115].

The second part presents an analysis of MOSFET transistors mismatches effect on the performance of UWB receiver front-end which constitutes the most important part of the Wireless Body Area Network sensor node. In order to calculate the mixer offset current and the LNA output offset voltage, relevant mismatch models for PMOS and NMOS transistors were developed. Using a 0.18-m CMOS process, Monte Carlo and harmonic balancing simulations were used to determine how W/L and V_{th} mismatches affect receiver gain and IIP2.

2. System level simulation of the complet receiver

2.1. Chirp FSK Modulation

The choice of modulation is limited by the constraints of cost, complexity, power dissipation, and resistance against interference. The aim is also modulation, should allow a non-coherent detection technique that requires a simple demodulator circuit. Based on these considerations, we propose a new modulation technique: Chirp FSK, also called double band (dual band) BFSK: Instead of assigning each bit a particular frequency, a fixed sub-band B_0 is assigned for bit '0' and B_1 for bit '1'. This technique is also called LFM (Linear Frequency Modulation).

This LFM or Chirp modulation technique, having the property of pulse compression, is one of the oldest spread spectrum methods (Spread Spectrum), developed for the use of radars during the 1940s[116]. Among the reasons for this choice are the good performance in terms of

distortion and interference rejection which allows a minimum of energy consumption for its implementation [117]. The principle of this modulation consists of the use of a large bandwidth called Chirp Modulation (CM). During a given pulse, the CM carrier sweeps over a wide band. Most chirp systems use a linear sweep pattern.

The linear chirp signal in Figure 4.1 can be represented by equation (4.1):

$$c(t) = A_p.\cos(2\pi f_0 t + \varphi(t)) \qquad 0 \le t \le T \tag{4.11}$$

Where f_0 is the initial chirp frequency, T is the duration of a chirp pulse, and the instantaneous phase $(2\pi f_0 t + \varphi(t))$ varies linearly with time. The instantaneous frequency f(t) is given by (4.2):

$$f(t) = \frac{1}{2\pi}\frac{d}{dt}\left((2\pi f_0 t + \varphi(t)\right) = f_0 + \frac{1}{2\pi}\left(\frac{d}{dt}\varphi(t)\right) \tag{4.2}$$

Considering $\varphi(t) = 2\pi S_r t^2 + \varphi_0$ where S_r and φ_0 are constant then $f(t)$becomes (4.3):

$$f(t) = f_0 + 2S_r t = f_0 + R.t \tag{4.3}$$

Note that the instantaneous frequency is a linear function of time with a slope R expressed by (4.4):

$$R = 2S_r = \frac{B}{T} \tag{4.4}$$

where B is the band width . R is the chirp speed.

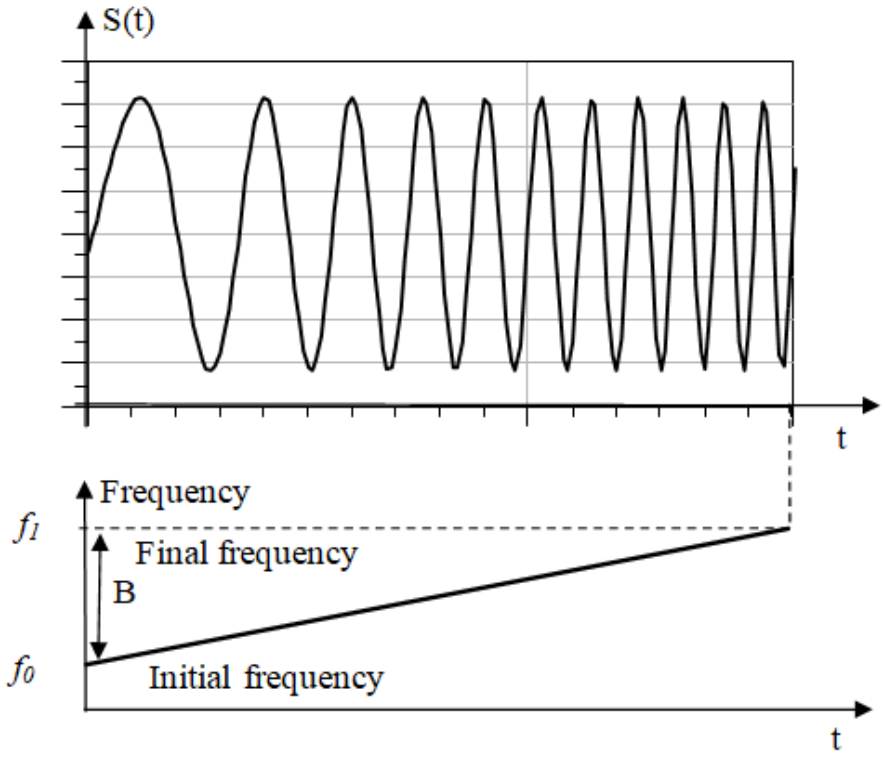

Figure 4.1. *Chirp signal and frequency versus time.*

So, the instantaneous frequency is increasing or decreasing during the duration of the pulse, and band B is equal to the interval of the swept frequency. For an increase in the instantaneous frequency (up chirp), the expression of the LFM signal is given by (4.5):

$$c(t) = A_p.\cos(2\pi f_0 t + \pi R t^2 + \varphi_0) \tag{4.5}$$

For a decrease in the instantaneous frequency (down chirp), the LFM signal can be represented by (4.6):

$$c(t) = A_p.\cos(2\pi f_0 t + \pi R(t^2 - 2T.t) + \varphi_0) \tag{4.6}$$

2.2. System level implementation under ADS

ADS tool was used to simulation the receiver. The schematic template used for receiver simulation is shown in Figure 4.2. The Chirp spread spectrum (CSS) UWB transmitter is based on a chirped pulse generator with CSS -FSK modulation. The chirp value is the amount of frequency shift between the beginning and the end of the pulse which corresponds to a frequency bandwidth of 500MHz.

The pulse repetition frequency PRF is set to 10Mp/s. A pulse width (t_p) of 20ns, is used to transmit a sub-band from 4Ghz to 4.5Ghz corresponding to a data bit '1'. From 3.2GHz to 3.7GHz corresponding to a data bit '0'

The UWB signal sent by the transmitter will experience attenuation due to the canal modeled by line of sight link (LOS).

The CSS-UWB received signal is first amplified with a LNA. The LNA signal drives the input of a differential double-balanced down-conversion. The output signal of the mixer is typically filtered by a low pass filter (LPF). The latter passes only the selected down-converted channel signal and suppresses the other channel. Then, in order to create an appropriate dynamic range, an automatic gain control amplifier (AGC-Amp) is used. Finally, the chirp FSK demodulator will retrieve the digital transmitted data (Rx_output data).

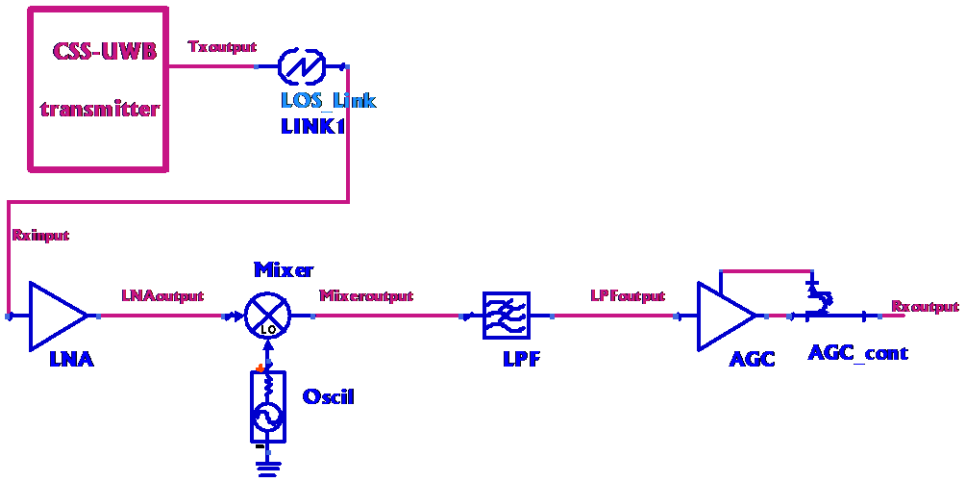

Figure 4.2. *Receiver schematic.*

2.3. Receiver spectrums for minimum and maximum input power

A harmonic balance simulation using the ADS tool is used to evaluate receiver performance for both lowest (sensitivity) and highest receiver input power levels.

The time domain simulation results in Figure 4.3 show the transmitted binary data (Tx_{data}), the chirped spread spectrum (CSS) FSK signal (Tx_{out}) and signals at the receiver input (R_{xin}), LNA output (LNA_{out}), mixer output (Mixerout), LPF output (LPFout) and receiver output (Rxout). This simulation shows that the receiver work properly for an input power level greater than -93.3dBm which constitutes the sensitivity

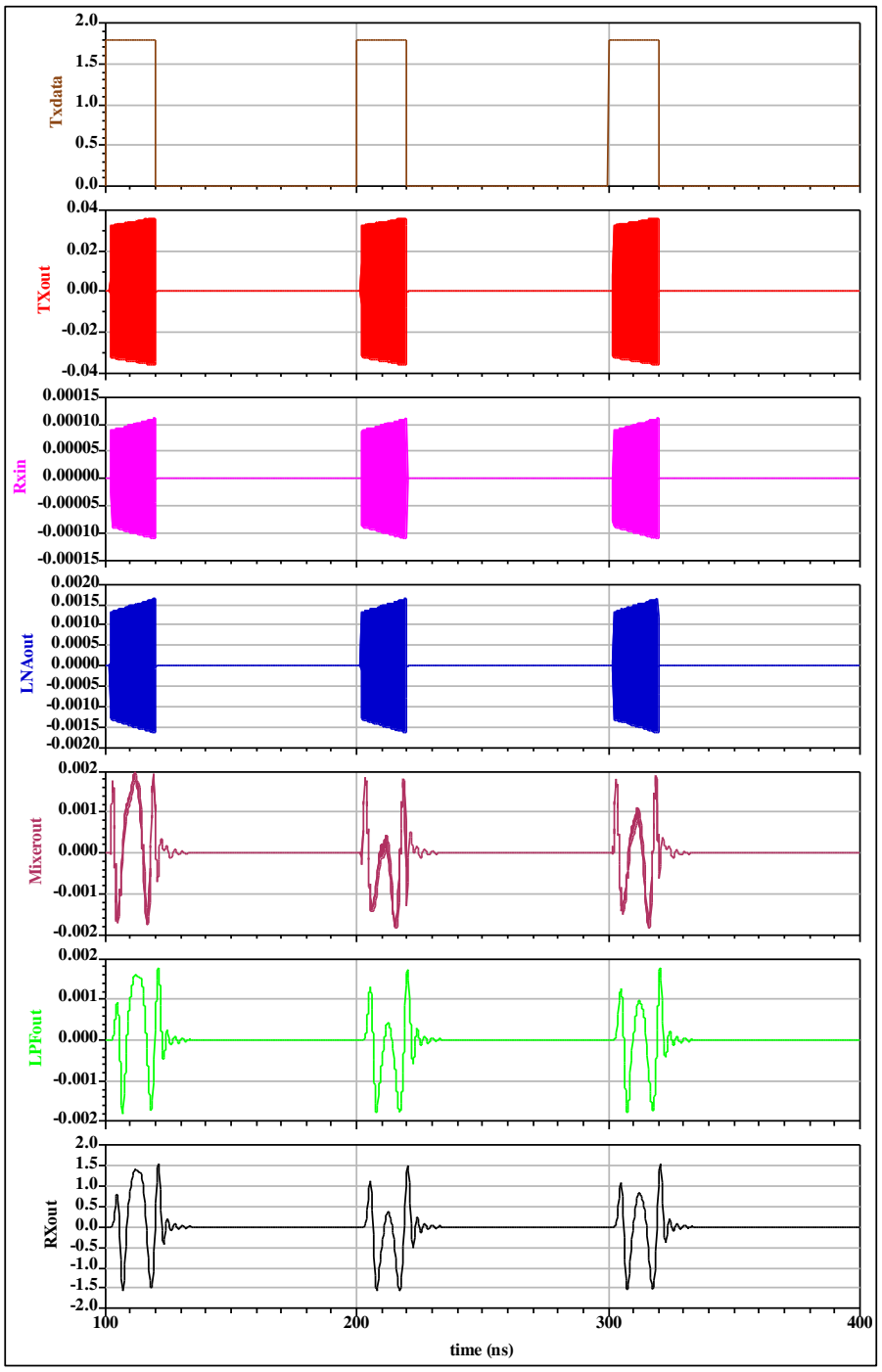

Figure 4.3. *Time representation of signals at each node of the receiver chain for t_p=20ns, PRF=10Mb/s and a receiver input power level of -93.3dBm*

2.3.1. For receiver maximum input power of -43.1dBm

The receiver maximum input power level is set to -43.1dBm because the FCC regulation set the maximum PSD to -41,3 dBm/Mhz.

Figure 4.4 shows frequency domain signals at each node of the circuit in Figure 4. 2 for a receiver input power at -43.1dBm. As shown, the simulated power spectral density (PSD) of (T_{xout}) and (R_{xin}) meets FCC spectral mask requirement and the 500 MHz bandwidth constrain. It is clear that the receiver performs amplification, down conversion and filtering very well with a maximum receiver output (R_{xout}) power level equals to -7dBm which is sufficient to drive the baseband demodulator.

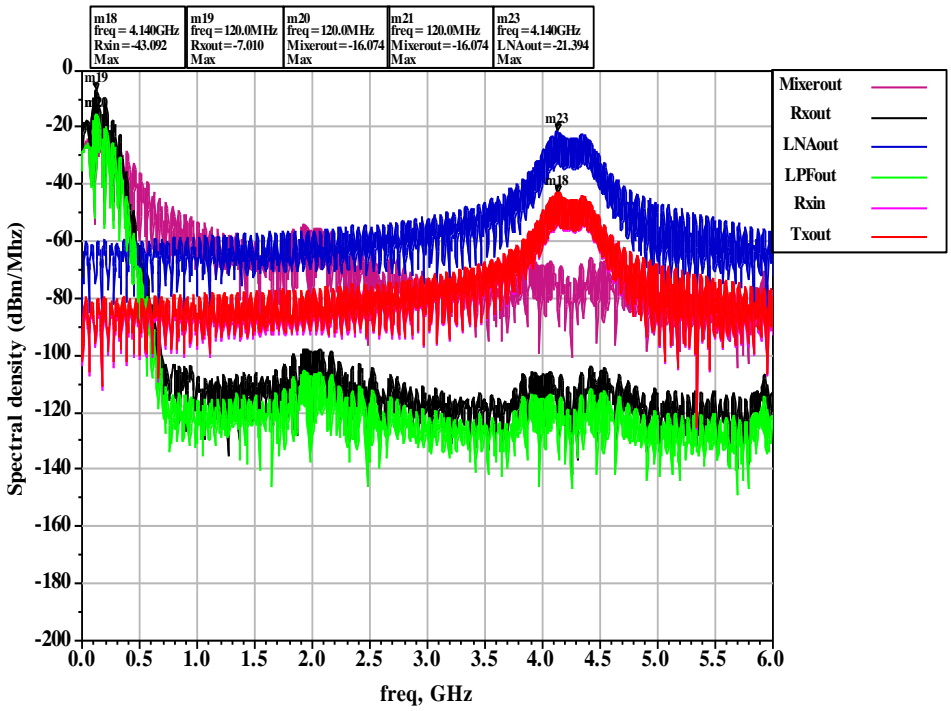

Figure 4.4. *Spectrum at each node of the receiver chain for t_p=20ns, P_{RF}=10Mb/s and a receiver input power level of -43.1 dBm*

2.3.2. For receiver minimum input power of -93.3dBm(Sensitivity=-93.3dBm)

Figure 4.5 shows spectrums at transmitter output (T_{xout}), receiver input (R_{xin}), LNA output (LNA_{out}), mixer output (Mixerout), LPF output (LPF_{out}) and receiver output (R_{xout}) for a receiver sensitivity of -93.3dBm.

From these results we can say that the receiver is robust because even at a minimum input power of -93.3dBm the receiver can retrieve the baseband signal after LNA amplification, a down conversion and successful filtering. (R_{xin}) spectrum respects FCC rules and the receiver maintains a t_p equals to 20ns and P_{RF} equals to 10Mb/s. The output (R_{xout}) power level equals to -4.37dBm able to drive the demodulator.

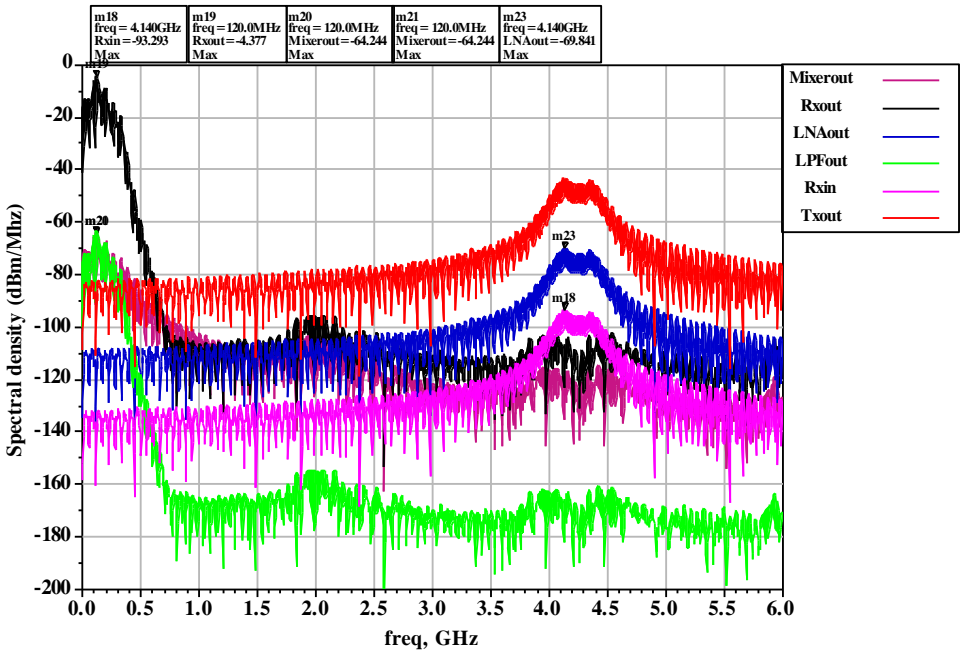

Figure 4.5. *Spectrum at receiver nodes for t_p=20ns, PRF=10Mb/s and a receiverinput power level of -93.3dBm*

2.4. Receiver budget simulation

In order to evaluate the contribution of each block of the receiver chain we run on ADS tool budget simulation.

2.4.1. For receiver maximum input power of -43.1dBm

For receive shown in figure(4.6) the maximum input power of -43.1dBm. Figure 4.7 (a) illustrates a cascaded gain of 39.2dB, Figure 4.7(b) shows a cascaded output power of -4dBm and a cascaded noise figure of 6.1dB is indicated in Figure 4.7(c).

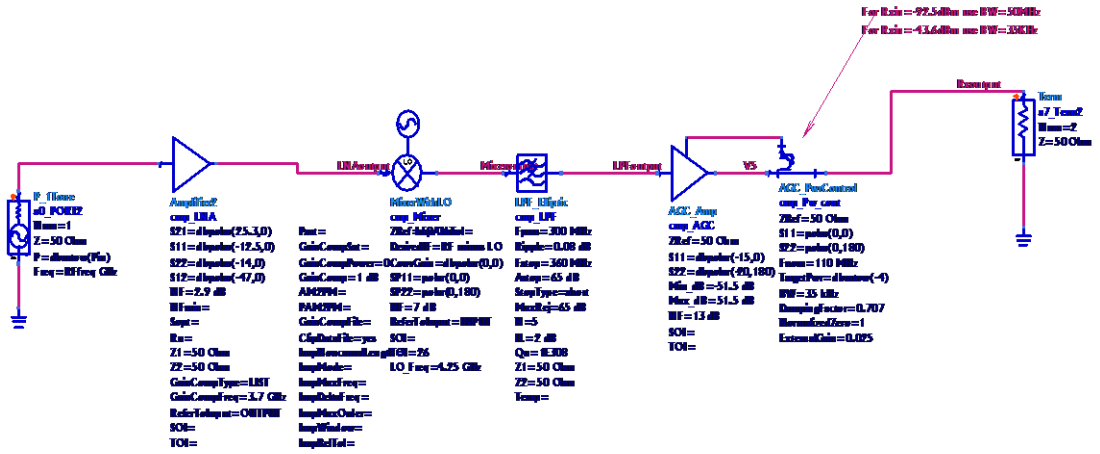

Figure 4.6. *receiver maximum input power of -43.1dBm*

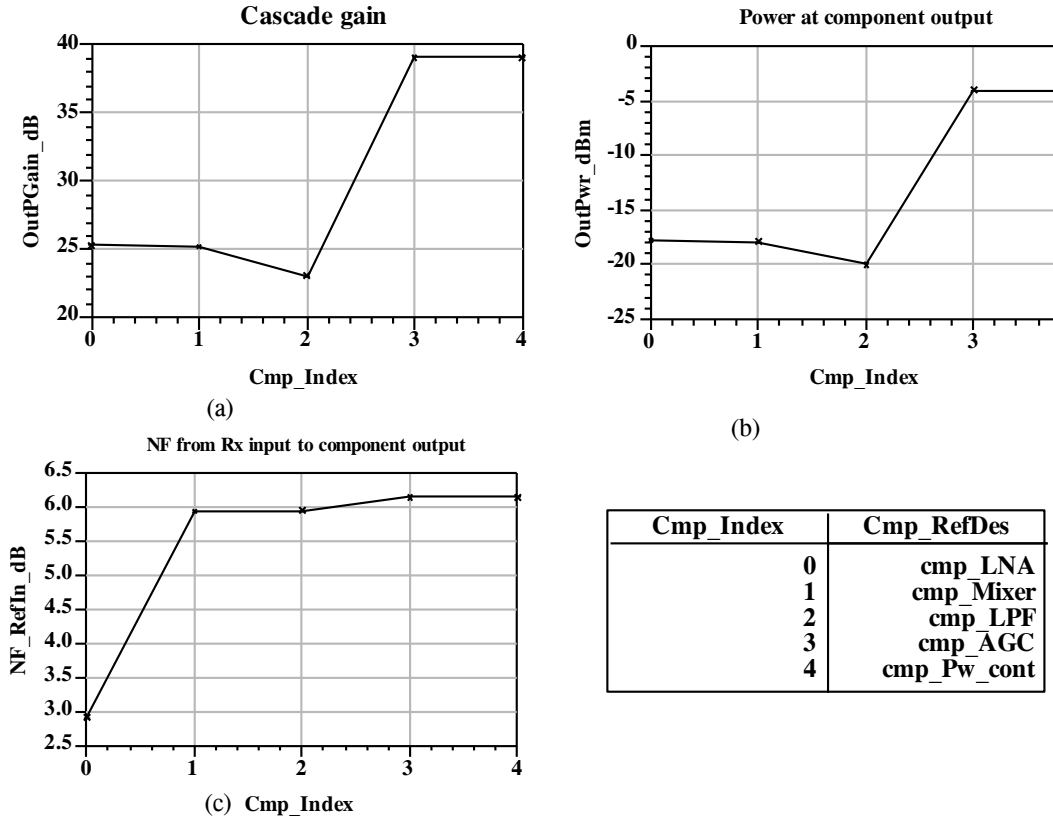

Figure 4.7. *Figure 4.7 (a) cascade voltage gain, (b) cascade receiver output power, (c) cascade NFfor a receiver input power of -43.1dBm*

2.4.2. For receiver minimum input power of -93.3dBm(Sensitivity=-93.3dBm)

For a minimum receiver input power of -93.3 dBm the Figure 4.8(a) illustrates the simulation for a cascaded gain of 85dB, Figure 4.8 (b) shows a cascaded output power of -

10dBm and in Figure 4.8 (c) a cascaded NF of 6.1dB. Figure 4.9 show receiver linearity performance. A 1dB compression point of 0dBm and IIP3 of 11.2dBm are achieved.

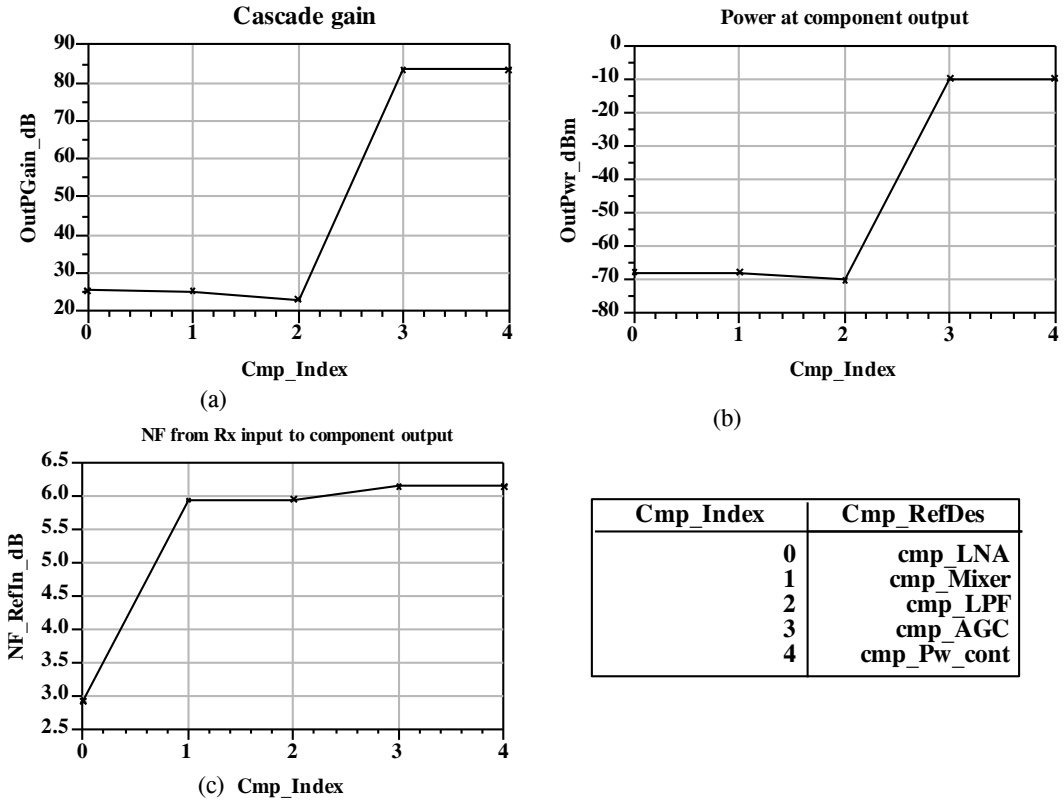

Cmp_Index	Cmp_RefDes
0	cmp_LNA
1	cmp_Mixer
2	cmp_LPF
3	cmp_AGC
4	cmp_Pw_cont

Figure 4.8. *(a) cascade voltage gain, (b) cascade receiver output power, (c) cascade NF for a receiver input power of -93.3dBm*

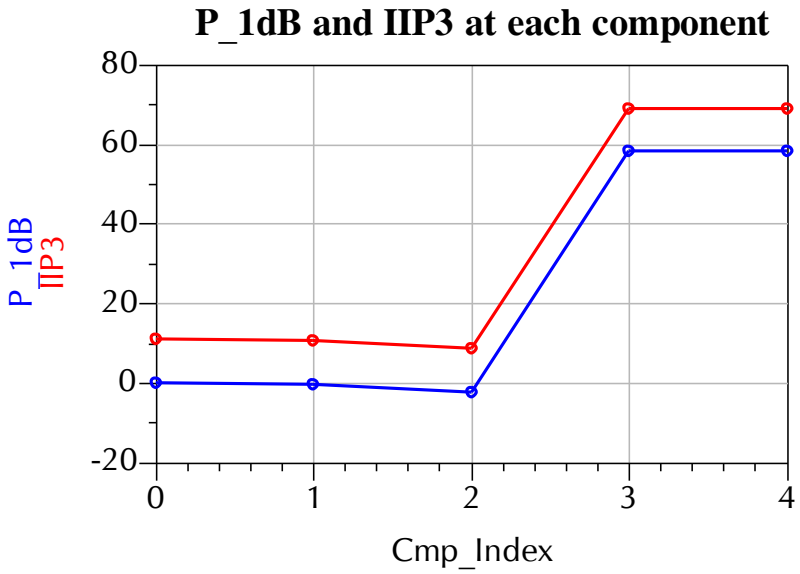

Figure 4.9. *Cascade P_1dB and IIP3*

2.5. Blocks parameters and receiver performance

Table1 lists the optimized circuit blocks required by the receiver front-end

Table 4.1. Circuit blocks requirements

LNA	***Mixer***	***LPF***	***AGC-Amp***
S21= 25.3 dB	Con gain= 0 dB	Fpass= 300 MHz	Max_gain= 60.27 dB
S11= -12.5dB	S11= -10 dB	Fpass= 360 MHz	Min_ gain= -60.27 dB
NF= 2.9 dB	NF= 7 dB	Max rej= 65 dB	S11= -15 dB
P_{-1dB} = 0dBm	P_{-1dB} = 16dBm	ILoss= 2dB	S22= -20 dB
IIP3= 10dBm	IIP3=26dBm	Order 5	NF= 13 dB

Table 4.2 presents the performance summary of the proposed CSS-UWB receiver and its comparisons with other reported state of the art designs. The proposed receiver shows better sensitivity and linearity while achieving better NF than reported design in [118] and [14].

Table 4.2. Comparison with other works

	This Works	[118]	[119]	[120]
Frequency	3-5 GHz	3-5 GHz	3-9 GHz	3-5 GHz
Modulation	CSS- FSK	BPM-BPSK	BPM-BPSK	Dual Band FSK
Tx Transmitted power	<-41.3dBm	<-41.3 dBm	<-41.3dBm	-41.3 dBm
Bandwidth	500 MHz	1.5 GHz	499.2/1331.2MHz	500 MHz
Data Rate	10 Mbps	110kbps	110kbps	3.2 Mbps
Pulse width	20 ns	-	2 ns	75 ns
Sensitivity	-93.3 dBm	-79dBm	-75 dBm	-86 dBm
Noise Figure	6.1 dB	8.3 dB	9.4 dB	5.32 dB
Gain	85 dB	>90 dB	90 dB	99 dB
IIP3	11.2 dBm	-22dBm	-12 dBm	-8.8 dBm

3. Analysis of device Mismatches effect on the receiver performance

It is necessary to design integrated circuits with high immunity to process, voltage, W/L ratio for MOS transistors , and temperature (PVT) variations in order to guarantee stable operation over these variations [121].

The Receiver Front-End (LNA+ Mixer) is one of the key elements of the UWB sensor nodes. When studying differential LNA and Mixer circuits, we make the assumption that the bias currents and characteristics of identical transistors are the same. In practice, MOS devices have a mismatched threshold voltage (Vth) since Vth is dependent on the surface charge density, oxide thickness, gate material, and substrate doping. Dopants are incorporated into the channel and gate areas of the transistor during manufacturing to modify Vth. The doping levels differ erratically from transistor to transistor [122].

Additionally, random variation affects two identical MOS transistors, leading to mismatches in the W/L ratio. Mismatched Vth and W/L ratios cause DC to offset at the circuit nodes. This might cause the circuit's stages to operate nonlinearly or get saturated [123][124].

Time-independent random differences in physical quantities of similarly designed devices are caused by processing-induced device mismatch. As device dimensions shrink and the available signal swing shrinks, the impact of MOS transistor mismatch becomes increasingly significant. For precise analog circuit design, the mismatch is a critical design parameter [125].

The mismatch of two CMOS identical transistors is characterized by the random variation of the difference in their threshold voltage Vth , their body factor, and their current factor.

The second order intercept point (IIP2) of a direct conversion receiver system is a critical performance parameter. It is a measure of second order non-linearity and helps quantify the receiver’s susceptibility to single and 2-tone interfering signals. At high frequencies, due to the presence of parasitic capacitance, the linearity (IIP2) drops[126].

In this section, we will present an analysis of how device mismatches affect the performance of the UWB receiver front-end.

3.1. Mismatch Analysis in LNA

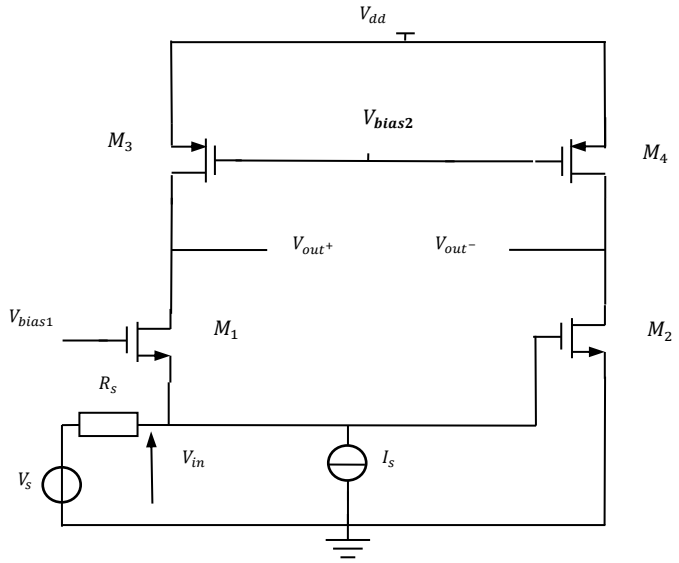

Figure 4.10. *LNA circuit*

Figure 4.10 shows the Low Noise Amplifier circuit. It is based on the Balun topology that converts the single-ended input signal into a differential and uses a common gate stage (CG) (M1) and a common source stage (CS) (M2). The input impedance of this circuit is controlled by M1 transconductance (g_{m1}). When the gains of CS and CG are equivalent and in opposition to each other, the output noise is canceled . The input impedance Z_{inCG} is given by:

$$Z_{inCG} = \frac{r_{oNmos} + r_{oPmos}}{r_{oNmos}(g_{m1} + g_{mb1}) + 1} \tag{4.7}$$

r_{oNmos} and r_{oPmos} are small signal output resistances for NMOS and PMOS transistors respectively.

Furthermore, distortion is decreased, allowing for the development of highly linear LNAs. If the CG-stage input impedance Z_{inCG} is equal to the source resistance R_s, the input impedance can be matched.

$$A_{LNA} = \frac{(V_{out}^{+} - V_{out}^{-})}{V_{in}} = A_{CG} - A_{CS} = 2g_{m1}\frac{r_{oNmos}\, r_{oPmos}}{r_{oNmos} + r_{oPmos}} \tag{4.8}$$

By tuning the DC voltage (V_{bias1}) at M_1 gate, we may change the current in M_2 and get an equal voltage gain at Vout+ and Vout-. The DC voltage (V_{bias2}) is used to adjust LNA gain magnitude and NF by changing the output conductance of M3 and M4 respectively, that operate in the triode region.

3.1.1. PMOS transistor mismatch model for the LNA

In the Triode area, an appropriate MOSFET model is

$$I_D = \mu_P C_{ox} \frac{W}{L} (V_{SG} - V_{th}) V_{SD} \tag{4.9}$$

where I_D is the drain current,V_{SG} is the gate-source voltage, V_{th} is the threshold voltage, with C_{ox} being the gate-oxide capacitance per unit-area, μ_P as the carrier mobility, W and L being the width and length of the transistor respectively.

The objective of the following analysis is to find the value of the PMOS output offset voltage $V_o = V_{SD3} - V_{SD4}$ due to mismatches between transistors M3 and M4.

We pose $V_{th3} = V_{th}$ *and* $V_{th4} = V_{th} + \Delta V_{th}$

$$we\ denote\ the\ ratio\ \frac{W3}{L3} = Rat\ and\ \frac{W4}{L4} = Rat + \Delta Rat$$

Mismatches in PMOS transistors lead to $I_{D3} \neq I_{D4}$

We denote $I_{D3} = I_D$ *and* $I_{D4} = I_D + \Delta I_D$

The currents can be approximated in the triode region (linear region) by:

$$I_{D3} = \mu_P C_{ox} \frac{W_3}{L_3} (V_{SG3} - V_{th3}) V_{SD3} \tag{4.10}$$

$$I_{D4} = \mu_P C_{ox} \frac{W_4}{L_4} (V_{SG4} - V_{th4}) V_{SD4} \tag{4.11}$$

In the following study we neglect $\mu_p C_{ox}\ mismatch$. The output offset voltage is given by:

$$V_o = V_{SD3} - V_{SD4}$$

$$= \frac{I_D}{\mu_p C_{ox} Rat (V_{SG} - V_{th})} - \frac{I_D + \Delta I_D}{\mu_p C_{ox} (Rat + \Delta Rat)(V_{SG} - V_{th} - \Delta V_{th})}$$

$$= \frac{I_D}{\mu_p C_{ox} Rat (V_{SG} - V_{th})} \left[1 - \frac{1 + \frac{\Delta I_D}{I_D}}{(1 + \frac{\Delta Rat}{Rat})(1 - \frac{\Delta V_{th}}{V_{SG} - V_{th}})} \right] \tag{4.12}$$

$$\frac{\Delta I_D}{I_D} \approx -\frac{\Delta Rd}{Rd}$$

where Rd is the equivalent PMOS load for the differential delay circuit.

Assuming $\frac{\Delta Rat}{Rat} \ll 1$, $\frac{\Delta V_{th}}{V_{SG}-V_{th}} \ll 1$ and $\frac{\Delta I_D}{I_D} \ll 1$

equation (4.12) becomes:

$$V_o = \frac{I_D}{\mu_p C_{ox} Rat(V_{SG}-V_{th})}\left[\frac{\Delta Rat}{Rat} + \frac{\Delta Rd}{Rd} - \frac{\Delta V_{th}}{V_{SG}-V_{th}}\right] \quad (4.13)$$

$\frac{I_D}{\mu_p C_{ox} Rat(V_{SG}-V_{th})}$ is approximately equal to the equilibrium source drain voltage V_{SD} of each transistor. This gives:

$$V_o = V_{SD}\left[\frac{\Delta Rat}{Rat} + \frac{\Delta Rd}{Rd} - \frac{\Delta V_{th}}{V_{SG}-V_{th}}\right] \quad (4.14)$$

Equation (4.14) is an important result, revealing the dependence of V_o on device mismatches and bias conditions.

In order to produce high and stable LNA gain and cancel noise correctly we need to minimize $\frac{\Delta Rd}{Rd}$, $\frac{\Delta Rat}{Rat}$, ΔV_{th} and maximize $(V_{SG} - V_{th})$.

3.1.1.1. Simulation result for LNA

The most important flaws are PMOS transistor mismatches and random changes during differential LNA circuit manufacture. We are interested in determine how these incompatibilities affect gain, noise figure, and IIP2. The proposed design's robustness is studied by running a Monte Carlo simulation.

Also, we will evaluate the standard uncertainty given by the following equation:

$$\text{Standard uncertainty} = \text{Std uncertainty} = \text{Std.}\frac{\text{dev}}{\sqrt{n}} = \sqrt{\frac{1}{n(n-1)}\sum_{j=1}^{n}\left(x_j - \bar{x}\ \right)^2} \quad (4.15)$$

where Std.dev is the Standard deviation given by:

$$\text{Std.dev} = \sqrt{\frac{1}{(n-1)}\sum_{j=1}^{n}(x_j - \bar{x}\ )^2} \quad (4.16)$$

n is the number of observations, where $\bar{x}$ is the mean and x_j is the j^{th} data point.

From statistical theory, 95% of the runs are in the range [mean - 2std uncertainty, mean + 2std uncertainty]. 95% is the level of confidence with a coverage factor of 2.

[mean - 2std uncertainty, mean + 2std uncertainty] is called confidence interval.

3.1.2. PMOS size mismatch

A number of Monte Carlo simulations were performed to demonstrate the impact of process modifications on the performance parameters of the LNA. The size of PMOS varied by 5% ($\frac{\Delta \text{Rat}}{\text{Rat}} = \pm 5\%$)

Figure 4.11(a) shows the Monte-Carlo simulation results of the LNA gain. As we see from the histogram data, the variation of $\frac{W}{L}$ value in PMOS transistors affects the gain, when $\frac{W}{L}$ changes by about 5%. From Figure 4.11 (a), we see that the mean of the LNA gain equals 30.15 dB and the standard uncertainty equals 0.0475 dB. These values are good for fabrication. 95% of the runs are in the range [30.055, 30.245]dB.

Figure 4.11(b) shows a gain variation of 25.46 dB to 21.5dB in the 3-5 GHz band, which is acceptable.

Figure 4.12(a) shows the Monte Carlo simulation result for LNA NF in case of PMOS size mismatch the mean=3.146dB, std dev=0.368dB, std uncertainty=0.0184dB and relative uncertainty=0.58%. 95% of the runs are in the range [3.1092, 3.1828] dB. Figure 4.12(b) shows NF vs. frequency.

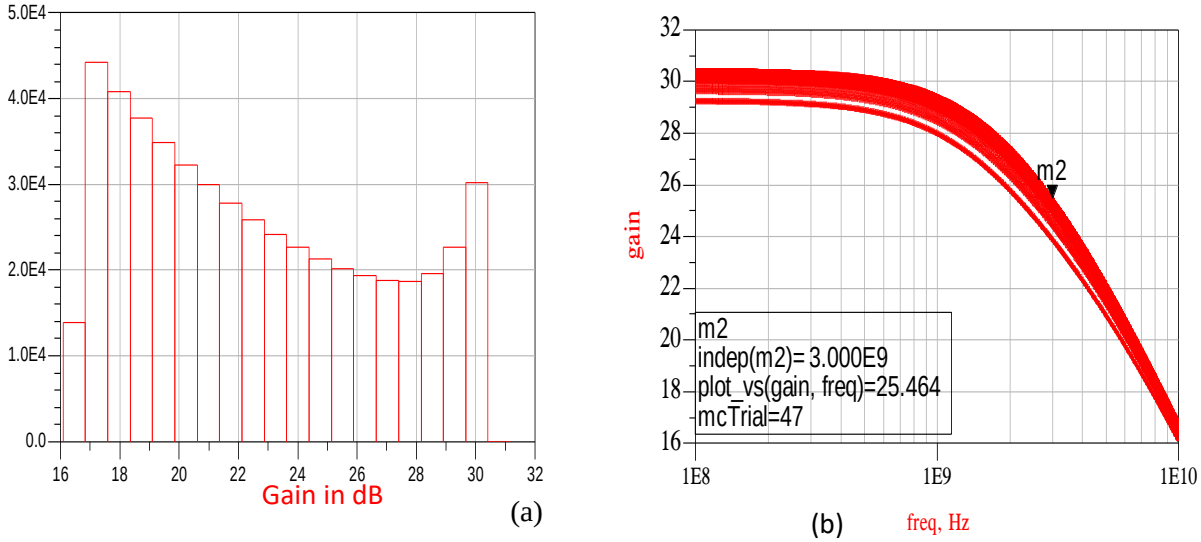

Figure 4.11. *LNA Gain for PMOS size mismatch a) Monte Carol simulation result, mean = 30.15 dB, std dev=0.336dB, std uncertainty=0.0475dB and relative uncertainty=0.157% b) LNA gain vs frequency*

The NF vary from 1.9dB to 3.4dB in the 3-5GHz band. In Figure 4.13, the linearity performance was plotted. In Figure 4.13 (a) Monte Carlo simulation result for LNA IIP2 is presented with a mean of 13.143dBm, a std dev equals to 3.34dBm, a std uncertainty of 0.472dBm and a relative uncertainty of 3.5%. Therefore the confidence interval of IIP2 is [12.199, 14.087]dBm. Figure 4.13 (b) shows LNA IIP2 versus LNA input power Pin. Therefore, the randomness of process due to PMOS size mismatch will affect the second order linearity but will not have a great impact on the gain and NF of the proposed LNA.

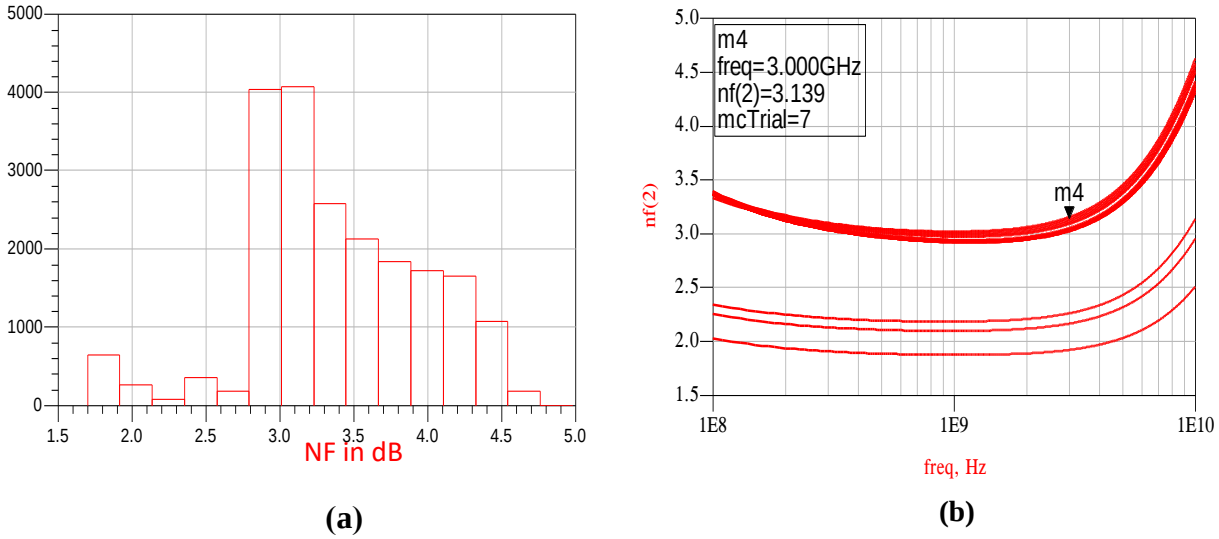

(a) **(b)**

Figure 4.12. *LNA NF for PMOS size mismatch a) Monte Carol simulation result, mean=3.146dB, std dev=0.368dB, std uncertainty=0.0184dB and relative uncertainty=0.58% b) LNA NF vs frequency*

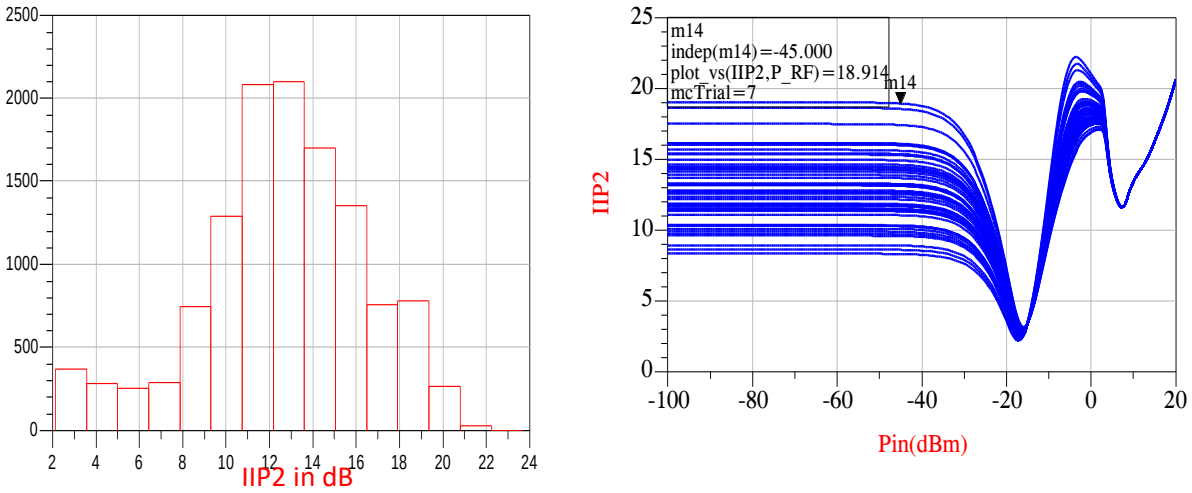

(a) **(b)**

Figure 4.13. *LNA IIP2 for PMOS size mismatch a) Monte Carlo simulation result, mean=13.143 dBm, std dev=3.34dBm, std uncertainty=0.472dBm and relative uncertainty=3.5% b) LNA IIP2 vs Pin*

3.1.3. PMOS Vth mismatch

In this part we will study the PMOS transistor voltage threshold (V_{th}) mismatch effect on the gain, NF, and IIP2.

The voltage threshold (V_{th}), was varied by 5% ($\frac{\Delta V_{th}}{V_{th}} = \pm 5\%$)

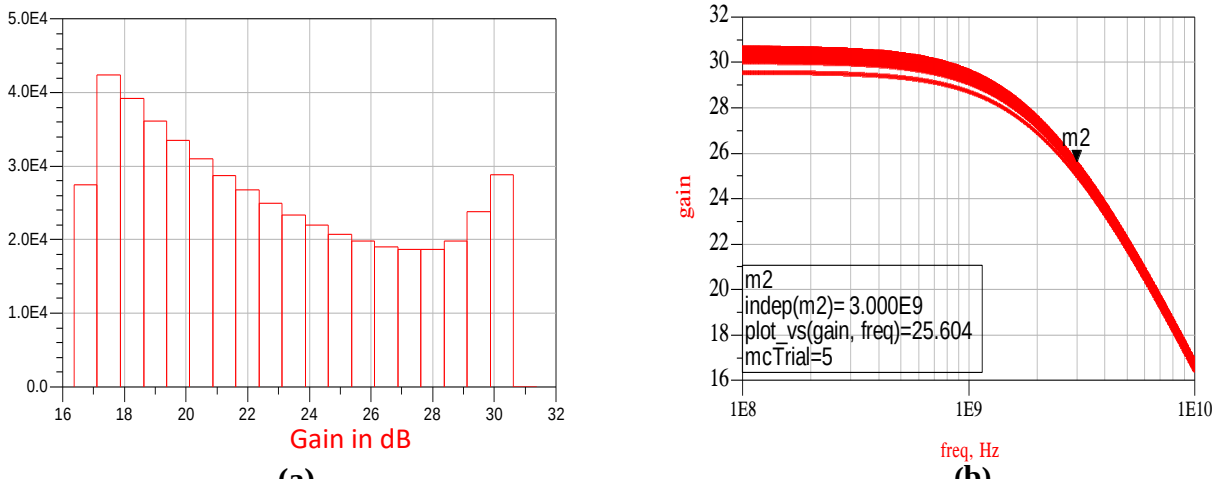

(a) **(b)**

Figure 4.14. *LNA Gain for PMOS V_{th} mismatch a) Monte Carlo simulation result, mean=30.15dB ,std dev=0.246dB, std uncertainty=0.0347dB and relative uncertainty=0.11% b) LNA Gain vs frequency*

LNA Gain Monte Carlo analysis in Figure 4.14(a) shows mean=30.15dB, std dev=0.246dB, std uncertainty=0.0347dB, and relative uncertainty=0.11%. In Figure 4.14(b) we plot LNA Gain versus frequency for different Monte Carlo trials. The results found are very close to Figure 4.11. There is no significant PMOS V_{th}mismatch effect on gain. Therefore, ninety five percent of the observations of gain are in the range [30.0806, 30.2194] dB.

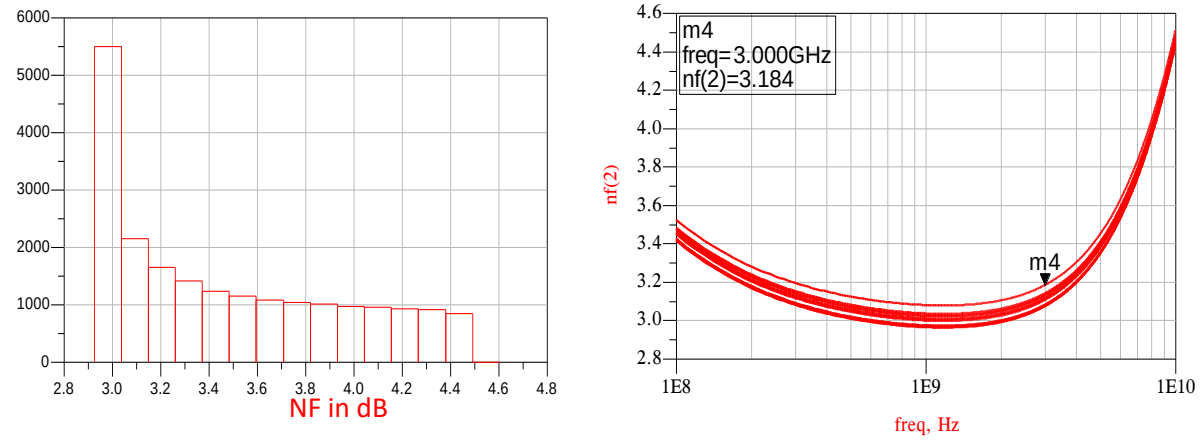

(a) **(b)**

Figure 4.15. *LNA NF for PMOS V_{th} mismatch a) Monte Carlo simulation result, mean=3.176dB, std dev=0.001dB, std uncertainty=0.00002dB and relative uncertainty=0.0007% b) LNA NF vs frequency.*

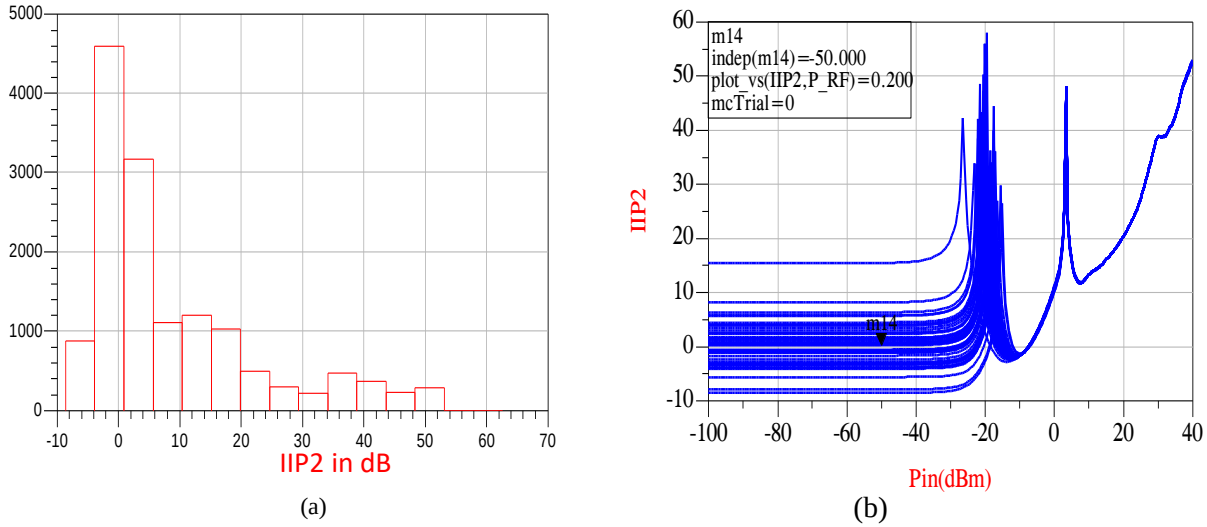

(a) (b)

Figure 4.16. *LNA IIP2 for PMOS V_{th} mismatch a) Monte Carlo simulation result, mean=8.665 dBm, std dev=14.008dBm, std uncertainty=1.98dBm and relative uncertainty=22.8% b) LNA IIP2 vs Pin.*

Figure 4.15 (a) depicts the corresponding NF in case of PMOS Vth mismatch. The mean equals to 3.176dB and the std dev equals to 0.001dB. Therefore, ninety five percent of the observations of NF are in the interval [3.17596, 3.17604]dB. From Figure 4.15(b) the NF vary from 3.1dB to 3.32dB in the 3-5GHz band.

Monte Carlo simulation result for LNA IIP2 in case of PMOS Vth mismatch is depicted in Figure 4.16(a) with a mean of 8.665dBm, the std dev=14.008dBm, the std uncertainty=1.98dBm and a relative uncertainty=22.8%. Figure 14.16 (b) shows LNA IIP2 versus input power. Therefore the confidence interval of IIP2 is [4.705, 12.625]dBm. Therefore, the PMOS V_{th} mismatch has a great influence on the second order intercept point of the LNA but will not have a significant impact on the gain and NF. From this analysis, we can confirm that the LNA IIP2 is sensitive to the variation in the threshold voltage and size of PMOS transistors, but LNA Gain and NF are less sensitive. This is why care must be taken with the mismatch of PMOS transistors.

3.2. Mismatch analysis in the receiver Front-End

3.2.1. Receiver front-end circuit

The passive mixer-based UWB receiver circuit is depicted in Figure 4.17. First, the LNA amplifies the UWB RF signal coming from the antenna. Then the differential RF signal V_{LNAout} is down-converted by the 25% duty-cycle double-balanced passive mixer and appears through the baseband load (C_{IF} || R_B). Due to their low power and improved linearity performance, 25% duty-cycle LO driven mixers have become quite popular recently [127][103]. To prevent the DC bias and the second-order intermodulation components produced inside the LNA, capacitors (C) are added to each mixer input.

Second-order intermodulation (IM2) products are mostly produced by the mixer during the overlap time when mixer switches operate concurrently [128] and [129]–[130], Asymmetric $\frac{W}{L}$ value or threshold voltage V_{th} in the NMOS switches of the mixer and unbalanced parasitic coupling between RF-to-LO or LO-to-RF ports cause IM2 products to be produced. Additionally, due to their frequency dependant properties, the degree of the aforementioned mismatch effects grows as the operating frequency rises. In the following, we study the effect of NMOS mixer switches mismatch on gain, NF, and IIP2 performance of the UWB receiver front end with a 25% duty cycle. The NMOS switches nominal size is $\frac{w}{L} = \frac{17.8\mu m}{0.18\mu m}$.

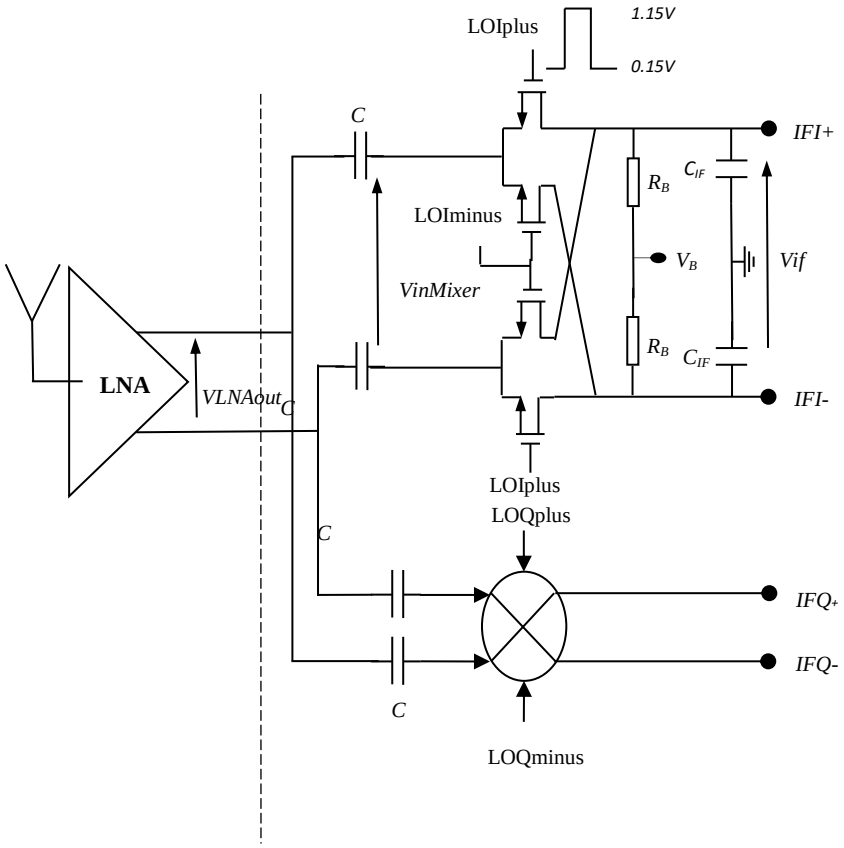

Differential double-balanced down-conversion passive mixer

Figure 4.17. *Passive mixer-based UWB receiver circuit.*

The differential outputs of one channel do not overlap during the 25% duty-cycle LO-driven mixer, in contrast to a 50% duty-cycle LO-driven mixer. Although each channel should ideally receive an equal amount of RF current, random asymmetry considerations may result in improperly balanced switching operations [131].

Utilizing an offset voltage source (V_{os}) linked in series at the mixer switch's gate allows for the modelling of the V_{th} mismatch.

3.2.2. NMOS transistor mismatch model for the mixer

The NMOS transistors of the passive mixer work as switches. This means that they operate in the linear region of the triode area, an appropriate NMOS current model in this region is given by:

$$I_D = \mu_n C_{ox} \frac{W}{L}(V_{GS} - V_{th})V_{DS} \qquad \text{for} \quad V_{DS} \ll (V_{GS} - V_{th}) \tag{4.17}$$

where I_D is the drain current,$(V_{GS} - V_{th})$ is the overdrive voltage, V_{th} is the threshold voltage, with C_{ox} being the gate-oxide capacitance per unit-area, μ_n as the carrier mobility, W and L being the width and length of the transistor respectively. $\frac{W}{L}$ is the aspect ratio. The drain current is a linear function of V_{DS}, this implies that the resistance between source and drain can be controlled by the overdrive voltage. We will study random mismatch between tow NMOS transistors in the mixer circuit. Suppose that the drain current are denoted $I_{D1}$and I_{D2}:

$$I_{D1} = \mu_n C_{ox}(\frac{W}{L})_1(V_{GS} - V_{th1})V_{DS1} \quad (4.18)$$

$$I_{D2} = \mu_n C_{ox}(\frac{W}{L})_2(V_{GS} - V_{th2})V_{DS2} \quad (4.19)$$

The current offset $\Delta I_D = I_{D1} - I_{D2}$ and the nominal current $I_D = \frac{I_{D1}+I_{D2}}{2}$

The size offset $\Delta(\frac{W}{L}) = (\frac{W}{L})_1 - (\frac{W}{L})_2$ and the nominal size $\frac{W}{L} = \frac{(\frac{W}{L})_1+(\frac{W}{L})_2}{2}$

The threshold voltage offset $\Delta V_{th} = V_{th1} - V_{th2}$ and the nominal threshold voltage $V_{th} = \frac{V_{th1}-V_{th2}}{2}$

Assuming $V_{DS1} \approx V_{DS2}$ and mismatches in $\mu_n C_{ox}$ is neglected, it follows:

$$\frac{\Delta I_D}{I_D} = \frac{V_{GS}}{V_{GS}-V_{th}} \frac{\Delta(\frac{W}{L})}{\frac{W}{L}} - \frac{\Delta V_{th}}{V_{GS}-V_{th}} \quad (4.20)$$

$\frac{\Delta I_D}{I_D}$ depends on the aspect ratio mismatch, the threshold voltage mismatch and the overdrive voltage mismatch.

This result suggests that, to minimize NMOS current mismatch, and thus reducing IM2 products, the overdrive voltage must be maximized. This is done when we have run simulation on the receiver front end using ADS tool.

3.3. Simulation result for the receiver front-end

3.3.1. Mixer NMOS switches size mismatch

A Monte Carlo simulations were run to evaluate the impact of process modifications on the performance parameters of the receiver front end. The size of mixer NMOS switches was varied by 5% from its nominal value ($\Delta(\frac{W}{L}) = \pm 5\%$)

Figure 4.18 shows Monte Carlo simulation result of IIP2 for the receiver front end. The mean=24.722dBm, the std dev=0.54dBm, the std uncertainty=0.024dBm and relative uncertainty=0.097%.

Therefore the confidence interval of receiver IIP2 is [24.674, 24.77]dBm.

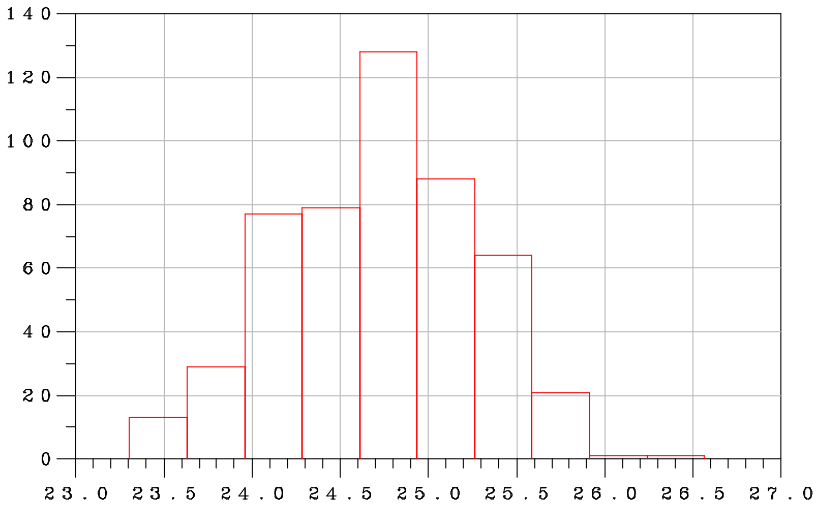

Figure 4.18. *IIP2Rx Monte Carlo simulation result for Mixer NMOS size mismatch, mean=24.722 dBm, std dev=0.54dBm, std uncertainty=0.024dBm and relative uncertainty=0.097%*

As we see in Figure 4.19(a) from Monte-Carlo simulation data, the mixer NMOS size mismatch of ±5% affects the receiver front end gain.

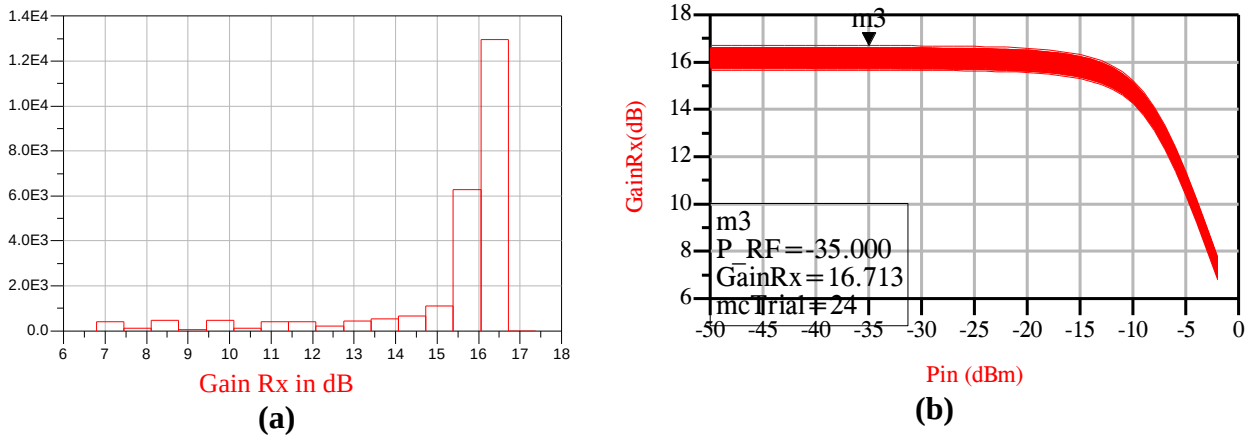

Figure 4.19. *GainRx for Mixer NMOS size mismatch a) Monte Carlo simulation result, mean = 15.285dB, std dev=2.081dB, std uncertainty=0.093dB and relative uncertainty=0.6% b) GainRx vs Pin.*

The results show that the mean of GainRx equals 15.285dB and the standard deviation (std dev) =2.081dB for a frequency of 4 GHz. Figure 4.19 (b) shows GainRx versus input power Pin for different Monte-Carlo trials. A 95% of receiver gain trials are in the range [15.099, 15.471] dB.

3.3.2. Mixer NMOS switches V_{th} mismatch

In this part, we will study the voltage threshold (V_{th}) mismatch effect on the receiver's front end performance. The voltage threshold (V_{th}), was varied by 5% ($\frac{\Delta V_{th}}{V_{th}} = \pm 5\%$).The Monte Carlo simulation result for the receiver IIP2 in the case of a NMOS Vth mismatch is depicted in Figure 4.20 with 500 iterations. We get a mean of 24.758dBm, the std dev=1.107dBm, and a relative uncertainty=0.2%. Therefore 95% of receiver IIP2 trials are in the range [24.659, 24.857] dBm.

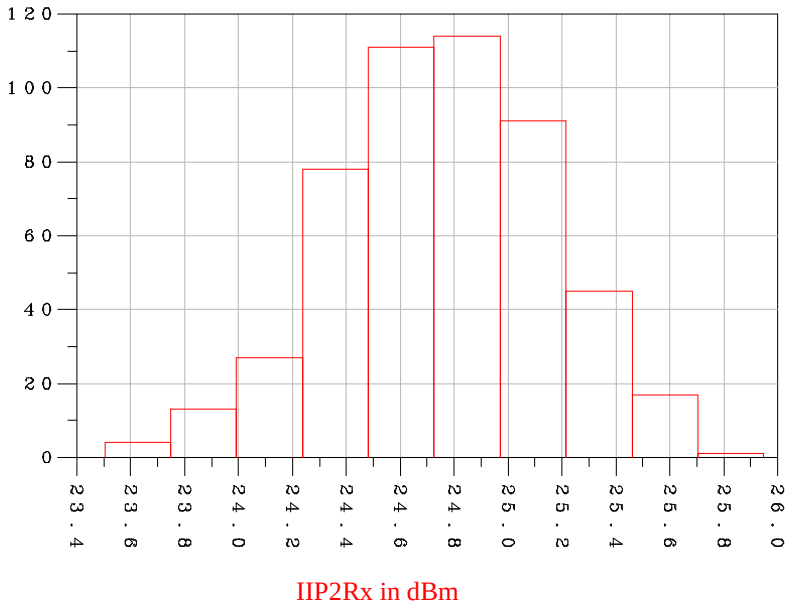

Figure 4.20. *IIP2Rx Monte Carlo simulation result for Mixer NMOS V_{th} mismatch, mean=24.758 dBm, std dev=1.107dBm, std uncertainty=0.0495dBm and relative uncertainty=0.2%.*

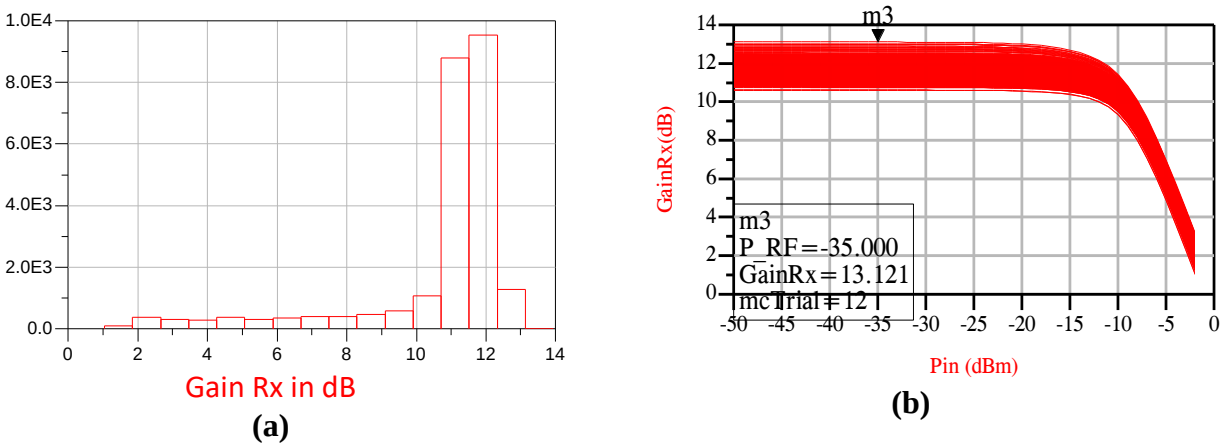

Figure 4.21. *GainRx for Mixer NMOS V_{th} mismatch a) Monte Carlo simulation result, mean= 10.709dB, std dev=2.246dB, std uncertainty=0.1dB and relative uncertainty=0.93% b) GainRx vs Pin.*

In Figure 4.21(a), we see Monte-Carlo simulation results for GainRx, in the case of mixer NMOS V_{th} mismatch of $\pm 5\%$. The results show that the mean of GainRx equals 10.709 dB and the standard deviation (std dev)=2.246 dB. Figure 4.21(b), shows GainRx versus input power Pin for different Monte-Carlo trials. A 95% of receiver Gain trials are in the confidence interval [10.509, 10.909] dB. Table 4.3 Summarizes Gain and IIP2 for LNA and Receiver front-end with the corresponding confidence interval at 95% of confidence.

Table4.3 Summary of Gain and IIP2 for LNA and Receiver front-end

	LNA		Receiver front-end	
	PMOS $\frac{W}{L}$ mismatch	PMOS V_{th} mismatch	NMOS switches $\frac{W}{L}$ mismatch	NMOS switches V_{th} mismatch
Mean Gain(dB)	30.15	30.15	15.285	10.709
Gain confidence interval(dB)	[30.055, 30.245]	[30.0806, 30.2194]	[15.099, 15.471]	[10.509, 10.909]
Mean IIP2(dBm)	13.143	8.665	24.722	24.758
IIP2 confidence interval(dBm)	[12.199, 14.087]	[4.705, 12.625]	[24.674, 24.77]	[24.659, 24.857]

4. Conclusion

A chirp spread spectrum UWB receiver operating in the 3-5 GHz band is designed Time domain as well as frequency domain analysis and simulation were done in order to determine the optimized value of each block parameter of the proposed receiver chain which obeys the specifications set by the WBAN standard.

The receiver is capable of handling a pulse repetition frequency of 10Mp/s with a pulse width of 20ns and a bandwidth of 500MHz. The receiver provides an output power level between -4.3 and -7dBm which is sufficient to drive the baseband demodulator. A sensitivity of -93.3dBm, a voltage gain of 85 dB an IIP3 of 11.2dBm, and a NF of 6.1 dB are achieved.

The analysis result suggests that, to minimize NMOS current mismatch, and thus reducing second-order inter modulation distortion, the overdrive voltage $V_{GS} - V_{th}$ must be maximized.. The receiver IIP2 confidence interval is [24.674, 24.77] dBm for NMOS switches $\frac{W}{L}$ mismatch and [24.659, 24.857] dBm for NMOS switch V_{th} mismatch.

General Conclusion

The research works presented in this thesis report which has been carried out within the laboratory SI2E: "Systems Integration & Emerging Energies Laboratory" in the National Engineering School of Sfax summarizes the contributions to the design of CSS-UWB receiver for WBAN medical applications.

The receiver is one of the parts of the medical sensor node that can be worn by patients. One of the most important challenges that researchers and designers face in these circuits is the size of the sensor node and the amount of energy consumed.

The results obtained during the development of this thesis are the modeling and design of different blocks of the receiver front end working with IR-UWB signal and Chirp-FSK modulation. Chirped signal with FSK modulation enables direct conversion technique with non-coherent FSK demodulator which simplifies the transceiver architecture.

A wideband inductorless balun LNA was designed with outstanding linearity performance, high gain and low noise figure. The design solely uses MOSFETs and employs a combination of the common gate and source stages to convert single-ended input to differential output. Optimization was conducted in order to ensure balanced output, noise and distortion canceling. Using 180 nm CMOS technology, the circuit exhibits strong wideband performance by amplifying signals at frequencies between 3GHz and 5GHz with gains that range from 25.5dB to 22dB respectively. The NF is between 3.2 dB and 3.5 dB. This LNA has demonstrated a suitable compromise between linearity, gain and noise figure while respecting UWB regulation. For that it is the best candidate for the receiver.

A differential passive mixer-based UWB receiver front-end was designed and analyzed using TSMC RF 0.18 μm CMOS process. The front-end circuit utilizes an inductorless balun LNA and a 25% duty cycle double-balanced passive mixer. Operating at 3–5 GHz, the receiver front-end exhibits a gain of 16 dB, an IIP3 of 3.14dBm and an IIP2 of 17.5 dBm leading to improved linearity. The designed receiver demonstrated an excellent RF and LO feed through rejection. The proposed mixer-based UWB receiver front end consumes 7.6 mW from a 1.8-V power supply, while the passive mixer consumes nearly zero power (0.72 pW).

Therefore the proposed double balanced passive mixer-based UWB receiver with differential topology is a good candidate to be integrated in a single chip UWB transceiver for WBAN medical application.

System level simulation of the complete receiver chain was conducted. Each circuit block of the receiver chain is designed with a strong focus on reducing circuit complexity while

maintaining the best performance. Time domain, as well as frequency domain analysis and simulation were done in order to determine the optimized value of each block parameter of the proposed receiver chain which obeys the specifications set by the WBAN standard. The analysis was conducted for minimum and maximum receiver input power. The receiver shows a sensitivity of -93.3dBm.

The impact of transistors mismatches on UWB receivers front end performances were also examined in this thesis. Two transistor mismatch models were proposed in order to evaluate the LNA output offset voltage and mixer offset current. A number of Monte Carlo simulations were performed in order to analyze the impact of a random variation in PMOS $\frac{W}{L}$ and voltage threshold on LNA gain, NF and IIP2. It is shown that the LNA IIP2 is sensitive to the variation in the threshold voltage and size of PMOS transistors but the LNA Gain and NF are less sensitive. A Monte Carlo and harmonic balance simulation were run to evaluate the impact of process modifications on the performance parameters of the receiver front-end. The size of mixer NMOS switches was varied by 5% from its nominal value. The analysis result suggests that, to minimize NMOS current mismatch and thus reducing second-order inter modulation distortion, the overdrive voltage (V_{GS}-V_{th}) must be maximized. Simulation results show that IIP2 of the receiver is not very sensitive to mixer NMOS mismatches.

The results showed that the proposed receiver is a promising contender for the low-power implementation of a wireless wearable device for medical applications.

The perspectives of my research work will focus on layout simulation and on the complete design of the sensor node using the 90nm CMOS technology to further reduce power consumption.

References

[1] P. Simon, “Pratiques de télémédecine et politique actuelle,” *ADSP*, no. 101, pp. 10–13, 2017.

[2] F. Puissance, U. La, B. Mics, P. Capteurs, D. Implant, and D. L. E. Corps, “Dé édica,” 2019.

[3] A. K. Teshome, B. Kibret, and D. T. H. Lai, “A review of implant communication technology in WBAN: Progress and challenges,” *IEEE Rev. Biomed. Eng.*, vol. 12, pp. 88–99, 2018.

[4] D. E. Bloom, D. Canning, and A. Lubet, “Global population aging: Facts, challenges, solutions & perspectives,” *Daedalus*, vol. 144, no. 2, pp. 80–92, 2015.

[5] T. A. Kareem and H. Trabelsi, “A Broadband High Gain, Noise-Canceling Balun LNA with 3–5 GHz UWB Receivers for Medical Applications.,” *Int. J. Online Biomed. Eng.*, vol. 18, no. 3, 2022.

[6] S. Sindhu, S. Vashiath, and S. K. Chakarvarti, “A Review on Wireless Body Area Network (WBAN) for Health Monitoring System, Implementation Protocol,” *Commun. Appl. Electron. Found. Comput. Sci. Newyork, USA*, vol. 4, no. 7, 2016.

[7] S. Singla and K. Sharma, “A review paper on wireless body area network for health care applications,” *Int. J. Comput. Sci. Mob. Comput.*, vol. 5, no. 10, pp. 1–11, 2016.

[8] J. I. Bangash, A. H. Abdullah, M. H. Anisi, and A. W. Khan, “A survey of routing protocols in wireless body sensor networks,” *Sensors*, vol. 14, no. 1, pp. 1322–1357, 2014.

[9] P. Kaur and S. S. Kang, “Hybrid Routing Protocol for Wireless Body Area Networks.”

[10] M. Yaghoubi, K. Ahmed, and Y. Miao, “Wireless Body Area Network (WBAN): A Survey on Architecture, Technologies, Energy Consumption, and Security Challenges,” *J. Sens. Actuator Networks*, vol. 11, no. 4, p. 67, 2022.

[11] A. Nadeem, M. A. Hussain, O. Owais, A. Salam, S. Iqbal, and K. Ahsan, “Application specific study, analysis and classification of body area wireless sensor network applications,” *Comput. Networks*, vol. 83, pp. 363–380, 2015.

[12] M. Tsang, “Connecting and caring: innovations for healthy ageing,” *World Heal. Organ. Bull. World Heal. Organ.*, vol. 90, no. 3, p. 162, 2012.

[13] S. Movassaghi, M. Abolhasan, J. Lipman, D. Smith, and A. Jamalipour, “Wireless body area networks: A survey,” *IEEE Commun. Surv. tutorials*, vol. 16, no. 3, pp. 1658–1686, 2014.

[14] S. Ullah *et al.*, “A comprehensive survey of wireless body area networks: On PHY, MAC, and network layers solutions,” *J. Med. Syst.*, vol. 36, pp. 1065–1094, 2012.

[15] R. Kachroo and D. R. R. Bajaj, “A novel technique for optimized routing in wireless body area network using genetic algorithm,” *J. Netw. Commun. Emerg. Technol.*, vol. 2, no. 2, 2015.

[16] H. F. Hafez Fouad, “Design and implementation of wireless sensors network and cloud based telemedicine system for rural clinics and health centers,” *Int. J. Sci. Eng. Res.*, vol. 6, no. 2, 2015.

[17] J. Y. Khan and M. R. Yuce, *Wireless body area network (WBAN) for medical applications*. InTechOpen, 2010.

[18] S. Patel *et al.*, “Monitoring motor fluctuations in patients with Parkinson’s disease using wearable sensors,” *IEEE Trans. Inf. Technol. Biomed.*, vol. 13, no. 6, pp. 864–873, 2009.

[19] B. Malik and V. R. Singh, “A survey of research in WBAN for biomedical and scientific applications,” *Health Technol. (Berl).*, vol. 3, pp. 227–235, 2013.

[20] D. M. Barakah and M. Ammad-uddin, “A survey of challenges and applications of wireless body area network (WBAN) and role of a virtual doctor server in existing architecture,” in *2012 Third International Conference on Intelligent Systems Modelling and Simulation*, 2012, pp. 214–219.

[21] A. V Mbakop, A. Lambebo, L. Jayatilleke, and S. Haghani, “Implementation of a wireless body area network for healthcare monitoring,” *ASEE-American Soc. Eng. Educ.*, 2013.

[22] S. Movassaghi, A. Majidi, A. Jamalipour, D. Smith, and M. Abolhasan, “Enabling interference-aware and energy-efficient coexistence of multiple wireless body area

networks with unknown dynamics," *IEEE Access*, vol. 4, pp. 2935–2951, 2016.

[23] K. Hasan, K. Biswas, K. Ahmed, N. S. Nafi, and M. S. Islam, "A comprehensive review of wireless body area network," *J. Netw. Comput. Appl.*, vol. 143, pp. 178–198, 2019.

[24] S. Ullah, P. Khan, N. Ullah, S. Saleem, H. Higgins, and K. S. Kwak, "A review of wireless body area networks for medical applications," *arXiv Prepr. arXiv1001.0831*, 2010.

[25] S. Ullah *et al.*, "A comprehensive survey of wireless body area networks," *J. Med. Syst.*, vol. 36, no. 3, pp. 1065–1094, 2012.

[26] D. Lewis, "802.15. 6 call for applications in body area networksresponse summary,"," *15–08–0407–05-0006*, 2008.

[27] P. Van Daele, I. Moerman, and P. Demeester, "Wireless body area networks: status and opportunities," in *2014 XXXIth URSI General Assembly and Scientific Symposium (URSI GASS)*, 2014, pp. 1–4.

[28] H.-T. Chu, C.-C. Huang, Z.-H. Lian, and J. J. P. Tsai, "A ubiquitous warning system for asthma-inducement," in *IEEE International Conference on Sensor Networks, Ubiquitous, and Trustworthy Computing (SUTC'06)*, 2006, vol. 2, pp. 186–191.

[29] L. Liu *et al.*, "Global, regional, and national causes of child mortality in 2000–13, with projections to inform post-2015 priorities: an updated systematic analysis," *Lancet*, vol. 385, no. 9966, pp. 430–440, 2015.

[30] D. P. Tobón, T. H. Falk, and M. Maier, "Context awareness in WBANs: a survey on medical and non-medical applications," *IEEE Wirel. Commun.*, vol. 20, no. 4, pp. 30–37, 2013.

[31] I. C. S. L. S. Committee, "IEEE Standard for Information technology-Telecommunications and information exchange between systems-Local and metropolitan area networks-Specific requirements Part 11: Wireless LAN Medium Access Control (MAC) and Physical Layer (PHY) Specifications," *IEEE Std 802.11^*, 2007.

[32] T. Cooklev, *Wireless communication standards: A study of IEEE 802.11, 802.15,*

802.16. IEEE Standards Association, 2004.

[33] M. M. Alam and E. Ben Hamida, "Surveying wearable human assistive technology for life and safety critical applications: Standards, challenges and opportunities," *Sensors*, vol. 14, no. 5, pp. 9153–9209, 2014.

[34] M. Li and M. Zhuang, "An overview of Physical layers on wireless body area network," *Anti-counterfeiting, Secur. Identif.*, pp. 1–5, 2012.

[35] I. of E. and E. Engineers, *IEEE Wireless Communications Letters*. IEEE, 2012.

[36] R. Huang, Z. Nie, C. Duan, Y. Liu, L. Jia, and L. Wang, "Analysis and comparison of the IEEE 802.15. 4 and 802.15. 6 wireless standards based on MAC layer," in *Health Information Science: 4th International Conference, HIS 2015, Melbourne, Australia, May 28-30, 2015, Proceedings 4*, 2015, pp. 7–16.

[37] A. Nabila, "A QoS based comparative analysis of the IEEE standards 802.15. 4 & 802.15. 6 in WBAN-based healthcare monitoring systems," in *2019 International conference on wireless technologies, embedded and intelligent systems (WITS)*, 2019, pp. 1–5.

[38] A. Trigui, S. Hached, F. Mounaim, A. C. Ammari, and M. Sawan, "Inductive power transfer system with self-calibrated primary resonant frequency," *IEEE Trans. power Electron.*, vol. 30, no. 11, pp. 6078–6087, 2015.

[39] M. Hernandez and R. Miura, *Body Area Networks using IEEE 802.15. 6: Implementing the ultra wide band physical layer*. Academic Press, 2014.

[40] V. Mainanwal, M. Gupta, and S. K. Upadhayay, "A survey on wireless body area network: Security technology and its design methodology issue," in *2015 international conference on innovations in information, embedded and communication systems (ICIIECS)*, 2015, pp. 1–5.

[41] C. A. Tavera, J. H. Ortiz, O. I. Khalaf, D. F. Saavedra, and T. H. H. Aldhyani, "Wearable wireless body area networks for medical applications," *Comput. Math. Methods Med.*, vol. 2021, 2021.

[42] M. Gupta, S. Tanwar, A. Rana, and H. Walia, "Smart healthcare monitoring system using wireless body area network," in *2021 9th International Conference on*

Reliability, Infocom Technologies and Optimization (Trends and Future Directions)(ICRITO), 2021, pp. 1–5.

[43] Y. N. M. Saleh, C. C. Chibelushi, A. A. Abdel-Hamid, and A.-H. Soliman, "Privacy preservation for wireless sensor networks in healthcare: State of the art, and open research challenges," *arXiv Prepr. arXiv2012.12958*, 2020.

[44] H. Rahangdale, "A Review on WMSN (Wireless Medical Sensor Networks) for Health Monitoring Systems," *ECS Trans.*, vol. 107, no. 1, p. 1973, 2022.

[45] A. Adarsh and B. Kumar, "Wireless medical sensor networks for smart e-healthcare," in *Intelligent Data Security Solutions for e-Health Applications*, Elsevier, 2020, pp. 275–292.

[46] Y. Qu, G. Zheng, H. Ma, X. Wang, B. Ji, and H. Wu, "A survey of routing protocols in WBAN for healthcare applications," *Sensors*, vol. 19, no. 7, p. 1638, 2019.

[47] A. Rady, E. M. El-Rabaie, M. Shokair, and N. Abdel-Salam, "Comprehensive survey of routing protocols for Mobile Wireless Sensor Networks," *Int. J. Commun. Syst.*, vol. 34, no. 15, p. e4942, 2021.

[48] Z. Huanan, X. Suping, and W. Jiannan, "Security and application of wireless sensor network," *Procedia Comput. Sci.*, vol. 183, pp. 486–492, 2021.

[49] A. O. Salau, N. Marriwala, and M. Athaee, "Data security in wireless sensor networks: Attacks and countermeasures," in *Mobile Radio Communications and 5G Networks: Proceedings of MRCN 2020*, 2021, pp. 173–186.

[50] M. R. K. Naik and P. Samundiswary, "Wireless body area network security issues—Survey," in *2016 International Conference on Control, Instrumentation, Communication and Computational Technologies (ICCICCT)*, 2016, pp. 190–194.

[51] L. Zhong *et al.*, "Technological Requirements and Challenges in Wireless Body Area Networks for Health Monitoring: A Comprehensive Survey," *Sensors*, vol. 22, no. 9, p. 3539, 2022.

[52] H. Wu, Y. Peng, K. Long, S. Cheng, and J. Ma, "Performance of reliable transport protocol over IEEE 802.11 wireless LAN: analysis and enhancement," in *Proceedings. Twenty-first annual joint conference of the IEEE computer and communications*

societies, 2002, vol. 2, pp. 599–607.

[53] E. C. C. CEPT, "ECC decision of 24 March 2006 on the harmonised conditions for devices using ultra-wideband (UWB) technology in bands below 10.6 GHz," *ECC/DEC/(06)*, vol. 4, 2006.

[54] S. Geng, D. Liu, Y. Li, H. Zhuo, W. Rhee, and Z. Wang, "A 13.3 mW 500 Mb/s IR-UWB transceiver with link margin enhancement technique for meter-range communications," *IEEE J. Solid-State Circuits*, vol. 50, no. 3, pp. 669–678, 2015.

[55] K. K. Lee and T. S. Lande, "A wireless-powered IR-UWB transmitter for long-range passive RFID tags in 90-nm CMOS," *IEEE Trans. Circuits Syst. II Express Briefs*, vol. 61, no. 11, pp. 870–874, 2014.

[56] U. F. C. Commission, "FCC Revision of part 15 of the commission's rules regarding ultra-wideband transmission systems: First report and order," *Tech. Rep.*, 2002.

[57] F. C. Commission, "Revision of part 15 of the commission's rules regarding ultra-wideband transmission systems," *First Rep. order*, 2002.

[58] F. Nekoogar, *Ultra-Wideband Communications: Fundamentals and Applications Fundamentals and Applications*. Prentice Hall Press, 2011.

[59] M. Crepaldi, G. N. Angotzi, and L. Berdondini, "A 0.34 mm 2 1 Gb/s non-coherent UWB receiver architecture with pulse enhancement and double PLL clock/data packet recovery," *IEEE Trans. Circuits Syst. I Regul. Pap.*, vol. 66, no. 7, pp. 2735–2748, 2019.

[60] X. Wang, "A 0.18 μm CMOS UWB wireless transceiver for medical sensing applications." Citeseer, 2008.

[61] A. Bhuiyan, "Analysis and design of low power CMOS ultra wideband receiver." University of Nevada, Las Vegas, 2009.

[62] J. Jin, S. Lecchi, R. Castello, and D. Manstretta, "An FDD Auxiliary Receiver with a Highly Linear Low Noise Amplifier," in *ESSCIRC 2022-IEEE 48th European Solid State Circuits Conference (ESSCIRC)*, 2022, pp. 309–312.

[63] P. J. Chang, A. Rofougaran, and A. A. Abidi, "A CMOS channel-select filter for a

direct-conversion wireless receiver," *IEEE J. Solid-State Circuits*, vol. 32, no. 5, pp. 722–729, 1997.

[64] J. Y.-C. Chang, *An integrated 900 MHz spread-spectrum wireless receiver in 1-(mu) m CMOS and a suspended inductor technique*. University of California, Los Angeles, 1988.

[65] B. Razavi, "Design considerations for direct-conversion receivers," *IEEE Trans. Circuits Syst. II Analog Digit. Signal Process.*, vol. 44, no. 6, pp. 428–435, 1997.

[66] C. R. Iversen, *A UTRA/FDD Receiver Architecture and LNA in CMOS Technology*. Aalborg Universitetsforlag, 2001.

[67] D. Manstretta, R. Castello, and F. Svelto, "Low 1/f noise CMOS active mixers for direct conversion," *IEEE Trans. circuits Syst. II Analog Digit. signal Process.*, vol. 48, no. 9, pp. 846–850, 2001.

[68] B. Razavi and R. Behzad, *RF microelectronics*, vol. 2. Prentice hall New York, 2012.

[69] Jihai Duan, Q. Hao2, Y. Zheng, B. Wei, W. Xu, and S. Xu, "Design of an Incoherent IR-UWB Receiver Front-End in 180-nm CMOS Technology." IEEE, p. 5, 2015.

[70] P. Sepidband and K. Entesari, "A CMOS wideband receiver resilient to out-of-band blockers using blocker detection and rejection," *IEEE Trans. Microw. Theory Tech.*, vol. 66, no. 5, pp. 2340–2355, 2018.

[71] S. B. Sedaghat, F. Safari, G. R. Karimi, S. M. Alizadeh, and R. Banitalebi, "0.3 V, 0.5 mW Low Noise Amplifier for 5.1 GHz Applications," 2012.

[72] T. H. Lee, *The design of CMOS radio-frequency integrated circuits*. Cambridge university press, 2003.

[73] T. H. Lee, "The design of CMOS radio-frequency integrated circuits," *Commun. Eng.*, vol. 2, no. 4, p. 47, 2004.

[74] P. Sharma, "Design of a 3.1-4.8 GHZ RF front-end for an ultra wideband receiver." Texas A&M University, 2006.

[75] S. Benali and H. Trabelsi, "Analysis of device mismatches effect on the performance of UWB-Ring VCO," in *2020 17th International Multi-Conference on Systems, Signals &*

Devices (SSD), 2020, pp. 814–818.

[76] D. Ben IsIssa, D. Ben, Kachouri, A., & Samet, M. (2011). New design of 3.2–4.8 GHz generator for multi-bands architecture of UWB communication. Analog Integrated Circuits and Signal Processing, 68(1), 9–20.sa, A. Kachouri, and M. Samet, "New design of 3.2–4.8 GHz generator for multi-bands architecture of UWB communication," *Analog Integr. Circuits Signal Process.*, vol. 68, no. 1, pp. 9–20, 2011.

[77] J. H. C. Zhan and S. S. Taylor, "A 5GHz resistive-feedback CMOS LNA for low-cost multi-standard applications," *Digest of Technical Papers - IEEE International Solid-State Circuits Conference*. 2006, doi: 10.1109/isscc.2006.1696111.

[78] H. S. Madiha Hajri, Dalenda Ben Issa, "Low noise amplifier for MB-OFDM UWB receivers." IEEE, p. 4, 2016.

[79] J. G. I. Bastos, L. B. Oliveira, J. P. Oliveira and M. M. Silva, "Balun LNA with Continuosly Controlable Gain and with Noise and Distortion Cancellation." IEEE, p. 4, 2012.

[80] D. Krstić, "RF microelectronics: Behzad Razavi: Prentice-Hall PTR, Upper Saddle River, NJ, 1998, hardcover, 335 pp., $92.99. ISBN 0-13-887571-5." Elsevier, 1998.

[81] F. Bruccoleri, E. A. M. Klumperink, and B. Nauta, "Wide-band CMOS low-noise amplifier exploiting thermal noise canceling," *IEEE J. Solid-State Circuits*, vol. 39, no. 2, pp. 275–282, 2004.

[82] I. Bastos, L. B. Oliveira, J. Goes, and M. Silva, "Analysis and Design of a MOSFET-only Wideband Balun LNA," *Int. J. Microelectron. Comput. Sci.*, vol. 1, no. 3, pp. 241–248, 2010.

[83] L. B. Oliveira, J. R. Fernandes, I. M. Filanovsky, C. J. M. Verhoeven, and M. M. Silva, *Analysis and design of quadrature oscillators*. Springer Science & Business Media, 2008.

[84] T. Tille, J. Sauerbrey, M. Mauthe, and D. Schmitt-Landsiedel, "Design of low-voltage MOSFET-only/spl Sigma//spl Delta/modulators in standard digital CMOS technology," *IEEE Trans. Circuits Syst. I Regul. Pap.*, vol. 51, no. 1, pp. 96–109, 2004.

[85] MOUNA Bettaieb, S. Benali, G. Bouzid, and HATEM Trabelsi, “Analysis and optimization of RF Front-End for MICS Band Receiver.” IEEE International Conference on Design & Test of Integrated Micro & Nano-Systems Analysis, p. 5, 2019.

[86] T. A. Vu, H. A. Hjortland, Ø. Næss, and T. S. Lande, “A 3–5 GHz IR-UWB receiver front-end for wireless sensor networks,” in *2013 IEEE International Symposium on Circuits and Systems (ISCAS)*, 2013, pp. 2380–2383.

[87] S. C. Blaakmeer, E. A. M. Klumperink, D. M. W. Leenaerts, and B. Nauta, “Wideband balun-LNA with simultaneous output balancing, noise-canceling and distortion-canceling,” *IEEE J. Solid-State Circuits*, vol. 43, no. 6, pp. 1341–1350, 2008.

[88] R. Bagheri *et al.*, “An 800-MHz–6-GHz software-defined wireless receiver in 90-nm CMOS,” *IEEE J. Solid-State Circuits*, vol. 41, no. 12, pp. 2860–2876, 2006.

[89] L. Xia, K. Shao, H. Chen, Y. Huang, Z. Hong, and P. Y. Chiang, “0.15-nJ/b 3–5-GHz IR-UWB system with spectrum tunable transmitter and merged-correlator noncoherent receiver,” *IEEE Trans. Microw. Theory Tech.*, vol. 59, no. 4, pp. 1147–1156, 2011.

[90] L. Liu, T. Sakurai, and M. Takamiya, “A charge-domain auto-and cross-correlation based data synchronization scheme with power-and area-efficient PLL for impulse radio UWB receiver,” *IEEE J. Solid-State Circuits*, vol. 46, no. 6, pp. 1349–1359, 2011.

[91] B. Shi and M. Y. W. Chia, “Design of a CMOS UWB receiver front-end with noise-cancellation and current-reuse,” in *2010 IEEE International Conference on Ultra-Wideband*, 2010, vol. 1, pp. 1–4.

[92] H. Trabelsi, I. Barraj, and M. Masmoudi, “A 3–5 GHz FSK-UWB transmitter for wireless personal healthcare applications,” *AEU-International J. Electron. Commun.*, vol. 69, no. 1, pp. 262–273, 2015.

[93] B. Saif and T. Hatem, “Low-complexity passive mixer-based UWB pulse generator with leakage compensation and spectrum Tunability,” in *2020 IEEE International Conference on Design & Test of Integrated Micro & Nano-Systems (DTS)*, 2020, pp. 1–5.

[94] R. S. Rao, *Microwave engineering*. PHI Learning Pvt. Ltd., 2015.

[95] B. Razavi *et al.*, "A 0.13/spl mu/m CMOS UWB transceiver," in *ISSCC. 2005 IEEE International Digest of Technical Papers. Solid-State Circuits Conference, 2005.*, 2005, pp. 216–594.

[96] C. Sandner *et al.*, "A wimedia/mboa-compliant cmos rf transceiver for uwb," *IEEE J. Solid-State Circuits*, vol. 41, no. 12, pp. 2787–2794, 2006.

[97] Y. Zheng *et al.*, "A CMOS carrier-less UWB transceiver for WPAN applications," in *2006 IEEE International Solid State Circuits Conference-Digest of Technical Papers*, 2006, pp. 378–387.

[98] H. Khosravi, Abolfazl Bijari, Nabeeh Kandalaft, and J. Cabral, "A Low Power Concurrent Dual-Band Low Noise Amplifier For WLAN Applications." IEEE, p. 6, 2019.

[99] N. Seyedhosseinzadeh and A. Nabavi, "Design of an active CMOS subharmonic mixer with enhanced transconductance," *AEU-International J. Electron. Commun.*, vol. 73, pp. 98–104, 2017.

[100] T. A. Kareem and H. Trabelsi, "Passive Mixer-based UWB Receiver with Low Loss, High Linearity and Noise-cancelling for Medical Applications," *Int. J. Electron. Telecommun.*, pp. 61–67, 2023.

[101] S. Zhou and M.-C. Chang, "A CMOS passive mixer with low flicker noise for low-power direct-conversion receiver," *IEEE J. Solid-State Circuits*, vol. 40, no. 5, pp. 1084–1093, 2005.

[102] E. S. Atalla, F. Zhang, P. T. Balsara, A. Bellaouar, S. Ba, and K. Kiasaleh, "Time-domain analysis of passive mixer impedance: A switched-capacitor approach," *IEEE Trans. Circuits Syst. I Regul. Pap.*, vol. 64, no. 2, pp. 347–359, 2016.

[103] A. Mirzaei, H. Darabi, J. C. Leete, and Y. Chang, "Analysis and optimization of direct-conversion receivers with 25% duty-cycle current-driven passive mixers," *IEEE Trans. Circuits Syst. I Regul. Pap.*, vol. 57, no. 9, pp. 2353–2366, 2010.

[104] X. He and J. van Sinderen, "A low-power, low-EVM, SAW-less WCDMA transmitter using direct quadrature voltage modulation," *IEEE J. Solid-State Circuits*, vol. 44, no.

12, pp. 3448–3458, 2009.

[105] B. Gilbert, “A precise four-quadrant multiplier with subnanosecond response,” *IEEE J. Solid-State Circuits*, vol. 3, no. 4, pp. 365–373, 1968.

[106] J. Crols and M. S. J. Steyaert, “A 1.5 GHz highly linear CMOS downconversion mixer,” *IEEE J. Solid-State Circuits*, vol. 30, no. 7, pp. 736–742, 1995.

[107] S. Chehrazi, R. Bagheri, and A. A. Abidi, “Noise in passive FET mixers: A simple physical model,” in *Proceedings of the IEEE 2004 Custom Integrated Circuits Conference (IEEE Cat. No. 04CH37571)*, 2004, pp. 375–378.

[108] A. Meaamar, “An ultra-wideband receiver front-end,” *Diss. Nanyang Technol. Univ.*, 2010.

[109] M. T. Terrovitis and R. G. Meyer, “Intermodulation distortion in current-commutating CMOS mixers,” *IEEE J. Solid-State Circuits*, vol. 35, no. 10, pp. 1461–1473, 2000.

[110] M. Y. Algumaei, N. A. Shairi, Z. Zakaria, and I. M. Ibrahim, “Review of mixer and balun designs for UWB applications,” *Int. J. Appl. Eng. Res.*, vol. 12, no. 17, pp. 6514–6522, 2017.

[111] C. Andrews and A. C. Molnar, “A passive mixer-first receiver with digitally controlled and widely tunable RF interface,” *IEEE J. Solid-State Circuits*, vol. 45, no. 12, pp. 2696–2708, 2010.

[112] Y. Gao, Y. Zheng, and C.-H. Heng, “Low-power CMOS RF front-end for non-coherent IR-UWB receiver,” in *ESSCIRC 2008-34th European Solid-State Circuits Conference*, 2008, pp. 386–389.

[113] Z. Zou *et al.*, “A low-power and flexible energy detection IR-UWB receiver for RFID and wireless sensor networks,” *IEEE Trans. Circuits Syst. I Regul. Pap.*, vol. 58, no. 7, pp. 1470–1482, 2011.

[114] T. A. Vu, H. A. Hjortland, O. Nass, and T. S. Lande, “A 3-5 GHz IR-UWB receiver front-end for wireless sensor networks,” *Proceedings - IEEE International Symposium on Circuits and Systems*. pp. 2380–2383, 2013, doi: 10.1109/ISCAS.2013.6572357.

[115] T. A. Kareem and H. Trabelsi, “A Novel CSS-UWB Receiver Front-End,” in *2022*

IEEE International Conference on Design & Test of Integrated Micro & Nano-Systems (DTS), 2022, pp. 1–5.

[116] H. Trabelsi, G. Bouzid, F. Derbel, and M. Masmoudi, "An 863–870 MHz spread-spectrum FSK transceiver design for wireless sensor," *Microelectronics J.*, vol. 41, no. 8, pp. 465–473, 2010.

[117] L. Simanjuntak, "A novel chirp slope keying modulation scheme for underwater communication," 2004.

[118] S. Joo *et al.*, "A fully integrated 802.15. 4a IR-UWB Transceiver in 0.13 μm CMOS with digital RRC synthesis," in *2010 IEEE International Solid-State Circuits Conference-(ISSCC)*, 2010, pp. 228–229.

[119] Y. Zheng *et al.*, "A 0.18 μm CMOS 802.15. 4a UWB transceiver for communication and localization," in *2008 IEEE International Solid-State Circuits Conference-Digest of Technical Papers*, 2008, pp. 118–600.

[120] H. Trabelsi, I. Barraj, and M. Masmoudi, "A Chirp Spread Spectrum FSK IR-UWB Receiver," *Trends Appl. Sci. Res.*, vol. 9, no. 8, p. 461, 2014.

[121] S. Al-Janabi, I. Al-Shourbaji, M. Shojafar, and S. Shamshirband, "Survey of main challenges (security and privacy) in wireless body area networks for healthcare applications," *Egypt. Informatics J.*, vol. 18, no. 2, pp. 113–122, 2017.

[122] B. Razavi, *Design of analog CMOS integrated circuits*. 清华大学出版社有限公司, 2005.

[123] T. Serrano-Gotarredona and B. Linares-Barranco, "A new five-parameter MOS transistor mismatch model," *IEEE Electron Device Lett.*, vol. 21, no. 1, pp. 37–39, 2000.

[124] P. G. Drennan and C. C. McAndrew, "Understanding MOSFET mismatch for analog design," *IEEE J. Solid-State Circuits*, vol. 38, no. 3, pp. 450–456, 2003.

[125] J. Wang and A. K. K. Wong, "Effects of mismatch on CMOS double-balanced mixers: a theoretical analysis," in *Proceedings 2001 IEEE Hong Kong Electron Devices Meeting (Cat. No. 01TH8553)*, 2001, pp. 85–88.

[126] D. Bhatt, J. Mukherjee, and J.-M. Redouté, “A Self-Biased Mixer in $0.18\mu\text {m} $ CMOS for an Ultra-Wideband Receiver,” *IEEE Trans. Microw. Theory Tech.*, vol. 65, no. 4, pp. 1294–1302, 2017.

[127] D. Kaczman *et al.*, “A Single–Chip 10-Band WCDMA/HSDPA 4-Band GSM/EDGE SAW-less CMOS Receiver With DigRF 3G Interface and ${+} $90 dBm IIP2,” *IEEE J. Solid-State Circuits*, vol. 44, no. 3, pp. 718–739, 2009.

[128] J. Han and K. Kwon, “A SAW-less receiver front-end employing body-effect control IIP2 calibration,” *IEEE Trans. Circuits Syst. I Regul. Pap.*, vol. 61, no. 9, pp. 2691–2698, 2014.

[129] D. Manstretta, M. Brandolini, and F. Svelto, “Second-order intermodulation mechanisms in CMOS downconverters,” *IEEE J. Solid-State Circuits*, vol. 38, no. 3, pp. 394–406, 2003.

[130] S. Chehrazi, A. Mirzaei, and A. A. Abidi, “Second-order intermodulation in current-commutating passive FET mixers,” *IEEE Trans. Circuits Syst. I Regul. Pap.*, vol. 56, no. 12, pp. 2556–2568, 2009.

[131] J. Han and K. Kwon, “RF receiver front-end employing IIP2-enhanced 25% duty-cycle quadrature passive mixer for advanced cellular applications,” *IEEE Access*, vol. 8, pp. 8166–8177, 2020.

Republic of Tunisia
Ministry of Higher Education,
Scientific Research

University of Sfax
National Engineering School of Sfax
(ENIS)

Doctoral School

Sciences and Technologies

Electrical Engineering

Order n°: 25 –2023

Contribution to the design of CSS-UWB receiver for medical applications in the WBAN network

Thaar Abdalraheem Kareem Al-musaadi

Abstract: The Ultra-Wideband Wireless Body Area Network (UWB-WBAN) has been identified to provide efficient, low-power and improved wireless communication between sensor nodes worn by the human body to monitor physiological signals. In this thesis, a 3-5 GHz CSS-UWB receiver front-end for medical wearable sensor node is designed and analyzed using TSMC 0.18µm CMOS technology. In a first part, a wideband inductorless balun LNA was designed with outstanding linearity performance, high gain and low noise figure. Optimization was conducted in order to ensure balanced output, noise and distortion canceling. Then a low power double balanced passive mixer-based UWB receiver was studied and designed. A duty cycle of 25% was chosen to eliminate overlap between LO signals, thereby improving receiver linearity. The proposed receiver was simulated at the system level. Time domain analysis as well as frequency domain analysis were done in order to determine the optimized block parameters of the receiver chain. The CSS-UWB receiver works with a sensitivity of -93.3dBm. It is capable of handling a pulse repetition frequency of 10Mp/s with a pulse width of 20ns and a bandwidth of 500 MHz. Finally, analysis of MOSFET transistors mismatches effect on the performance of UWB receiver front-end was carried out. A PMOS and NMOS transistors mismatch models were proposed. A Monte Carlo and harmonic balance simulations were performed in order to evaluate the impact of transistors size mismatch as well as Vth mismatch on the receiver gain and IIP2. We proved that the proposed circuit meets the requirement of UWB system perfectly which make it suitable for WBAN applications.

Key-words: CSS-UWB Receiver, WBAN Wireless Sensors, LNA, Mixer, MOS mismatch.